
Identification of Nilsson Orbitals in the Superdeformed Minimum of ^{237}Pu

Thomas James Morgan



München 2008

Identification of Nilsson Orbitals in the Superdeformed Minimum of ^{237}Pu

Thomas James Morgan

Dissertation
an der Fakultät für Physik
der Ludwig-Maximilians-Universität
München

vorgelegt von
Thomas James Morgan
aus München

München, den 31.03.2008

Erstgutachter: Prof. Dr. Dietrich Habs

Zweitgutachter: Prof. Dr. Otmar Biebel

Tag der mündlichen Prüfung: 27.05.2008

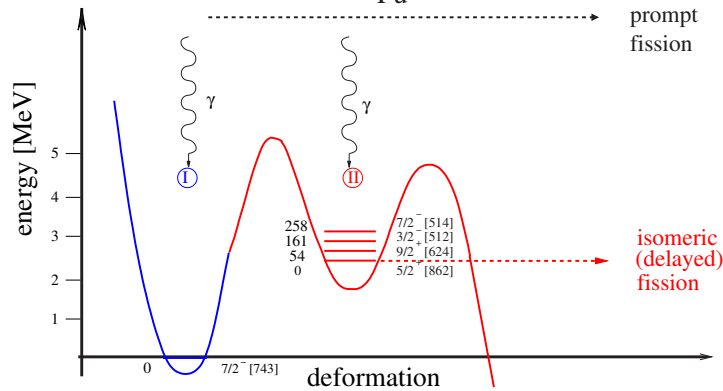
Zusammenfassung

Identifizierung von Nilsson Orbitalen im superdeformierten Minimum von ^{237}Pu

In der vorliegenden Arbeit wird ein Experiment zur Spektroskopie im superdeformierten 2. Minimum der doppelhöckrigen Spaltbarriere von ^{237}Pu vorgestellt, mit dem erstmals in einem Formisomer mit ungerader Neutronenzahl Einteilchenzustände identifiziert und mit ihren Nilsson-Quantenzahlen charakterisiert werden konnten. Nachdem in den gerade-gerade Nachbarkernen bereits Rotations- (^{236}fU und ^{240}fPu) sowie Vibrationszustände (^{240}fPu) bekannt sind, wurden jetzt die beiden Spaltisomere von ^{237}Pu ($t_{1/2} = 115\text{ns}$ bzw. $1.12\ \mu\text{s}$) am Kölner Tandem-Beschleuniger in einem γ -Spektroskopie-Experiment untersucht. Dabei wurden in der $^{235}\text{U}(\alpha,2\text{n})$ -Reaktion mit einem gepulsten α -Strahl die Zustände im 2. Minimum populiert. Nach dem prompten Zerfall der angeregten Zustände zum Grundzustand der Formisomere spaltet der Kern verzögert mit der jeweiligen Halbwertszeit, die resultierenden Spaltfragmente wurden in einem eigens gebauten 4π Parallelplatten-Detektor nachgewiesen. Die extrem seltenen isomeren γ -Zerfälle wurden in Koinzidenz zu den Spaltfragmenten mit dem hocheffizienten MINIBALL Detektorsystem identifiziert.

Das untergrundkorrigierte γ -Spektrum konnte in die Beiträge der beiden Formisomere zerlegt und 9 Rotationsbanden konnten identifiziert werden, die auf den Grundzustandsbanden der zwei Isomere aufbauen. Die Grundzustands-Spins der beiden Formisomere konnten zu $I=5/2$ (115 ns - Isomer) und $I=9/2$ (1120 ns - Isomer) bestimmt werden. Aus den 149 identifizierten γ -Übergängen wurde für die beiden Spaltisomere in ^{237}Pu jeweils ein eigenes Niveauschema erstellt, dessen Konsistenz durch den Nachweis verbindender γ -Übergänge zwischen den Rotationsbanden gestützt wird. Darüberhinaus konnten die beiden isomeren Teil-Niveauschemata zu einem gemeinsamen Bild verknüpft werden, indem der Grundzustand des langlebigen $9/2$ -Isomers nun $54.0(3)\text{ keV}$ oberhalb des kurzlebigen $5/2$ -Isomers angesiedelt werden konnte. Das detaillierte Niveauschema wurde mit Hartree-Fock-Bogoliubov Einteilchen-Rechnungen, sowie Rechnungen im Rahmen des Nilsson-Modells und Woods-Saxon Potentials verglichen. Dieser Vergleich erlaubte zum ersten Mal eine Identifizierung von Nilsson-Quantenzahlen im 2. Minimum von Aktinidenkernen. Im Zuge dieser Arbeit wurden die Nilsson Einteilchen-Zustände $5/2^+[862]$ und $9/2^+[624]$ für die beiden Isomeren-Grundzustände in ^{237}Pu und $3/2^- [512]$ und $7/2^- [514]$ für zwei angeregte Bandenköpfe, anhand von Einteilchen-Rechnungen identifiziert, die erstmals den deformierten Schalenabschluß $N = 146$ im zweiten Potentialminimum reproduzieren konnten. Die Identifizierung von Nilsson-Orbitalen im zweiten Minimum werden einen wichtigen Beitrag zur Bestätigung und Verbesserung von Kernmodellen liefern und es ermöglichen, die daraus resultierenden Vorhersagen im Bereich der Superschweren Elemente insbesondere in Bezug auf Spaltbarrieren von neutronenreichen Kernen entlang des r-Prozess-Pfades zu verbessern.

Identification of Nilsson Orbitals in the Superdeformed Minimum of ^{237}Pu



In this thesis, a spectroscopy experiment in the second minimum of the double humped fission barrier of ^{237}Pu is presented, in which, for the first time, single-particle states for a neutron-rich shape isomer with odd neutron number were identified and characterised by their Nilsson quantum numbers. While rotational (^{236}fU and ^{240}fPu) and vibrational excitations (^{240}fPu) had already been identified earlier in the even-even neighbouring nuclei, now the fission isomers in ^{237}Pu ($t_{1/2} = 115\text{ns}/1.12\ \mu\text{s}$) were investigated in a γ -spectroscopy experiment at the Cologne Tandem accelerator. Using the $^{235}\text{U}(\alpha, 2n)$ reaction with a pulsed α beam, states in the second minimum were populated. Following the prompt decay of excited states into the ground states of the two shape isomers, the nucleus decays with its half-life, the resulting fission fragments were detected in a specially built 4π parallel plate detector. The extremely rare isomeric γ decays were measured in coincidence with the fission fragments using the highly efficient MINIBALL spectrometer.

The background-subtracted γ -ray spectrum was disentangled into contributions from the two shape isomers and 9 excited rotational bands were identified built on the ground states of the two isomers. The ground state spins of the two shape isomers were determined to be $I = 5/2$ (115 ns isomer) and $I = 9/2$ (1120 ns isomer). From the 149 identified γ transitions, independent level schemes were constructed for the two fission isomers in ^{237}Pu . The consistency of these level schemes was supported by the connecting γ transitions between rotational bands. Furthermore, both level schemes could be combined to a common level scheme, in which the ground state of the long-lived $9/2$ isomer was placed $54.0(3)$ keV above the ground state of the short-lived $5/2$ isomer. The resulting level scheme was compared to Hartree-Fock-Bogoliubov single-particle calculations, Nilsson model and Woods-Saxon potential calculations. This comparison allowed for the first time an assignment of the Nilsson quantum numbers. In the course of this thesis the $5/2^+[862]$ and $9/2^+[624]$ Nilsson single-particle states were identified for the ground states of the two isomers in ^{237}fPu as well as $3/2^- [512]$ and $7/2^- [514]$ for excited rotational bands, for the first time based on calculations reproducing the deformed magic neutron number $N = 146$. The identification of Nilsson orbitals will provide an important input for the validation and improvement of theoretical nuclear models and will lead to improved predictions for fission barriers and their extrapolations to neutron-rich heavy elements in the mass region of the r-process path of the astrophysical nucleosynthesis.

Contents

Motivation	12
1 Introduction	15
2 Theoretical description of nuclear single particle states	25
2.1 Spherical shell model	27
2.2 Deformed shell model- Nilsson Model	30
2.2.1 Woods- Saxon potential	34
2.3 Relativistic Mean Field	34
2.4 Relativistic Hartree- Fock Bogoliubov calculations	41
3 Planning of the Experiment and Experimental Set up	43
3.1 Isomeric yield considerations for $^{237\text{f}}\text{Pu}$	44
3.2 Experimental set up	45
3.2.1 MINIBALL Detector	46
3.2.2 Parallel Plate Avalanche Counter (PPAC) array	47
3.3 Readout electronics and data acquisition	55
3.4 Hardware trigger	56
3.5 The experiment	56
4 Preparation of experimental data	59
4.1 Event building	59
4.2 PPAC data calibration	61
4.3 MINIBALL data calibration	63
4.3.1 MINIBALL photopeak efficiency	64
4.3.2 MINIBALL time calibration	67
4.3.3 Background correction	69
5 Extraction of experimental results	73
5.1 Disentanglement of the γ spectrum	73
5.1.1 Isomer - specific γ - ray spectra	75
5.2 Search for rotational bands	78
5.3 Angular distribution	83

6 Discussion of the experimental results	85
6.1 Construction of fission - isomeric level schemes	86
6.2 Lifetime considerations	93
6.3 Comparison to theoretical single - particle level schemes	95
6.3.1 Early Woods - Saxon - type calculation	95
6.3.2 Comparison of experimental results to Nilsson calculations	97
6.3.3 Relativistic Hartree - Fock Bogoliubov calculations	102
7 Conclusions and Outlook	105
A Table of γ - energies and relative intensities	107
B Solar Cells	111
B.1 Design and technical realisation of the solar cell detector array	112
B.2 Offline Measurements	114
B.3 Online Measurements Munich	117
B.4 Online Measurements Cologne	121
Conference Presentations	128
Poster Presentations	128
Oral Presentations	129
Curriculum Vitae	130
Academic Education	130
Practical Education	131
Teaching Experience	131

List of Figures

1.1	Fission barrier for ^{237f}Pu	16
1.2	Island of fission isomers on the chart of nuclides	17
1.3	Schematic overview of the multiple fission barrier in light actinide isotopes	18
1.4	Schematic overview of collective surface vibrations	20
1.5	Energy levels of a (prolate) deformed harmonic oscillator model potential.	22
1.6	Single-particle neutron energy levels in the second minimum	23
2.1	Comparison of levels arising through the use of different central potentials in the shell model	28
2.2	Nilsson diagram for neutrons, $N \geq 126$	33
2.3	Binding energy per nucleon vs. Fermi wave number for nuclear matter computed from the linearised theory.	38
3.1	Expected nuclear structure in the second minimum of ^{237}Pu	44
3.2	Excitation functions for the isomeric- to- prompt- fission yield ratios in ^{237f}Pu	46
3.3	Schematic view of the experimental set up used in the high resolution γ - spectroscopy of ^{237f}Pu	47
3.4	MINIBALL spectrometer as used for the present experiments on ^{237f}Pu	48
3.5	Photograph of the segmented PPAC anode board.	49
3.6	Picture of the 4π PPAC array in its target chamber	50
3.7	Example of the fission fragment time of flight	51
3.8	Construction of a PPAC module	52
3.9	Schematic top on view of a PPAC counter	53
3.10	Anode back plate and the two epoxy spacer frames for a PPAC module	53
3.11	The PPAC array	55
3.12	Block diagram of the trigger electronics.	57
4.1	Example of the event building process	60
4.2	Time structure of the events recorded	60
4.3	Time structure of γ rays in one of the individual MINIBALL Ge detectors	61
4.4	Typical anode time spectrum of a PPAC	62
4.5	Typical cathode time spectrum from one of the eight PPAC modules	63

4.6	Fission time spectrum of the first 24 hours of beam time	64
4.7	Energy calibration curve for γ rays detected in a typical MINIBALL germanium detector	65
4.8	γ -ray energy spectrum following the $^{235}\text{U}(\alpha, 2n)$ reaction measured with all MINIBALL detectors.	66
4.9	Absolute γ -ray photopeak efficiency for the MINIBALL detector array.	67
4.10	Calibrated time structure of γ rays in one of the individual MINIBALL Ge detectors	68
4.11	Energy-time correlation of γ rays registered in one of the germanium detectors.	68
4.12	Energy dependent time resolution of a typical germanium γ -ray detector.	69
4.13	Timing correlation between fission fragments and γ rays	70
4.14	Background corrected γ -ray spectrum	71
5.1	Time spectrum of fission fragments measured with respect to the prompt beam pulse	74
5.2	Example of an individual γ - transition halfife	75
5.3	Spectrum of lifetimes for the 149 γ transitions.	76
5.4	Energy spectrum of prompt γ rays in coincidence with delayed fission fragments	77
5.5	Energy spectra of γ rays in coincidence with isomeric fission decay from the two isomers	79
5.6	Example of a rotational γ -ray spectrum for an odd-neutron even-proton arbitrary rotational band.	80
5.7	γ -ray energy spectrum in coincidence with isomeric fission decay from the 115 ns isomer with indicated rotational bands	81
5.8	γ -ray energy spectrum in coincidence with isomeric fission decay from the 1120 ns isomer with 4 rotational bands	82
5.9	Angular distribution for the rotational band head γ transition at 573.9 keV	84
6.1	Rotational bands in the first minimum of ^{237}Pu	86
6.2	Moments of inertia of rotational bands in the second minimum of ^{240}Pu , ^{239}Pu and ^{237}Pu	87
6.3	Decay scheme deduced for the 115 ns isomer	89
6.4	Decay scheme deduced for the 1120 ns isomer	90
6.5	Energy spectra of γ rays in coincidence with isomeric fission decay from the two isomers	91
6.6	Level scheme of the second minimum of ^{237}Pu	92
6.7	Proposed decay scheme of the 2.6 ns isomer in ^{239}Pu	94
6.8	Single-neutron energies as a function of β_2 for a deformed Woods-Saxon potential for ^{237}Pu	96
6.9	Proposed single-particle states from a Woods-Saxon calculation versus experimental findings	97
6.10	Magic neutron numbers for different β_4 values and constant β_2 , κ and μ	98

6.11	Evolution of magic neutron numbers for constant $\beta_4 = 0.4$ and $\beta_2 = 0.6$	99
6.12	Evolution of the single particle energies in ^{237}Pu as a function of β_2	100
6.13	Theoretically proposed single- particle states versus experimental findings	101
6.14	Energy surface for ^{237}Pu using a HFB diagonalisation	102
6.15	Single- particle states for neutrons in ^{237}Pu at $\beta_2 = 0.6$ using a HFB diagonalisation	103
B.1	Typical ASE TE16SF solar cell with and without its carrier board	112
B.2	shows a solar cell of Type ASE TE16SF prior to etching in a 10 % HF solution and a solar cell after etching for 10s	113
B.3	A solar cell preamplifier (Saclay design).	113
B.4	Preamplifier and shaper signals as seen from an oscilloscope screen	113
B.5	Schmitt-Pleasanton reference spectrum of the fission fragment mass distribution of ^{252}Cf	114
B.6	Typical energy spectrum of spontaneous fission from a ^{252}Cf source.	115
B.7	Angular- dependent response of two types of solar cells	116
B.8	Readout electronics used in the solar cell test experiments	117
B.9	Prompt fission fragment energy spectrum following the $^{235}\text{U}(\alpha, f)$ reaction	118
B.10	Energy versus time spectrum for the $^{235}\text{U}(\alpha, f)$ reaction	118
B.11	Schematic view of the 4π solar cell array set up	119
B.12	A 4π solar cell detector array	120
B.13	Prompt fission fragment energy spectrum following the $^{235}\text{U}(\alpha, 2n)$ reaction	121
B.14	Time resolution of solar cells	122

Motivation

Models to describe nuclear systems have been developed ever since the discovery of the nucleus by E. Rutherford in 1907 [POV01]. One of the first major successes in the forties was the "shell model" [BOH69]. The "magic" nucleon numbers, which were found to have a "stabilising" effect on the nucleus, were explained by this model. Another model, developed in the sixties by Bohr and Mottelson, describes the nucleus from a geometrical point of view, where the excitation spectrum is explained by the dynamics of a rotating or vibrating small sphere (much like a "liquid drop"). Although these models provide a partial description of the nuclear medium, the microscopic understanding of the strong (residual) interaction between nucleons remained problematic. In order to understand effects of the microscopic strong interaction on the nuclear structure, also new experiments are needed on isotopes where no data was available.

Most of the atomic nuclei we know are at least slightly deformed, only in very stable configurations, given by the magic nucleon numbers, spherical nuclei can be found [RIN80]. However, while typical nuclear deformations can be described by an axis ratio of a rotational ellipsoid of about 1.3:1, in the region of the actinide nuclei 'superdeformed' nuclei can be found with axis ratios of 2:1 (with a rugbyball-like prolate nuclear shape) [THI02]. They represent specific configurations, where the nuclear potential energy surface exhibits a second (superdeformed) potential minimum at such large deformations (besides the normally-deformed usual first minimum with its nuclear ground state). These states are called 'shape isomers' (due to their large life time) or 'fission isomers' (because they predominantly decay via delayed fission after their isomeric lifetime).

Investigating such shape isomers one can probe the nuclear single-particle structure at large deformations needed for the improvement of theoretical calculations used to describe the nuclear landscape [RIN80]. So far, no knowledge of excited single-particle states in superdeformed actinides exists. Spectroscopy of odd-neutron single-particle states can result in a more detailed knowledge of the internal structure of nuclei such as the coupling of the outer neutron to the core of the nucleus. For this reason in this work the single-particle structure of ^{237}fPu was investigated, and spectroscopic results are compared to currently available theoretical calculations. Only if nuclear models are consistently able to reproduce experimental findings one can reliably apply these to regions so far experimentally unaccessible. This can lead to refined models of the ground-state properties of e.g. superheavy elements or fission barrier calculations predicting the lifetime of nuclei along the r-process path [THI02].

In earlier work rotational, and vibrational excitations in even-even actinides (^{236}fU and

$^{240\text{f}}\text{Pu}$ [REI95, PAN00, GAS01]), $^{240\text{f}}\text{Pu}$ and the isomeric ground state single-particle states in $^{239\text{f}}\text{Pu}$ [BAC79], were identified. In this work the excited rotational single-particle states built on the two shape isomers ($t_{1/2} = 115$ ns and $t_{1/2} = 1120$ ns, respectively) in $^{237\text{f}}\text{Pu}$ were investigated via the $^{235}\text{U}(\alpha,2\text{n})$ reaction at 24 MeV. The experiment was performed at the Cologne Tandem accelerator using the highly efficient MINIBALL Ge-detector set up [EBE01]. The identified level scheme is presented and compared to single-particle calculations allowing for the first time an assignment of Nilsson quantum numbers for actinide fission isomers.

In chapter 1 a brief overview of the identification of fission isomers will be given describing the evolution from experiments probing two-quasiparticle states in the actinide region to first experiments testing the single-particle structure in this exotic nuclear region. Chapter 2 gives an introduction to theoretical models which are used to predict the properties of single-particle levels in the superdeformed actinide region. In chapter 3 an overview of the experimental characteristics and the experimental planning of our investigations in $^{237\text{f}}\text{Pu}$ is given. Chapter 4 describes the preparation of the experimental data obtained during the MINIBALL campaign at the IKP in Cologne, leading to the extraction of experimental results on the excitation structure in the second minimum of $^{237\text{f}}\text{Pu}$ presented in chapter 5. Chapter 6 is dedicated to a discussion and interpretation of the experimental results. This thesis is concluded in chapter 7 with a summary of the results obtained in this thesis and an outlook to further possible experiments. Appendix A gives a compilation of the γ -ray transitions identified in this thesis, while appendix B contains a detailed description of a fission fragment detector array comprised of solar cells developed within the framework of this thesis project.

Chapter 1

Introduction

The discovery of nuclear fission by Hahn and Strassmann in 1939 [HAST39] and the first qualitative descriptions of the fission process by Meitner and Frisch [MEI38] and more quantitative studies by Bohr and Wheeler [BOWH39], by examining the interplay between the attractive forces of the nucleons and the repulsive electromagnetic forces within the liquid drop model, led to the first concept of a fission barrier. In 1962 Polikanov et al. [PODR62] observed very short-lived fissioning states ("fission isomers") with a half-life of 14 ms, when bombarding a ^{238}U target with a beam of ^{16}O particles. Furthermore, in 1966 Bjørnholm and coworkers measured the excitation energy of the 0.9 ms isomer in ^{240}Am to be 3.15 (25) MeV [BJO67]. It was inexplicable how an excited state at 3.15 MeV and a lifetime of 0.1 ms could remain stable with respect to γ decay. The first explanation was that these states were metastable high-spin states with spin values larger than $20\hbar$. Measurements by Flerov et al. [FLE68] showed no increase in isomeric yield when using heavy ions instead of light projectiles in order to increase the transferred spin in the reaction, thereby excluding such high-spin states. The consistent theoretical interpretation of these states was given in a series of studies by Strutinsky [STR67, STR68]. In the picture outlined there, these fission isomers result from a second deformed minimum which arises from a superposition of microscopic shell corrections on top of the rather unstructured macroscopic part of the deformation energy described by the liquid drop model. This scenario is illustrated in Fig. 1.1, where the potential energy curve as a function of the nuclear deformation is shown for the case of ^{237}Pu studied within the present work. Strutinsky therefore concluded that the spontaneously fissioning states observed by Polikanov et al. were in fact shape isomers indicating a large nuclear deformation. Fission isomers are ground states in a "second minimum" of a double-humped fission barrier.

The first experimental evidence that fission isomers indeed have a larger deformation than the ground state was given by Specht et al. [SPE72]. By measuring the conversion electrons in coincidence with delayed fission events, transitions in a rotational band built on the 3.8 ns fission isomer of ^{240}Pu were identified. The moment of inertia of this rotational band was found to be 2.2 times larger than that of the ground state rotational band, exhibiting a rotational parameter $\hbar^2/2\theta = 3.343(8)$ keV. Final proof that fission isomers indeed represent (superdeformed) nuclear shapes was given by the determination of their quadrupole moments via lifetime measurements

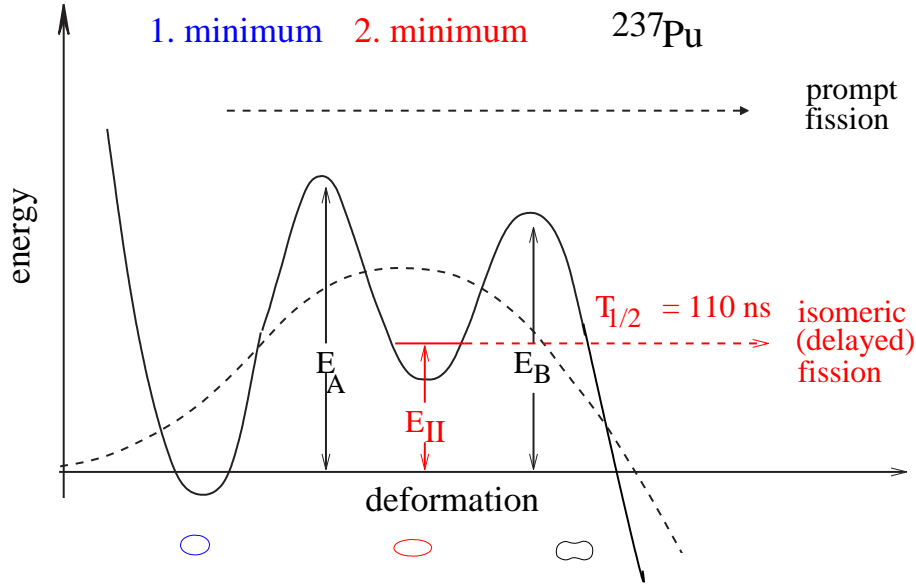


Figure 1.1: Double-humped fission barrier for ^{237}Pu ($E_A = 5.9 \pm 0.3$ MeV, $E_B = 5.2 \pm 0.3$ MeV) [BJO80]. The dashed line describes the unstructured potential barrier as described by the (macroscopic) liquid drop model. The solid line shows the qualitative description of the potential energy as a function of the nuclear deformation, including shell effects according to the Strutinsky model.

of rotational states, resulting in typical values of the intrinsic quadrupole moment $Q_0 \approx 30$ eb, corresponding to an axis ratio of about 2:1 for prolate deformed nuclei [MET80].

The fission isomeric half-lives presently known range from 5 ps to 14 ms and are thus 24-30 orders of magnitude shorter than those for spontaneous fission from the respective nuclear ground states. Figure 1.2 shows a part of the nuclear chart summarising the knowledge of fission isomers. Shape isomers with an axis ratio of 2:1 are known to exist in the actinide regime from $Z = 92$ (Uranium) to $Z = 97$ (Berkelium) and for $141 \leq N \leq 151$. The localisation of fission isomers in the actinide region can be understood from an analysis of the observed half-lives within the framework of the doubly-humped fission barrier. Shell corrections to the nuclear binding energy, which are typically of the order of some MeV, only lead to significant structures in the fission barrier if the smoothly varying macroscopic part of the deformation energy is small. This solely occurs in the actinide region, due to a near cancellation between the surface tension and the Coulomb force. From an analysis of the measured lifetimes it was concluded that the highest stability for fission isomers is around the magic superdeformed neutron number $N = 146$ [MET74]. With increasing proton number, the outer barrier is lowered due to the decrease in the liquid drop part of the fission barrier, rendering the search for actinide fission isomers so far experimentally impossible for nuclei with $Z > 97$, as their lifetimes are too short to be measured. For lighter actinides the inner barrier becomes smaller and more penetrable, enabling a γ back decay to the ground state of the first minimum, which is then more favourable than delayed fission from the second minimum through the outer barrier.

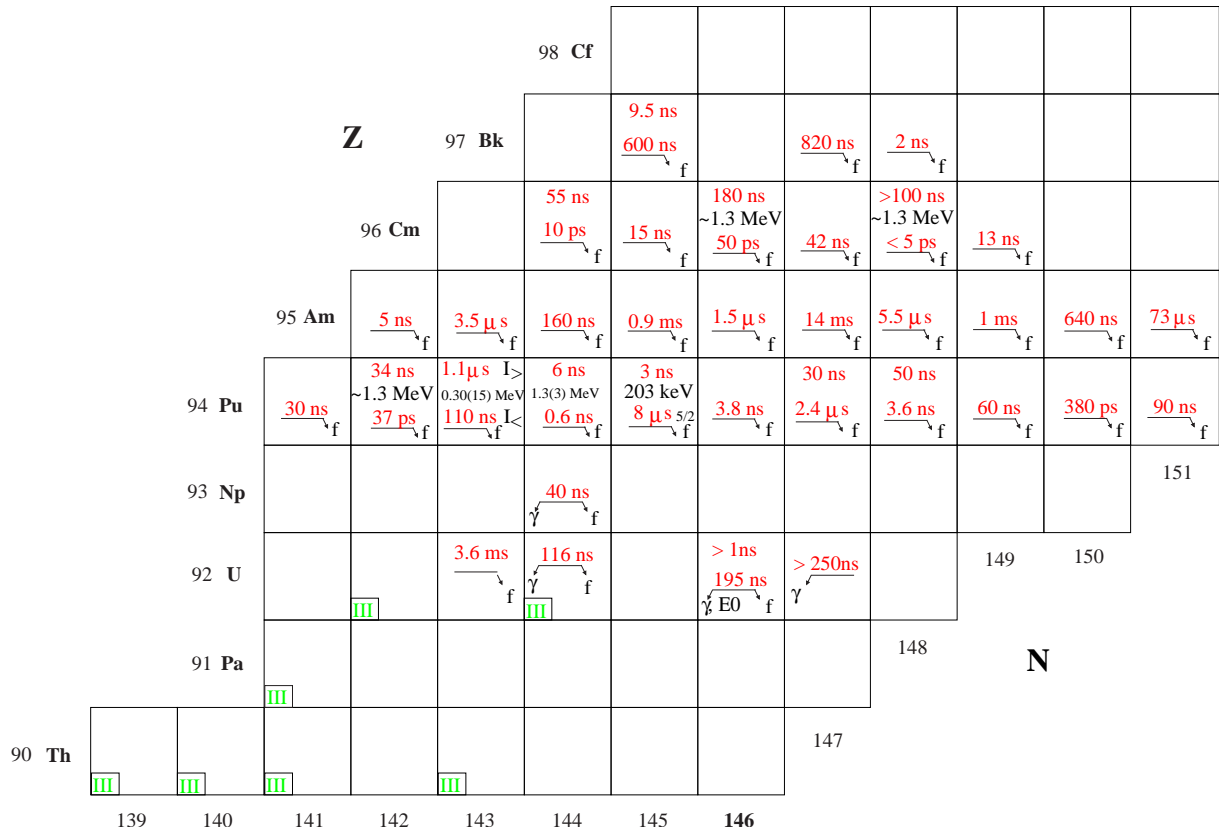


Figure 1.2: Extract from the nuclear chart showing the "island of fission isomers" with half-lives of all presently known 35 fission isomers in the actinide mass region. Those nuclei, where a γ -back decay to the first minimum has been identified are marked with a γ . For those nuclei where two fission isomers are known, two lifetimes and the assumed energy between the ground states of these isomers are given. Those nuclei, where a hyperdeformed third minimum in the potential energy surface has been experimentally established, have been marked with the green index III [THI03, OBE07].

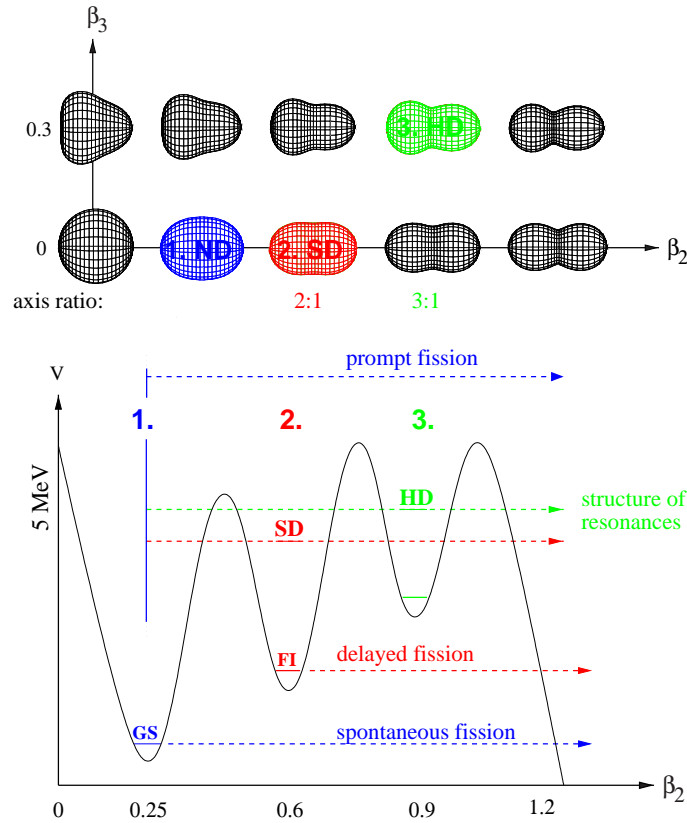


Figure 1.3: Schematic overview of the multiple-humped fission barrier in light actinide isotopes together with the corresponding nuclear shapes. Lower part: cut through the potential energy surface along the fission path (β_2 path), revealing a superdeformed (SD) second minimum at an axis ratio of 2:1 and a hyperdeformed (HD) third minimum at an axis ratio of 3:1 [THI03]. The energy and location of the saddle points and minima (except for the third one) were taken from [HOW80], while the energy of the third minimum was taken from [CWI94]. The energy scale was slightly shifted in order to reproduce the energy of the ground states in the first well. In the upper part the corresponding nuclear shapes are displayed with of the quadrupole and octupole degrees of freedom. From [HUN99].

Additionally indicated in Fig. 1.2 is the region between the Thorium and Uranium isotopes, where a third potential well has already been experimentally identified [THI03]. For the lighter actinides the outer barrier becomes thicker and is further split in half. Fig. 1.3 displays a cut through the potential landscape along the fission path (similar to the curve shown in Fig. 1.1) for such a situation. In addition to the already discussed appearance of the second minimum here also a third well is shown in the fission barrier, as theoretically predicted and experimentally observed e.g. in the Thorium and Uranium isotopes [BLO89, HAB99, KRA98]. Going from the normal deformed first minimum to the second well, the quadrupole deformation parameterised by β_2 increases from an axis ratio of about 1.3:1 to the superdeformed axis ratio of 2:1, while in the hyperdeformed third minimum with an axis ratio of 3:1 reflexion-asymmetric octupole deformed nuclei (characterised by β_3) can be found, as illustrated in the upper part of Fig. 1.3.

In the superdeformed second minimum of actinide nuclei the same excitation modes are expected as in the normally deformed first minimum. (Non-collective) quasi-particle excitations predominantly appear above the pairing energy, which for normally deformed even-even nuclei lies at approximately 1.2 MeV. Below this energy only collective excitations are expected. From the appearance of 2-quasiparticle isomers the pairing-energy in the second minimum is also expected to be ~ 1.2 MeV [BJO80]. Similar to the normally deformed first minimum, the rotational band built on the isomeric ground state is the lowest-lying collective excitation. In the second minimum the energetic distance of the rotational states is much smaller due to the increased moment of inertia Θ . The spin-dependent energy of the rotational band members is given by $E_{\text{rot}} = A \cdot I(I + 1)$, where the rotational parameter is $A = \hbar^2/2\Theta$ with a typical value of $A \approx 3.4$ keV [THI02] for superdeformed isomers in the second potential minimum of actinides. Besides the ground state rotational band in the collective model of Bohr and Mottelson [BOM75], (collective) surface vibrations with excitation energies predicted to range below the pairing-gap are expected for superdeformed isomers.

Surface vibrations in the rest frame of the nucleus can be expanded into multipoles. The lowest vibrational modes are quadrupole and octupole excitations. The quadrupole part leads to a β vibration along the symmetry axis of the nucleus or to a γ vibration perpendicular to its symmetry axis. The K quantum number, used to characterise collective vibrations, is given by the projection of the nuclear spin onto the symmetry axis of the deformed nucleus, where β - and γ -vibrations are characterised as $K^\pi = 0^+$ and $K^\pi = 2^+$, respectively. The octupole part leads to a quadruplet of states ($K^\pi = 0^-, 1^-, 2^-$ and 3^-).

On each vibrational ground state a rotational band can be excited, whose structure is given by the K -quantum number and the parity of the band head. The energy of the rotational states is approximately given by $E_{\text{rot}}(I) = A(I(I+1) - K(K+1))$, where the spin I for $K \neq 0$ can have values of $I = K, K+1, K+2, \dots$. For $K = 0$ even spins can only have a positive parity, while odd spins can only carry negative parity. Fig. 1.4 schematically shows the collective excitations and the resulting vibrational structure to be expected below the pairing gap. Above the ground state rotational band collective quadrupole and octupole surface vibrational excitations are expected, similar to the first minimum. On top of every vibrational excitation a rotational band occurs.

Non-collective quasi-particle excitations represent a further type of excited mode upon which rotational bands can be built. They only appear above the pairing energy, which ranges between 1.2 and 1.4 MeV for even-even actinide nuclei. In a γ -spectroscopic study of ^{236}fU , using the Darmstadt-Heidelberg crystal ball, first indications of β - and γ -vibrations and the ($K^\pi = 0^-$)-octupole band were observed by P. Reiter et al. [REI93, REI95]. In this experiment the limited resolution of this NaI detector system emphasised the need of high-resolution γ spectroscopy for this kind of studies. Consequently the shape isomer of the even-even nucleus ^{240}Pu , with a magic neutron number of $N = 146$, where the largest stability of fission isomers is located [MET74], was studied by Pansegrau et al. using an efficient germanium detector setup [PAN00]. The superdeformed second minimum was populated using the $^{238}\text{U}(\alpha, 2n)$ reaction and excited states built on the ground state rotational band, measured by Specht et al. [SPE72],

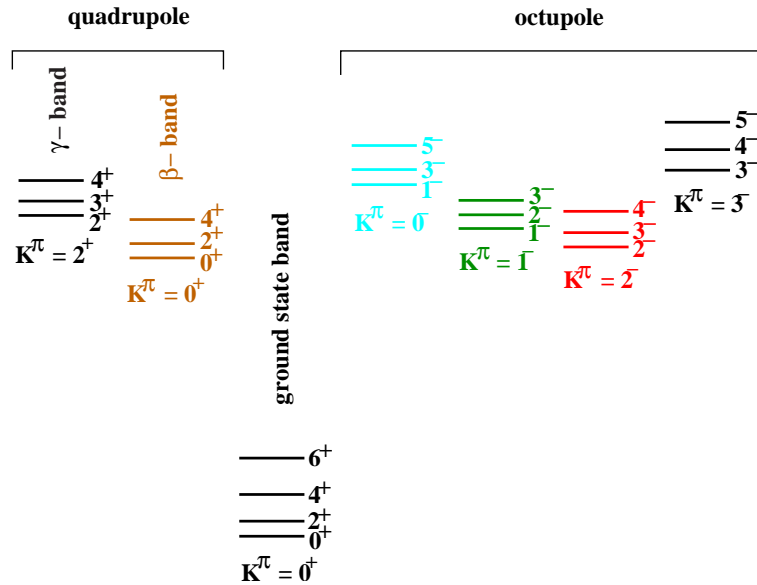


Figure 1.4: Schematic overview of the band structure of reflexion-symmetric collective surface vibrations below the pairing gap in an even-even nucleus. From [VAN73].

were investigated. As it turned out, these γ -spectroscopic data had to be complemented by conversion electron measurements [GAS02] in order to allow for a consistent interpretation, resulting in the most detailed level scheme so far available for nuclei in the second potential well including two quasi-particle excitations. In fact, more spectroscopic information was available in the second minimum for ^{240}Pu as compared to the normally deformed first well. In addition, the structure of high-lying multi-phonon transmission resonances around the barrier top was studied, allowing for an identification of previously known resonances with the 3rd and 4th β vibrational phonon [HUN01].

Besides the superdeformed fission isomers in the actinide region, superdeformation, i.e. the appearance of a strongly deformed second potential well, is a general phenomenon in nearly all other mass regions, however restricted there to high angular momenta [NOL88, WAR01]. For those nuclei a lowering of the potential in the region of superdeformation occurs for high spins (up to $\sim 60\hbar$) due to the additional rotational energy. Since the depth of the potential well in the region of high-spin superdeformation continuously decreases with lower angular momenta, the decay from the "second" into the "first" minimum ('decay-out') typically occurs for angular momenta between about $10\hbar$ and $30\hbar$. In contrast, the double-humped fission barrier for shape isomers in the actinides already exists at low angular momenta, allowing to reach the ground state of superdeformed nuclei through a population of the second minimum.

Spectroscopic studies in fission isomers are extremely difficult from the experimental point of view due to the low production cross sections in the presence of the background component from prompt fission dominating by 5 to 6 orders of magnitude. However, they offer unique advantages for clarifying the nuclear structure of strongly deformed nuclei compared to more conventional spectroscopy in the first minimum. The very different energies for rotational and

vibrational excitations due to the low angular momenta in fission isomers allow for a clear separation between the two, in contrast to the high-spin regime, where Coriolis mixing effects often create a complex spectroscopic situation preventing unambiguous signatures of collective structures. Thus fission isomers offer the unique possibility of detailed spectroscopic studies on collective vibrational excitations in highly deformed nuclei, while no equivalent information has been obtained so far in the high-spin superdeformation regime.

To extend our knowledge in the superdeformed actinide region, it is necessary not only to study collective excitations and the 2 quasi-particle states in even-even nuclei, but it is imperative to identify single-particle states. The liquid drop model is based on the assumption of a homogeneous density distribution in space. Deviations from this homogeneous distribution, i.e. shell structure effects, lead to changes in the binding energies of nuclei from their mass in the liquid drop model. Nuclei with (spherical) magic nucleon numbers such as ^{208}Pb exhibit an increased stability. However, magic nucleon numbers are not only found for spherical nuclei, but also deformed closed shells lead to magic nucleon numbers, i.e. an increased nuclear stability. Fig. 1.5 shows the single-particle energy levels of a (prolately deformed) harmonic oscillator potential as a function of its deformation β . It shows that significant shell gaps occur at axis ratios of 2:1 and 3:1, respectively, corresponding to quadrupole deformations of $\beta = 0.6$ and 0.9. While the configuration at an axis ratio of 2:1 corresponds to the existence of shape isomers in the superdeformed second potential well, the recently established third potential minimum results in hyperdeformed nuclear configurations ($\beta_2 = 0.9$).

The spherically deformed harmonic oscillator potential is not able to explain all experimentally observed magic numbers. In order to reproduce the higher magic numbers a spin-orbit potential is added to the harmonic oscillator. In atomic physics, the spin-orbit interaction is due to the magnetic interaction of the magnetic dipole moment of the electron spin and the magnetic field experienced by the electron in its rest frame as it moves through the Coulomb field. In contrast in nuclear physics the spin-orbit potential cannot be magnetic as this would be very weak. Moreover, in the nucleus the spin-orbit interaction is due to the total spins of the nucleons and the orbital angular momentum is the relative orbital angular momentum between the core of the nucleus and the unpaired nucleons. Inside the nucleus we have a spin-saturated system and the effect will be cancelled. Near the surface, however, that cancellation does not occur and a single nucleon experiences a spin-orbit interaction due to the other nucleons. The cancellation effect causes the strength of the interaction to be largest where the density of nucleons is changing most rapidly [WIL91, EIS70]. The origin of the spin-orbit force in nuclei, in particular its abnormal strength, is now better understood in a relativistic approach to nuclear systems (see chapter 2.3).

For deformed nuclei the spherical nuclear potential used in the shell model is not appropriate, leading to the deformed shell model. The purpose of the Nilsson model (an extension to the deformed shell model) is to produce a basic single-particle model applicable to nearly all deformed nuclei [NIL55]. It accounts for most of the observed features of single-particle levels in hundreds of deformed nuclei (see chapter 2 for a more indepth description of the Nilsson model).

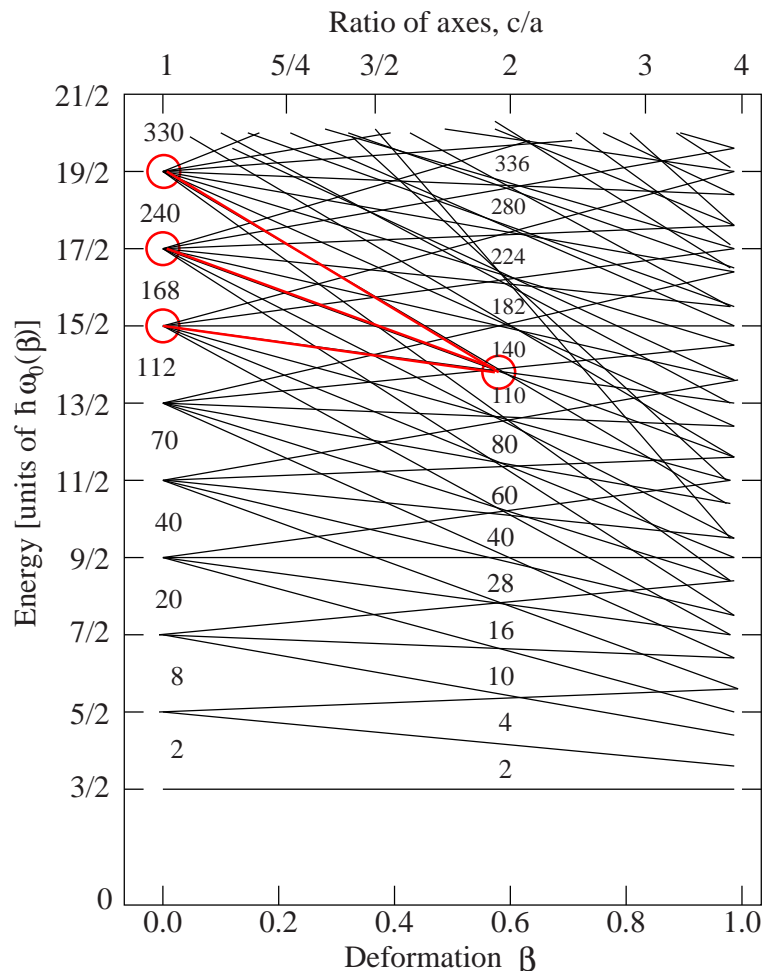


Figure 1.5: Energy levels of a (prolate) deformed harmonic oscillator model potential. Shell gaps at large deformations (axis ratio 2:1, 3:1) are visible. Marked in red are orbitals down-sloping with deformation from higher-lying shells into the region of superdeformed actinides.

According to Strutinsky it is from the level density of such single-particle states that shell corrections to the nuclear binding energy can be calculated. Furthermore Strutinsky realised that fluctuations in the level density, leading to shell closures and fluctuations in the binding energy, are not only dependent on the nucleon number, but also appear for a fixed nucleon number with a varying deformation. For superdeformed shape isomers with an axis ratio of 2:1 around the neutron number 146 large shell corrections of about 3 MeV are found [BJO80]. Shell effects are used as corrections in the calculation of fission barriers, therefore the identification of single-particle states at large deformations is necessary for a better understanding of fission barriers. Since a deviation in the shell correction energy by 1 MeV results in a modification of the fission lifetime by up to 5 orders of magnitude, the identification of single-particle states can therefore improve models describing the ground-state properties of e.g. super-heavy elements.

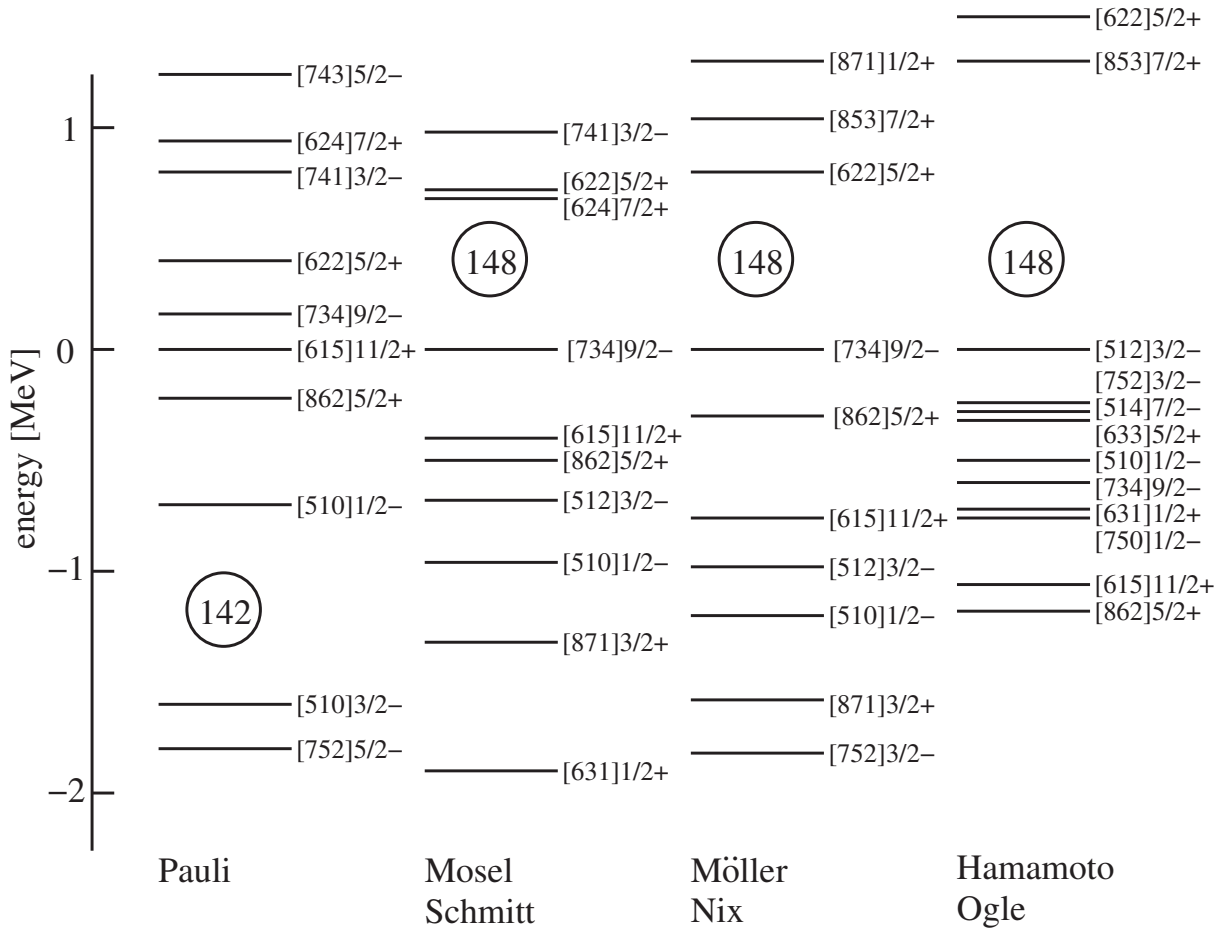


Figure 1.6: Single-particle neutron energy levels at the deformation of the second minimum calculated by different groups [PAU73, MOS71, MOEL73, HAM75] (The quantum numbers will be explained in Chap. 2.2).

Figure 1.6 shows the spectrum of single-particle states calculated by different theory groups for the nucleus ^{237}fPu in the superdeformed actinide region, using either the Nilsson model [MOEL73, MOS71] or a deformed Woods-Saxon potential [HAM75, PAU73]. Shown are one calculation [PAU73] producing a shell closure for $N=142$ on the left of the figure and three

calculations producing a shell closure of $N = 148$ for neutrons to the right of the figure. Experimentally the magic neutron number for superdeformed fission isomers was found to be $N = 146$ [MET74]. As none of these models was able to reproduce this magic number, while even resulting in contradicting predictions of the level sequence, experimental data is required as input to more modern theoretical approaches such as the relativistic Hartree-Fock-Bogoliubov (HFB) theory (see chapter 2 for a more detailed theoretical discussion on the relevant theories). It should be emphasised that prior to our experiments not one excited single-particle orbital was unambiguously identified in strongly deformed actinide nuclei. Thus it was not possible to test the predictive power of theoretical attempts to describe the nuclear structure in this regime. Thus it was the aim of this thesis to study single-particle (Nilsson) orbitals at the deformation of the second minimum, for the first time addressing an odd-neutron fission isomer (^{237f}Pu), using high-resolution γ -ray spectroscopy.

Chapter 2

Theoretical description of nuclear single particle states

The assumption of an approximately independent motion of nucleons in an average potential is the basis of the shell model. For a particular nucleon, this potential represents its interaction with all other nucleons in the nucleus. For spherical nuclei, the nuclear energy is the same whatever the j orientation, thus one can identify states by their spectroscopic notation (s,p,d,f, etc. and l_j). For deformed nuclei, the spherical nuclear potential [RIN80] used in the shell model is no longer a good starting point. In fact, for calculations in a non - spherical potential, the total angular momentum j is no longer a “good” quantum number. Therefore, if the potential has a deformed shape, the energy levels in the deformed potential depend on the spatial orientation of the orbit. More precisely, the energy depends on the component of j along the symmetry axis of the potential in the case of axially symmetric deformation. In chapter 2.2 two different types of deformed shell model calculations are introduced.

Modern nuclear structure theory has evolved from the macroscopic and microscopic studies of phenomena in stable nuclei towards regions of exotic, short-lived nuclei far from the valley of stability, and towards nuclear astrophysics applications. The main challenge is to create a consistent microscopic theoretical framework that will provide a unified description of bulk properties, nuclear excitations and reactions [RIN80]. In a shell model nucleons (or electrons) move in individual orbitals in a common potential. This will always lead to variations in the single-particle energies. When an energy spacing is large, this increases the stability of a configuration filling completely the orbitals up to this state. This is then a “magic” number. The situations, where the level spacing is large (i.e. has a gap) may be different for stable, exotic, or deformed nuclei [WOL08].

For the shell model one distinguishes the independent particle shell model (IPM) and the interacting shell model (SM):

1. IPM: particles move without mutual interaction in the potential. One classifies two types of IPM's.
 - (a) Phenomenological IPM: The potential is parameterised empirically, e.g. as a harmonic

oscillator or a Woods-Saxon potential (see chap. 2.1). It may also be deformed (Nilsson model, see chap. 2.2). Using this approach the experimentally observed magic numbers were first independently reproduced by Haxel, Jensen, Suess and Goeppert-Mayer [HAX49, MAY49].

- (b) Microscopic IPM: The potential is calculated as the average field of the other particles (mean field). The simplest methods are the Hartree or Hartree-Fock (HF) approximation (see also chap. 2.3). This is a self-consistent approach to solve the many-body Schrödinger equation. The wave function in this approximation is an antisymmetric product of the single-particle wave functions for this mean field [RIN80, VRE05].
2. SM with interactions: The nucleons in the orbitals (as in 1.) interact with each other due to the residual interactions, which are not yet taken into account in the mean field potential. IPM models take into account only the long-range part of the nuclear force, while the SM with interactions also takes into account the short-range part of the nucleon-nucleon interaction, and include the corresponding short-range correlations. Again there are two types of SMs with residual interaction:
- (a) In the first, only pairing interactions are taken into account. This is a special residual interaction, which describes the dominant interaction between the orbitals with $|jm\rangle$ and $|j-m\rangle$. It can be treated in the BCS method. Combined with the HF method it is called the Hartree-Fock-Bogoliubov (HFB) theory. It can still be formulated as an IPM, but with "quasi-particles" (these do not have a fixed particle number) [RIN80, VRE05].
 - (b) General residual interactions. The residual interaction is diagonalised in a space of IPM states. This space can be very large for many particles in many orbitals, i.e. in heavier nuclei. There are many modern techniques to treat these problems.
 - i. Conventional: truncated model space (usually with inert core) (e.g. sd shell) and empirical interactions.
 - ii. no-core SM (NCSM) large spaces without core. Consistent calculation of effective interactions adjusted to the model space [NAV96].
 - iii. Monte-Carlo SM (MCSM) or Shell-model Monte-Carlo (SMMC). Sampling of configurations according to the importance in changing the energy [LAN93, LAN95].
 - iv. Greens-function Monte-Carlo (GFMC) GF techniques to evolve a trial wave function to the ground state [CAR87].

As a second classification, a model can be formulated non-relativistically (i.e. with the Schrödinger equation) or relativistically (i.e. with the Dirac equation). This can be done (but has not always been done) for all of the above models. Relativistically one uses the methods of quantum field theory. It is formulated not with a many-body Hamiltonian but with a Lagrange density (\mathcal{L}). The model is an interacting system of nucleons (p, n, possibly excited nucleons

like Δ or N^*) and mesons (σ , ω , ρ , δ , π ...). The Lagrangian has to be postulated (i.e. it is not derived from QCD but symmetries are retained) and different assumptions correspond to different energy densities as a function of density. It is thus related to energy density functional (EDF)-theory. The treatment of the Lagrangian can be done in various ways:

1. Phenomenological ("Walecka model"): The energy density functional is parameterised, and fitted to nuclear matter and/or finite nuclei [WAL74, WAL95]. There are several versions:

- $\sigma\omega$ model (simplest version with only σ and ω mesons.)
- non-linear (NL) model (self-interaction of σ meson)
- density-dependent coupling model (DDRH)

The models are usually treated in Hartree-approximation (called Relativistic Hartree (RH) or Relativistic Mean Field (RMF)-model), but also RHF has been used. Another approach is RHB, which denotes one of the truncated model space RMF models with pairing included (see chap. 2.4) [BEN03, KUC91, MAN75, PAA07, RIN80].

2. Microscopic relativistic models: One starts from nucleon-meson interactions taken from fits to NN-scattering (realistic interactions). Including higher order correlations and exchange an effective interaction in the medium is calculated. This is then used to calculate the mean field (for nuclear matter or nuclei). The method is called the Brückner-HF (BHF, non relativistic) or Dirac-BHF (or DB, relativistic) method [ANA83, CEL86, HAA87, HOR87, MAC89].

2.1 Spherical shell model

The shell model is partly analogous to the atomic shell model which describes the arrangement of electrons in an atom, where a filled shell results in greater stability. When adding nucleons (protons or neutrons) to a nucleus, there are certain numbers, where the binding energy of the next nucleon is significantly less than for the previous one. This observation, that there are certain magic numbers of nucleons: 2, 8, 20, 28, 50, 82, 126, which are more tightly bound than the next higher number, is the origin of the shell model [HAX49, MAY49].

Note that the shells exist for both protons and neutrons individually, so that we can speak of "magic nuclei", where one nucleon type is at a magic number, and "doubly magic nuclei", where both are. Due to the increased importance of the Coulomb force, the largest magic numbers are 126 and, speculatively, 184 for neutrons, but only ~ 120 for protons. This plays a relevant role in the search of the so-called island of stability in the regime of superheavy elements. Besides, some semi-magic numbers have been found, most noticeably $Z=40$.

The independent particle shell model IPM is based on a Hamiltonian of the form [WOL08]:

$$\mathcal{H} = \sum_i h(i) \tag{2.1}$$

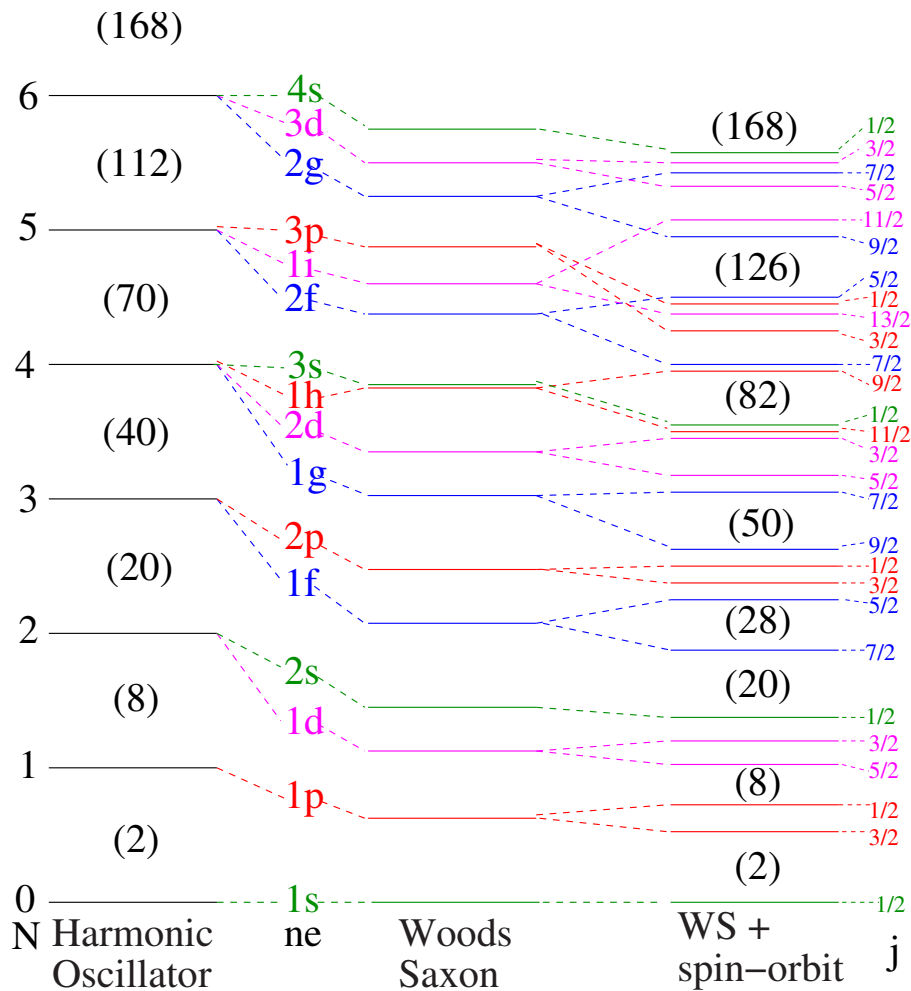


Figure 2.1: Comparison of levels arising through the use different central potentials in the shell model. On the left the level order due to the harmonic oscillator potential is shown, the middle column represents the level ordering if a finite square well (corresponding to Woods-Saxon) potential is used to parameterise the level ordering. Adding a strong spin-orbit interaction to the Woods-Saxon potential, we obtain a level ordering where the gaps in the levels correspond to the experimentally observed "magic" numbers [EIS70].

$$h = \frac{p^2}{2m} + V_{cent}(r) + V_{so}(r)\vec{l} \cdot \vec{s} + V_{Coul}(r) + V_{Lane}(r) \quad (2.2)$$

where $\frac{p^2}{2m}$ is the kinetic energy. $V_{cent}(r)$ is the central potential. It is often parameterised as a harmonic oscillator, as this is analytically solvable. The potential is created by strong short-range forces and is thus proportional to the nuclear density. Therefore a finite depth model square well potential is often considered. A more realistic potential is given by the Woods Saxon potential:

$$V_{cent} = V_0 \frac{1}{1 + \exp(\frac{r-R}{a})}. \quad (2.3)$$

where R is the radius and a the surface thickness. The third term of equation 2.2 is the spin-orbit interaction. It is the interaction of the spin and orbital angular momentum of individual nucleons. In atomic physics it is the relativistic (magnetic) effect of the spin magnetic moment with a magnetic field of orbital motion. It is found to be:

$$V_{so}(r) = \lambda \frac{\hbar}{mc} \frac{1}{r} \frac{\partial V_{cent}}{\partial r}, \quad (2.4)$$

with $\lambda = 1/2$. However, in nuclear physics the contribution is much larger, here we have a strong spin-orbit interaction with $\lambda \approx 10$. With the total angular momentum $j = l \pm 1/2$ the contribution of the spin-orbit term is proportional to:

$$\langle jm|l \cdot s|jm \rangle \sim \frac{1}{2}(j(j+1) - l(l+1) - \frac{3}{4}) \sim \begin{cases} l \\ -(l+1) \end{cases} \quad (2.5)$$

Thus the $j = l + 1/2$ level is lowered, more so for larger l . It is because of this strong spin-orbit interaction that the "magic" shell closures for heavier nuclei are explained. The puzzle is then the abnormal strength of the spin-orbit term, which is understood in the relativistic approach (see chap. 2.3 below). The fourth term $V_{Coul}(r)$ is the Coulomb potential a long-range force, usually described as that of a charged sphere. The fifth and last term $V_{Lane}(r)$ is the isospin dependent (Lane) potential. It is the symmetry energy which arises due to the difference between the proton and neutron potential. It has recently been discussed extensively in connection with exotic nuclei, especially its density dependence [LAN62, FUC06, WOL07].

Fig. 2.1 shows schematically the evolution of single-particle orbitals for different potentials used to describe the shell model. If the nuclear potential were close to that of the harmonic oscillator, the major shell closings would occur at nucleon numbers 2, 8, 20, 40, 70 and 112 (left column). The first three members of the series correspond to the observed major shell closings, whereas the higher-lying ones do not. The choice of a more realistic radial dependence somewhat modifies the detailed sequence of orbits. The main effect is to remove the harmonic oscillator degeneracy in such a sense that the orbits of highest l are depressed with respect to the low l orbits, illustrated in the middle column by the use of a finite depth Woods-Saxon-potential. A decisive step in the development of the nuclear shell model was the recognition that the assumption of a relatively strong spin-orbit interaction in the nucleonic motion leads to a natural explanation of the major shell closings [HAX49, MAY49]. This coupling splits the

levels with $j = l \pm 1/2$, which are degenerate in a spin-independent potential, and if the sign is such as to lower the levels with $j = l + 1/2$, the experimentally observed shell closings are obtained, shown in the right hand column of Fig. 2.1. The sequence of single-particle levels that results when the spin-orbit force is added to the central potential is confirmed by a large body of evidence [BOH69]. The interpretation of the nuclear levels is particularly simple for configurations consisting of closed shells of neutrons and protons with only a single additional particle or with a single particle missing from such a closed configuration.

2.2 Deformed shell model - Nilsson Model

Far from closed shells, i.e. for nuclei around $A \sim 25$ (Al, Mg), $150 < A < 190$ (rare earth nuclei), and for $A > 220$ (actinides), nuclei are permanently deformed. In these regions one has to assume a deformed single particle potential [RIN80]. The assumption of deformation is able to explain many experimental facts, of which the most important is the existence of rotational bands. In the mass regions mentioned above the nuclear excitation spectra show pronounced rotational bands following an $I(I + 1)$ behaviour. Very large quadrupole moments are found, which are directly connected to the strongly enhanced quadrupole transition probabilities. The strongly enhanced $B(E2)$ values within the rotational bands are an indication of stable quadrupole deformations (β_2) [SEG64]. Furthermore, in Coulomb excitation experiments of the rare earth region large hexadecupole matrix elements were found [HEN68], hinting at a stable hexadecupole deformation (β_4).

Also the appearance of short-lived fission isomers ($t_{1/2} \leq 1$ msec) in the actinide region for deformations of $\beta_2 \approx 0.6$ is not described by the spherical shell model. It is clear that large deformations play an important role in the nuclear fission process, for this reason the deformed shell model is needed to explain this process [RIN80]. As was seen in Fig. 1.5, also deformed nuclei can show pronounced gaps in the single-particle spectrum, i.e. "shells", very much analogous to spherical nuclei. Then nuclei in the neighborhood of these deformed shells can be described in terms of single-particle motion, however, in a deformed mean field potential. This is the idea of the deformed shell model, first proposed by Nilsson and thus often called the Nilsson model.

The deformed oscillator potential in the shape of a spheroid may be written as [NIL69].

$$V_{osc} = \frac{1}{2}M[\omega_{\perp}^2(x^2 + y^2) + \omega_z^2 z^2]. \quad (2.6)$$

Nilsson introduced the deformation parameter ε : $\omega_z = \omega_0(\varepsilon)(1 - \frac{2}{3}\varepsilon)$, $\omega_{\perp} = \omega_0(\varepsilon)(1 + \frac{1}{3}\varepsilon)$. The quadrupole part of the potential is obtained up to a second order in ε , as

$$\varepsilon(1 - \frac{1}{\sigma}\varepsilon)r^2P_2(\cos\theta), \quad (2.7)$$

where P_2 is the second order Legendre polynomial. The Nilsson model can be formulated with "stretched" coordinates (ξ, η, ζ) with ξ given by $\xi = x\sqrt{(M\omega_{\perp}/\hbar)}$ (M is the mass) and η

and ζ accordingly. By this one can transform away coupling terms of $r^2 P_2(\cos\theta)$ between shells N and $N \pm 2$. Then to first order in ε the potential can be expressed as

$$V_{osc} = \frac{1}{2}\hbar\omega_0(\rho^2 - \frac{2}{3}\varepsilon\rho^2 P_2(\cos\theta_t)), \quad (2.8)$$

where θ_t is the angle in the stretched coordinates and $\rho^2 = \xi^2 + \eta^2 + \zeta^2$.

At this stage deformations of higher multipoles (e.g. P_4 = hexadecupole) were introduced to the model by adding terms proportional to

$$\varepsilon_3\rho^2 P_3(\cos\theta_t), \quad \varepsilon_4\rho^2 P_4(\cos\theta_t) \quad \text{and} \quad \varepsilon_6\rho^2 P_6(\cos\theta_t).$$

As discussed above, the spin-orbit term is an essential feature of the shell model. Since in the deformed shell model the three available vectors of nucleon motion are its spin s , velocity ν , and gradient of the oscillator potential at the nuclear position, ∇V , the simplest invariant term one may construct is $s \cdot (p \times \nabla V)$. With this a spin-orbit potential is obtained:

$$V_{s.o} \propto \left(\frac{\omega_z}{w_\perp}\right)^{\frac{1}{3}} (l_T \cdot s) + \left(\left(\frac{\omega_\perp}{\omega_z}\right)^{\frac{2}{3}} - \left(\frac{\omega_z}{w_\perp}\right)^{\frac{1}{3}}\right) l_3 s_3 \quad (2.9)$$

In this equation the quantity l_T is defined in terms of the doubly-stretched coordinates $a = (M\omega_0/\hbar)^{\frac{1}{2}}\omega_\perp x/\omega_0$ etc. which transform the harmonic oscillator ellipsoid into a sphere. Presently we approximate this term by $l_t \cdot s$, where l_t is defined in the stretched coordinates (ξ, η, ζ) :

$$V_{s.o} \propto l_t \cdot s \quad (2.10)$$

The harmonic oscillator potential is not satisfactory for higher orbitals. One possibility is to use a finite depth potential, as discussed below. In the Nilsson model a radial correction term is added, that flattens the bottom of the potential more and more with increasing A . It is natural to consider an expansion of the radial dependence of the potential, in which the ρ^2 or r^2 harmonic (oscillator) term is the lowest-order term. The next (anharmonic) term to be considered is then the ρ^4 term, whose matrix elements within one oscillator shell are actually the same as those of $(\frac{1}{2}l^2)$ apart from additive constants. The correction chosen was:

$$V_{corr} \propto \rho^4 - \langle \rho^4 \rangle_N, \quad (2.11)$$

where the second term is the average of the correction within a shell N . Nilsson summarised his single-particle Hamiltonian as:

$$H_{s.p.} = \frac{1}{2}\hbar\omega_0(\varepsilon, \varepsilon_4)[-\Delta_\rho + \frac{2}{3}\varepsilon\frac{1}{2}(2\partial^2/\partial\zeta^2 - \partial^2/\partial\xi^2 - \partial^2/\partial\eta^2) + \rho^2 - \frac{2}{3}\varepsilon\rho^2 P_2(\cos\theta_t) + 2\varepsilon_4\rho^2 P_4(\cos\theta_t)] - 2\kappa\hbar\omega_0(l_t \cdot s - \mu(\rho^4 - \langle \rho^4 \rangle_N)), \quad (2.12)$$

Region	κ	μ
$N, Z < 50$	0.08	0
$50 < Z < 82$	0.0637	0.60
$82 < N < 126$	0.0637	0.42
$82 < Z$	0.0577	0.65
$126 < N$	0.0635	0.325

Table 2.1 Parameters of the Nilsson Hamiltonian [GUS67]

where the first two terms in the square bracket give the kinetic energy. We define ω_0 by $\omega_0^3 = \omega_{\perp}^2 \omega_z$, which enters from volume conservation and is a function of the mass number only. The above Hamiltonian includes only P_2 and P_4 coordinates, and only terms within one shell are considered [GUS67]. κ and μ are adjustable coupling parameters. In practice they are adjusted in each major shell separately. Table 2.1 gives the parameters of the Nilsson Hamiltonian as deduced by Nilsson et al. [NIL55]. It shows that the parameters κ (responsible for the spin orbit force) and μ (shifts levels with higher l -values downwards), vary for different N and Z numbers. In chapter 6.3.2, the experimental spectroscopic results obtained in this thesis are compared to the Nilsson model. The values for κ and μ are chosen such that the experimental levels are described and a first tentative assignment of the single-particle states in the second minimum of ^{237}Pu was performed.

How are the single nucleon orbits described in a deformed nucleus? The interaction of the single nucleon with the underlying core depends on the relative orientation of the orbit with respect to the time-averaged shape of the deformed core. The degeneracy of the substates in the spherical case will be lifted according to the projection of the spin j on the symmetry axis of the deformed nucleus (referred to as the quantum number $\Omega = j, j-1, j-2, \dots$). The amount of energy splitting between the substates depends on the relative interaction of the Ω -orbits with the deformed nucleus.

The Nilsson model describes the evolution of these energy splittings between the K -states as a function of deformation. In Fig. 2.2 the splitting of the single-particle orbits is plotted as a function of ϵ_2 (ϵ : nuclear deformation parameterised in the oscillator model), where $\epsilon_2 \approx 1.05 \beta_2$ [BOH69]. The labelling of the orbits is: $\Omega[N, n_z, \Lambda]$ with N being the principal quantum number of the major oscillator shell, n_z the number of quanta associated with the wave function moving along the z -direction and Λ the projection of the orbital angular momentum onto the z axis. For example the $2g_{9/2}$ orbit splits into five two-fold degenerate components, where the first two orbits are strongly down-sloping for prolate ($\epsilon_2 > 0$) and oblate ($\epsilon_2 < 0$) deformation. The upper two orbits at the prolate side strongly favor sphericity, since the energy increases strongly. At the oblate side, the upper two orbits are rather insensitive to deformation.

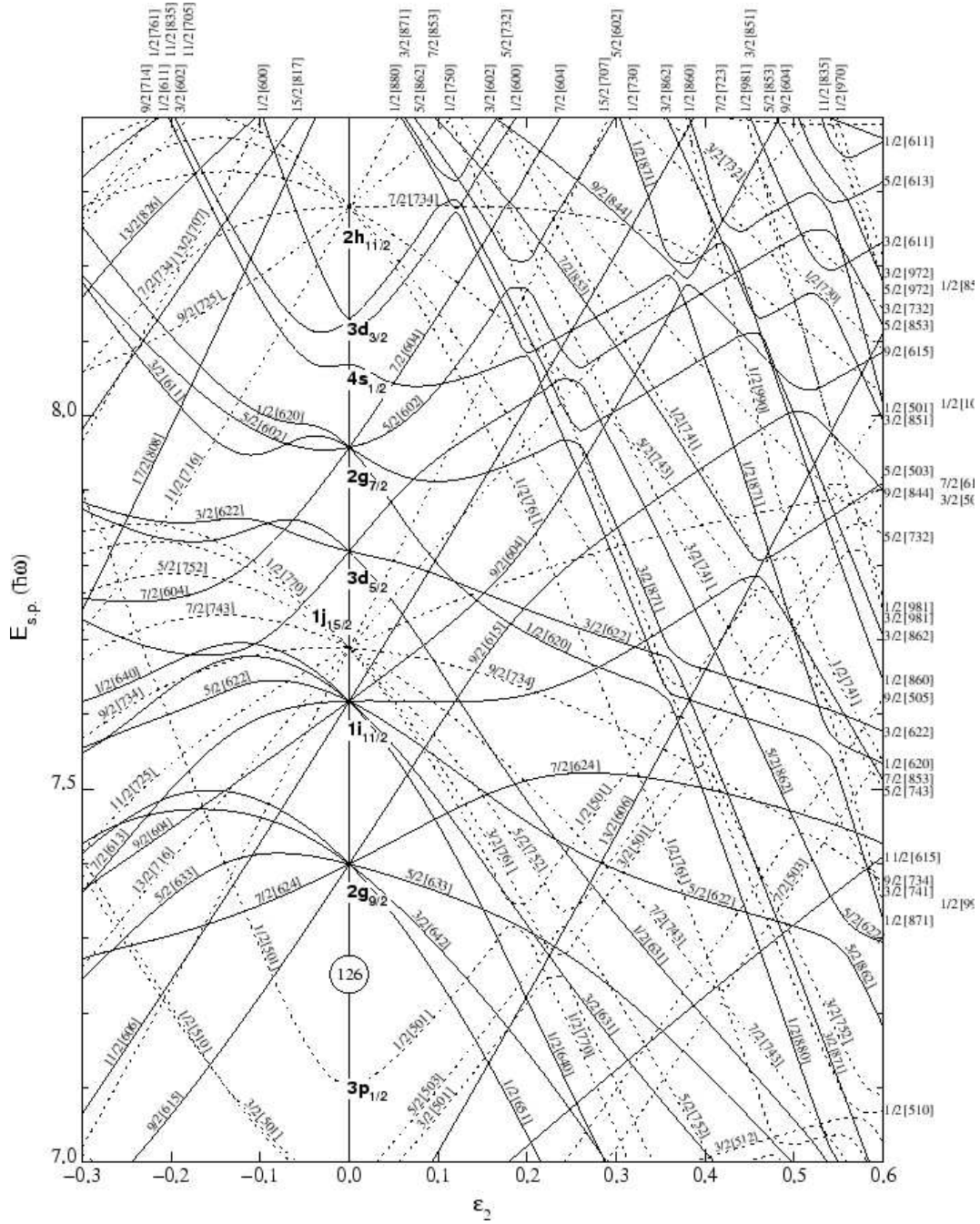


Figure 2.2: Evolution of the single-particle energies as a function of the nuclear deformation parameter $\epsilon_2 = 1.05 \beta_2$ in the Nilsson model for neutron numbers $N \geq 126$ [FIR96].

2.2.1 Woods-Saxon potential

As described above a more realistic description of the single-particle levels is given by the choice of a finite depth potential, such as the Woods-Saxon potential, instead of the oscillator potential both for spherical and deformed nuclei. Here the potential well has a similar shape as the density of nucleons, which is given for the spherical case by

$$\rho(r) = \frac{\rho_0}{1 + \exp\left[\frac{r-R}{a}\right]}, \quad (2.13)$$

where r is the distance of the nucleons with respect to the centre of the nucleus, ρ_0 is a constant, R is the radius of the nucleus and a is the surface thickness. The spherical Woods-Saxon potential is therefore taken as

$$V(r) = -\frac{V_0}{1 + \exp\left[\frac{r-R_v}{a_v}\right]} \quad (2.14)$$

Typical values for the parameters are: depth $V_0 \approx 50$ MeV, radius $R_v \sim 1.1A^{1/3}$ fm, and surface thickness $a_v \sim 0.5$ fm [GRE96, RIN80]. We generalise the spherical Woods-Saxon potential to deformed nuclei by

$$V(r) = -\frac{V_0}{1 + \exp\left[\frac{r-R_v(r;\beta_2)}{a_v}\right]} \quad (2.15)$$

where $(r;\beta_2)$ denotes a set of all the shape parameters uniquely specifying the nuclear surface shape [NAZ85]. In the full Hamiltonian, a spin-orbit term must be added to the Woods-Saxon potential in equation in order to reproduce the correct magic numbers. This is given by

$$V_{so}(r;\beta_2) = -\lambda \left(\frac{\hbar}{2mc}\right)^2 [\nabla V(r;\beta_2)_{so} \times p] \cdot s. \quad (2.16)$$

This is the basis of the theoretical investigation of ^{237}Pu as performed by Hamamoto and Ogle [HAM75]. The results from this theoretical investigation are compared to our experimental findings and discussed in chap. 6.3.1.

2.3 Relativistic Mean Field

In recent years the relativistic description of nuclear systems has been investigated extensively. It is formulated as an effective field theory (EFT). This means that it is not a fundamental field theory (like QED or QCD), but a field theoretical formulation of composite objects (hadrons) with effective adjustable parameters [SER86].

The attractiveness of this approach is that many phenomena in nuclear physics can be understood in a more "natural", i.e. elegant, way, like the saturation mechanisms of nuclear

matter, the strong spin-orbit force, the pseudo-spin symmetry or the energy dependence of the optical potential. Some of these questions will be discussed below. Today the application of a relativistic description to nuclear matter and to ground and excited states of nuclei has reached a similar precision as that of non-relativistic approaches [VRE05].

The effective field theory is formulated with nucleons and mesons as effective degrees of freedom, and is often called Quantumhadrodynamics (QHD). It is formulated with a Lagrangian density with minimal coupling (i.e. linear point coupling) of the mesons and baryons [SER86]. Such an approach is justified by the phenomenological success of the one-boson-exchange potential (OBEP) in the description of the NN interaction, which can be derived in the static limit from such a theory.

We construct a Lagrangian, choosing the simplest theoretical model, the $\sigma\omega$ model as [SER86]:

$$\mathcal{L}^{(\sigma\omega)} = \mathcal{L}^{(ferm)} + \mathcal{L}_0^{(mes)} \quad (2.17)$$

where

$$\mathcal{L}^{(ferm)} = \bar{\psi}(i\gamma^\mu D_\mu - m^*)\psi = \mathcal{L}_0^{(ferm)} + \mathcal{L}_{int} \quad (2.18)$$

where the covariant derivative $D_\mu = \partial_\mu + ig_v V_\mu$ includes coupling to the vector field and, the effective mass $m^* = m - g_s\phi$ includes the coupling to the scalar field. $\mathcal{L}_0^{(ferm)}$ is the free Dirac Lagrangian and thus

$$\mathcal{L}_{int} = -g_v\bar{\psi}\gamma^\mu\psi V_\mu + g_s\bar{\psi}\psi\phi, \quad (2.19)$$

where the vector current is $j^\mu = \bar{\psi}\gamma^\mu\psi$ and $\rho_s = \bar{\psi}\psi$ is the scalar density. The meson Lagrangian is

$$\mathcal{L}^{(mes)} = \frac{1}{2}(\partial_\mu\phi\partial^\mu\phi - m_s^2\phi^2) - \frac{1}{4}F^{\mu\nu}F_{\mu\nu} + \frac{m_v^2}{2}V_\mu V^\mu \quad (2.20)$$

with the field tensor $F^{\mu\nu} = \partial^\mu V^\nu - \partial^\nu V^\mu$. As the meson fields have a mass this cannot be a gauge theory, but it is rather an EFT. The equations for the fields are obtained from the Euler-Lagrange variational equations. For the Fermion field this is the Dirac equation interacting with scalar and vector fields:

$$\gamma^\mu(i\partial_\mu - g_v V_\mu)\psi - (m - g_s\phi)\psi = 0 \quad (2.21)$$

The equations for the σ and ω mesons are

$$(\partial_\mu\partial^\mu + m_s^2)\phi = g_s\bar{\psi}\psi \quad (2.22)$$

$$\partial_\mu F^{\mu\nu} + m_v^2 V^\nu = g_v\bar{\psi}\gamma^\nu\psi, \quad (2.23)$$

i.e. a Klein-Gordon equation for the σ -meson with a source proportional to the scalar density and a Proca equation for the ω -meson with a vector source. From invariance with respect to a global phase transformation of $\psi \rightarrow e^{i\alpha}\psi$, the conservation of the vector current is obtained $\partial_\mu J^\mu = 0$. The baryon conservation number is:

$$B = \int d^3x j^0 = \int d^3x \psi^\dagger\psi = const \quad (2.24)$$

The full equations of motion for the quantum fields are only solvable numerically. The simplest approximation is the semiclassical approximation (relativistic mean field approximation; RMF). It is equivalent to a relativistic Hartree approximation. For not too small densities the boson field can be approximated by classical fields as:

$$\begin{aligned}\hat{\phi} &\rightarrow \langle \hat{\phi} \rangle \equiv \phi(x) \\ \hat{V}_\mu &\rightarrow \langle \hat{V}_\mu \rangle = V_\mu(x).\end{aligned}$$

However, fermions (nucleons) are treated quantally i.e. they cannot be approximated by classical fields at low temperatures. In this approximation the Dirac equation (2.21) describes the motion of a nucleon in scalar $S(x)$ and a vector $V_\mu(x)$ fields which are determined by the scalar and vector nucleon density. These can be solved easily for nuclear matter (construct S , V) and for spherical nuclei (see below).

The simplest $\sigma\omega$ -model represents the essential features of nuclear systems, e.g. leading to attractive (σ -meson) and repulsive (ω -meson) forces and thus to saturation. On a quantitative level, however, it is not satisfactory. Various extensions have been considered. A first step is to include the isovector mesons.

$$\begin{aligned}\rho - \text{meson}, J^\pi &= 1^-, T = 1, m_\rho \sim 770 \text{ MeV}, (\rho^0, \rho^\pm) \\ \delta - \text{meson}, J^\pi &= 0^+, T = 1, m_\delta \sim 980 \text{ MeV}, (\text{also known as } a_0)\end{aligned}\tag{2.25}$$

which are necessary to describe the proton neutron difference in strong interactions (together with the photon field, for the electromagnetic interaction).

A possible approach of including pion-fields is to apply the $SU(2)_{\text{isospin}}$ gauge theory to strong isospin [WOL08]:

$$D_\mu = \partial_\mu + \frac{i}{2}g_\pi\gamma_\mu\gamma_5\vec{\tau}\cdot\vec{\pi}\tag{2.26}$$

where $\vec{\pi}$ is the pseudovector pion field. Then the interaction Lagrangian of the nucleon-pion system is:

$$\mathcal{L}_{\pi N} = -\frac{g_\pi}{2}\bar{\psi}\gamma_5\vec{\tau}\psi\vec{\pi}\tag{2.27}$$

which is called a pseudoscalar coupling. However, usually a pseudovector coupling $\mathcal{L}_{\pi N}^{pv} = -\frac{g_\pi}{2}(\bar{\psi}\gamma_5\gamma^\mu\partial_\mu\psi)\vec{\tau}\cdot\vec{\pi}$ is preferred, because it describes better πN -scattering. π -mesons are usually not considered in most RMF-calculations. It is found that this contribution is small (it vanishes for spin-isospin saturated systems).

An extension that has been used extensively are non-linear models with self-interaction of the σ -meson fields.

$$\mathcal{L}^{NL} = \frac{1}{2}(\partial_\mu\phi\partial^\mu\phi - m_s^2\phi^2) - \frac{b_3}{2}\phi^3 - \frac{b_4}{4}\phi^4\tag{2.28}$$

This can be used to improve the compressibility of nuclear matter. Other approaches employ instead density dependent couplings of the $\sigma\omega$ field to the nucleon:

$$\mathcal{L}^{DD} = \bar{\psi}[i\gamma^\mu(\partial_\mu + ig_\omega V_\mu) - (m - g_\sigma\phi)]\psi + \mathcal{L}_0^{(mes)}\tag{2.29}$$

where $g_\omega = \Gamma_\omega(\hat{\rho})$ and $g_\sigma = \Gamma_\sigma(\rho)$ are functionals of a scalar operator dependent on the density.

The simplest system to solve is nuclear matter, which is defined as a homogenous, isotropic and stationary system of strongly interacting hadronic matter at a given density ρ_B (baryonic density), temperature T (here $T=0$), asymmetry ($\delta = \frac{N-Z}{N+Z}$, at first we assume $\delta = 0$). For simplicity we consider only σ and ω -meson fields. Then the meson fields

$$\begin{aligned}\phi(\vec{x}, t) &\rightarrow \phi_0 \\ V_\mu(\vec{x}, t) &\rightarrow \delta_{\mu 0} V_0\end{aligned}$$

are constant in space-time and the vector field has no space-direction but only a time-like component. The field equations for the σ , ω mesons, simplify as:

$$\phi_0 = \frac{g_\sigma}{m_0^2} \rho_s, \quad (2.30)$$

i.e. the σ -field is given by the scalar density, and

$$V_0 = \frac{g_\omega}{m_\omega^2} \rho_B \quad (2.31)$$

the ω -field, is given by ρ_B an external parameter. For the nucleon field ψ we obtain:

$$[i\gamma^0 \partial_t - g_\omega V_0 + i\vec{\gamma} \vec{\nabla} - m^*] \psi = 0 \quad (2.32)$$

where $m^* = m - g_0 \phi_0$ is the (Dirac) effective mass. This is like a free Dirac equation with constant shifts in mass and energy. From the known solutions the energy density, or the energy particle, can be calculated. It is seen to depend only on two quantities, which are fitted to the saturation point of nuclear matter: $C_s^2 = g_s^2 \frac{m^2}{m_s^2} = 265$, $C_v^2 - \delta_v^2 \frac{m^2}{m_v^2} = 196$. The results for symmetric nuclear matter (4-fold degeneracy of levels) and pure nuclear matter (2-fold degeneracy) is shown in Fig. 2.3. One finds a qualitatively reasonable behaviour for nuclear matter (saturation) and unbound neutron matter. However, quantitatively the effective mass $m^*/m \sim 0.16$ is too low and the incompressibility $K_V \sim \frac{\partial^2 E}{\partial \rho^2} \sim 500$ MeV is too high. To improve this behaviour, extended models as discussed above are used (non-linear and density dependent models) [WAL95].

By taking the square of equation (2.32) and rewriting, one obtains a Schrödinger-like equation for the upper component wave function

$$\left(\frac{-\hbar \Delta}{2m} + U_{seq} - \epsilon^{nr} \right) \psi = 0 \quad (2.33)$$

with the Schrödinger-equivalent potential

$$U_{seq} = (V - S) + \frac{1}{2m}(S^2 - V^2) + \frac{V}{m} \epsilon^{nr} \quad (2.34)$$

where $S = g_s \phi_0$, $V = g_\omega V_0$ and $\epsilon^{nr} = E - mc^2$. It is found that the leading part of the potential is the difference of vector and scalar fields. The fields in calculations are typically found to be of the order of several hundred MeV ($S \sim 450$ MeV, $V \sim 400$ MeV). The weak central potential is then a cancellation effect. It is seen below for finite nuclei, that this cancellation is not true for the spin-orbit term and accounts for the strong spin-orbit coupling. The last term shows that

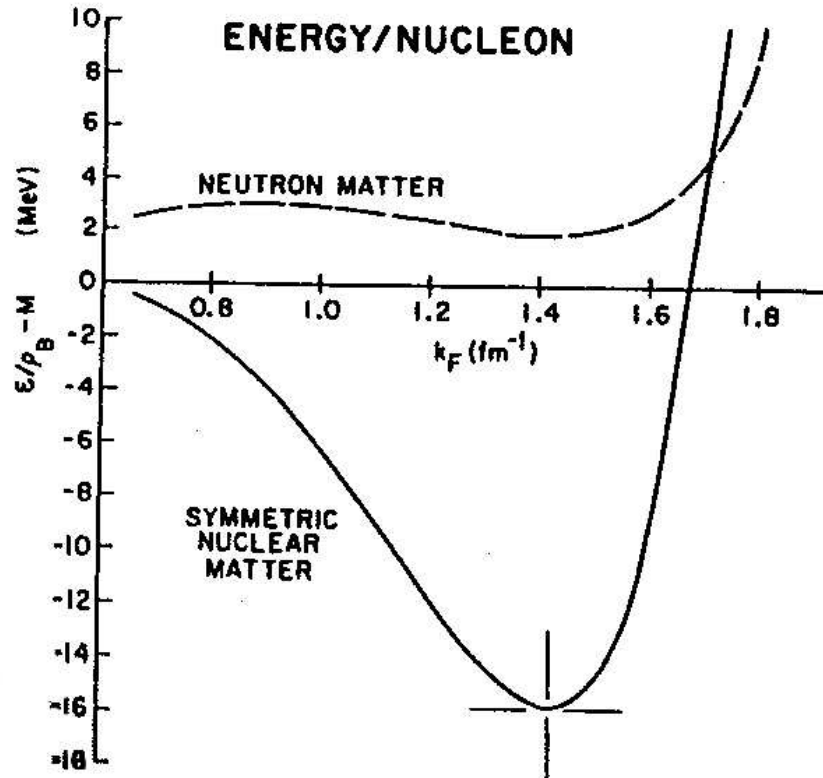


Figure 2.3: Binding energy per nucleon vs. Fermi wave number for nuclear matter computed from the linearised theory. The coupling constant C_s^2 and C_v^2 have been chosen to reproduce the binding energy and density of nuclear matter (degeneracy $\gamma = 4$, $\epsilon/\rho_B - m_b c^2 = -15.75 \text{ MeV}$, $k_F = 1.42 \text{ fm}^{-1}$) [FET71]. The prediction of the linearised theory for pure neutron matter, obtained by simply setting $\gamma = 2$, are also shown in this figure, taken from [WAL74].

the potential is typically energy dependent as a relativistic effect. This is also known empirically for the real part of the optical potential.

We now consider calculations for finite nuclei. In the following spherical symmetry will be assumed. In this case, single-particle levels are characterised by the principal quantum number $n = 1, 2, \dots$, the orbital angular momentum $l = 0, 1, \dots$, the parity $\pi = (-1)^l$, the total angular momentum $j = \pm 1/2$, and its projection $\Omega = -j, -j + 1, \dots, j - 1, j$. In the relativistic description it is convenient to combine the quantum numbers l and j by introducing the quantity $\kappa = \pm 1, \pm 2, \pm 3, \dots$ where $j(\kappa) = |\kappa| - 1/2$ and

$$l(\kappa) = \begin{cases} \kappa - 1 & \text{if } \kappa > 0 \\ -\kappa & \text{if } \kappa < 0 \end{cases} \quad (2.35)$$

A single-particle state $\psi_{n\kappa\Omega}$ with energy $E_{n\kappa}$ (including the rest mass m) of a nucleon is obtained by solving the time-independent Dirac equation;

$$\mathcal{H}\psi_{n\kappa\Omega} = E_{n\kappa}\psi_{n\kappa\Omega} \quad (2.36)$$

where

$$\mathcal{H} = \vec{\alpha} \cdot \vec{p} + V(r) + \beta[m - S(r)] \quad (2.37)$$

is the relativistic Hamiltonian with Dirac matrices $\vec{\alpha}$ and β momentum operator \vec{p} in standard notation [TYP08]. The system of units is chosen such that $\hbar = c = 1$. The scalar and vector potentials are denoted by $S(r)$ and $V(r)$. Here, the sign convention with a positive scalar field S is used. For spherical symmetry it is customary to write the Dirac spinor as:

$$\psi_{n\kappa\Omega} = \frac{1}{r} \begin{pmatrix} F_{n\kappa}(r)\mathcal{Y}_{\kappa\Omega}(\hat{r}) \\ iG_{n\kappa}(r)\mathcal{Y}_{-\kappa\Omega}(\hat{r}) \end{pmatrix} \quad (2.38)$$

with radial wave functions $F_{n\kappa}(r) = F_{nlj}(r)$ and $G_{n\kappa}(r) = G_{nlj}(r)$ in the upper and lower components, respectively, that are normalised to

$$\int_0^\infty dr [|F_{n\kappa}(r)|^2 + |G_{n\kappa}(r)|^2] = 1. \quad (2.39)$$

The spin and angular dependence is contained in the spinor spherical harmonics

$$\mathcal{Y}_{\kappa\Omega}(\hat{r}) = \sum_{m_l m_s} \langle l m_l s m_s | j \Omega \rangle Y_{lm_l}(\hat{r}) \chi_{sm_s} \quad (2.40)$$

where the orbital angular momentum $l(\kappa)$ of the spherical harmonic Y_{lm_l} is coupled with the nucleon spin $s = 1/2$ of the spinor χ_{sm_s} to the total angular momentum $j(\kappa)$. The upper and

lower component in equation 2.38 have an opposite sign for the quantum number κ in the spinor spherical harmonics and consequently opposite parity with a difference of one in the orbital angular momentum. By applying equation 2.37 to the Dirac spinor in equation 2.38 a set of coupled first-order differential equations is obtained. Which can be decoupled leading to the independent wave equations:

$$H_F(\kappa)F_{n\kappa} = E_{n\kappa}F_{n\kappa} \quad (2.41)$$

$$H_G(\kappa)G_{n\kappa} = E_{n\kappa}G_{n\kappa} \quad (2.42)$$

with Schrödinger-like Hamiltonians

$$H_F(\kappa) = \frac{1}{A} \left[-\frac{d^2}{dr^2} + \frac{\kappa(\kappa-1)}{r^2} + \frac{A'}{A} \left(\frac{d}{dr} - \frac{\kappa}{r} \right) \right] + V - S + m \quad (2.43)$$

and

$$H_G(\kappa) = \frac{1}{A} \left[-\frac{d^2}{dr^2} + \frac{\kappa(\kappa+1)}{r^2} + \frac{B'}{B} \left(\frac{d}{dr} + \frac{\kappa}{r} \right) \right] + V - S + m \quad (2.44)$$

A' denotes the derivative with respect to the radius r . The quantities

$$A(r) = E_{n\kappa} - V(r) + m - S(r) \equiv 2m_{eff} \quad (2.45)$$

$$B(r) = E_{n\kappa} - V(r) - m + S(r) \quad (2.46)$$

depend on the single-particle energy $E_{n\kappa} = E_{nlj}$, appearing as the eigenvalue in equations (2.41) and (2.42). $A(r)$ can be considered as twice the position depending effective nucleon mass m_{eff} . It is always positive in standard RMF models. For vanishing scalar and vector fields $S(r)$ and $V(r)$ at large radii r , $B(r)$ reduces to the non-relativistic energy $\epsilon_{n\kappa} = E_{n\kappa} - m < 0$ of the bound nucleon. The Hamiltonians $H_F(\kappa)$ and $H_G(\kappa)$ have the same spectrum, even though the potentials have a different form. The Hamiltonian of equation (2.41) for the upper component wave function $F_{n\kappa}(r)$ can be rewritten in a non-relativistic form:

$$H_F(\kappa) = -\frac{d}{dr} \frac{1}{2m_{eff}} \frac{d}{dr} + \frac{l(l+1)}{2m_{eff}r^2} + V_c(r) + V_{so}(r) \langle \vec{l} \cdot \vec{s} \rangle + m \quad (2.47)$$

with central and spin-orbit potentials

$$\begin{aligned} V_c(r) &= V - S + \frac{1}{Ar} \left(-\frac{A'}{A} \right) \\ &= V - S - \frac{1}{2} V_{so}(r) \end{aligned} \quad (2.48)$$

taking equation (2.45) into account, we find that

$$V_{so} = \frac{2}{Ar} \left(-\frac{A'}{A} \right) = \frac{1}{2m_{eff}^2 r} \frac{d}{dr} (V + S) \quad (2.49)$$

and with $\kappa(\kappa-1) = l(l+1)$ and $\kappa-1 = 2 \langle \vec{l} \cdot \vec{s} \rangle$. The spin-orbit potential contains contributions from the derivative of the sum $V + S$ whereas the main contribution to the

central potential arises from the difference $V - S$. These equations (2.48, 2.49) are an extension of equation (2.34) for nuclear matter and are very interesting to understand the nuclear shell model. With this typically the magnitude of the scalar and vector fields are found to be of the order of several hundred MeV ($S \approx 450$ MeV, $V \approx 400$ MeV). Then the central potential is relatively weak, because the two fields essentially cancel each other. On the other hand in the spin-orbit term the two fields add to each other and lead to a strong spin-orbit force. This then is a elegant explanation of the above mentioned puzzle of the abnormal strength of the spin-orbit interaction in the shell model [TYP08, WOL08].

Self-consistent mean-field models based on the relativistic mean-field theory (RMF) [SER86, SER97] have been very successfully employed in analyses of a variety of nuclear structure phenomena, not only in nuclei along the valley of β stability, but also in exotic nuclei with extreme isospin values and close to the particle drip-lines. RMF-based models have reached a level of sophistication and accuracy comparable to the non-relativistic Hartree-Fock-models based on Skyrme and Gogny effective interactions [VRE05]. For nuclei with unfilled shells we find that additional correlations are required to describe the properties of e.g. deformation and pairing.

2.4 Relativistic Hartree - Fock Bogoliubov calculations

In addition to the self-consistent mean-field single-nucleon potential, the inclusion of pairing correlations is essential for a quantitative description of structure phenomena in open-shell spherical and deformed nuclei.

The Hartree-Fock-Bogoliubov (HFB) theory [BEN03, KUC91, MAN75, PAA07, RIN80] provides a unified description of ph - and pp -correlations in nuclei and, when the self-consistent HFB equations are formulated in coordinate space, allows also for a treatment of continuum effects in the presence of pairing. In the relativistic version most applications have used the finite-range meson-exchange representation of the RMF theory, in which the nucleus is described as a system of Dirac nucleons coupled to effective mesons and the electromagnetic field (such as the: σ , ρ , π and ω meson). A medium dependence of the effective interaction can be introduced either by including non-linear meson self-interaction terms in the Lagrangian, or by assuming an explicit density dependence for the meson nucleon couplings [VRE05]. The HFB-wavefunction $|HFB\rangle = |\Phi\rangle$ is defined as the quasi-particle vacuum of the quasiparticles:

$$\alpha_k^+ = \sum_n U_{nk} c_n^+ + V_{nk} c_n \quad (2.50)$$

where $\alpha|\Phi\rangle = 0$. One has two densities, the normal density:

$$\rho_{nn'} = \langle \Phi | c_{n'}^+ c_n | \Phi \rangle = \sum_k V_{nk}^* V_{n'k} \quad (2.51)$$

and the pairing tensor:

$$\kappa_{nn'} = \langle \Phi | c_n c_{n'} | \Phi \rangle = \sum_k V_{nk}^* U_{n'k}. \quad (2.52)$$

The density functional depends on the two densities:

$$E = E[\rho, \kappa] \quad (2.53)$$

The variation of $E'[\rho, \kappa] = E[\rho, \kappa] - \lambda Tr(\rho)$ (with a constant to conserve particle number on the average) with respect to ρ and κ yields two coupled equations for the HFB wave functions $U_k(r)$ and $V_k(r)$,

$$\begin{pmatrix} \hat{h} - \hat{\Delta}^* \\ \hat{\Delta} - \hat{h}^* \end{pmatrix} \begin{pmatrix} U_k(r) \\ V_k(r) \end{pmatrix} = \begin{pmatrix} U_k(r) \\ V_k(r) \end{pmatrix} E_k \quad (2.54)$$

with two potentials, the normal mean field

$$\hat{h} = \frac{\delta E'}{\delta \rho'} \quad (2.55)$$

and the pairing field

$$\hat{\Delta} = \frac{\delta E}{\delta \kappa'} \quad (2.56)$$

We no longer have a sharp Fermi surface ($\rho^2 = \rho$) but there is still a constraint: $\hat{\rho}^2 - \hat{\rho} = \hat{\kappa}\hat{\kappa}^*$, which means, that we have independent quasi-particles with the occupation numbers 0 or 1.

Extending this to the relativistic Hartree-Fock-Bogoliubov equations [SER01, VRE05, RIN80], also known as the Dirac-Hartree-Fock-Bogoliubov equations, defined as:

$$\begin{pmatrix} \hat{h}_D - m - \lambda & \hat{\Delta} \\ -\hat{\Delta}^* & -\hat{h}_D + m + \lambda \end{pmatrix} \begin{pmatrix} U_k(r) \\ V_k(r) \end{pmatrix} = E_k \begin{pmatrix} U_k(r) \\ V_k(r) \end{pmatrix} \quad (2.57)$$

where \hat{h}_D is the Dirac Hamiltonian, λ is the chemical potential, $\hat{\Delta}$ is the pairing field, E_k is the quasi-particle energy and $V_k(r)$ is the quasiparticle wave function. These equations can be applied for a fully self-consistent description of open-shell nuclei, where the possibly deformed mean fields and the pairing field are determined simultaneously. They also describe the ground-state properties of weakly bound nuclei far from stability. These calculations were performed by Ring and Daoutidis [DAO07] for ^{237}Pu , the results of these calculations are compared to the experimental findings of this thesis in chapter 6.3.3.

Chapter 3

Planning of the Experiment and Experimental Set up

Measuring a rare decay process such as isomeric fission requires a highly efficient experimental set up optimised in all components to the specific characteristics of the reaction under study. Therefore, when planning such an ambitious experiment, the first step has to be a review of the previously published nuclear structure information on $^{237\text{f}}\text{Pu}$.

In fact only very little unambiguous information was published when starting this thesis project. Basically the existence of two fission isomers was confirmed, the shape isomeric ground state with a half-life of 110 ns [RUS71] and a higher-lying long-lived isomer with $t_{1/2} = 1180$ ns [VAN73]. The excitation energy of the long-lived isomer was rather vaguely reported as being 300 ± 150 keV [VAN73] above the isomeric ground state, and for the spins of the two isomers only tentative values of $\frac{5}{2}$ and $\frac{11}{2}$ were derived for the short- and long-lived isomers, respectively [GUEN79].

Figure 3.1 shows a schematic view of the nuclear structure in the second potential well of $^{237\text{f}}\text{Pu}$, as it was known at the beginning of this present work. Indicated in red are the two known fission isomers with their respective half-lives of $t_{1/2} = 110$ ns and $t_{1/2} = 1180$ ns [RUS71, VAN73, SPE74]. On top of the two fission isomers rotational bands have been added. For the isomeric ground state a spin of $I = \frac{5}{2}$ was assumed, supported both by the ground state band in the neighbouring shape isomer $^{239\text{f}}\text{Pu}$ [BAC79] and by the g-factor measurement in the low spin isomer ($g = -0.45(3)$) performed by M.H. Rafailovich et al. [RAF82]. For the energetic position of the rotational band members a typical superdeformed rotational parameter $\frac{\hbar^2}{2\theta} \approx 3.4$ keV was assumed [THI02]. The spin assignments of $I = 5/2$ and $11/2$ for the two shape isomers have to be treated tentatively, it will be one of the goals of the present work to consolidate these assignments. In addition to the rotational bands expected on top of the two isomeric levels, β vibrational states have been included in Fig. 3.1, separated from their respective isomeric ground state by a typical β -vibrational phonon energy in the second minimum of actinides of $\hbar\omega_\beta \approx 600$ keV [THI03]. Whilst the rotational band structure has been subject of the present work, the measurement of E0 transitions aiming at the identification of the collective

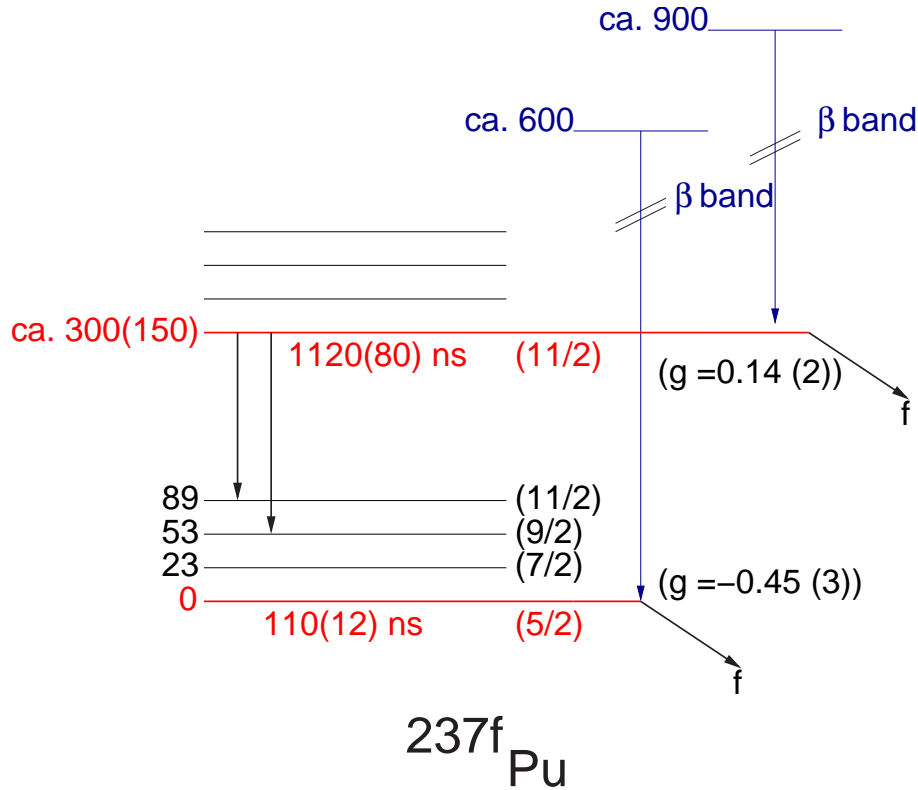


Figure 3.1: Expected nuclear structure in the second minimum of ^{237}Pu based on the two known fission isomers. Known properties such as isomeric half-lives [VAN73, RUS71, RAF83], spin assignment [GUEN79] and g-factors [RAF82] are indicated, while in addition the expected structure of rotational and β vibrational bands (assuming a typical superdeformed rotational parameter $\frac{\hbar^2}{2\theta} = 3.4$ keV and a β phonon energy of 600 keV) has been included.

β -vibrational excitations will be left to future experiments.

3.1 Isomeric yield considerations for ^{237}Pu

Based on the properties of the 3.8 ns shape isomer in the prototype nucleus ^{240}Pu with its deformed magic neutron number $N = 146$ [PAN00, GAS02], a comparison for the reaction-specific properties in ^{237}Pu is listed in Table 3.1. Following a nuclear reaction, in which an actinide compound nucleus is produced with an excitation energy above the fission barrier, the probabilities for prompt fission, population of the first minimum and population of the second minimum are approximately 0.9, 0.1 and 10^{-5} , respectively. Consequently studies of shape isomers have to be performed in competition with (prompt) fission products being about 10^5 more abundant than the desired reaction. In the case of ^{240}Pu and ^{237}Pu this is expressed by the isomer-to-prompt population ratio, which is $8.4 \cdot 10^{-5}$ for ^{240}Pu [PAN00] and $1.34 \cdot 10^{-5}$ for ^{237}Pu [VAN73], respectively. For the production of both isomers in ^{240}Pu and ^{237}Pu , the $(\alpha, 2n)$ reaction provides a maximum isomeric yield at 24 MeV beam energy, based on the excitation functions measured by R. Vandenbosch et al. [VAN73] (see Figure 3.2). For the 3.8 ns isomer in the even-even

	$^{240\text{f}}\text{Pu}$	$^{237\text{f}}\text{Pu}$
reaction	$^{238}\text{U}(\alpha, 2\text{n})^{240\text{f}}\text{Pu}$	$^{235}\text{U}(\alpha, 2\text{n})^{237\text{f}}\text{Pu}$
E_α [MeV]	24	24
I_α [nA]	2	2
target thickness	$\sim 1.5 \text{ mg/cm}^2$	$\sim 3.8 \text{ mg/cm}^2$
N_{del}^{fiss}	70/hour	50/hour
$(d\Omega/4\pi)_\gamma$ [%]	14	9
$\frac{\sigma_{isomer}}{\sigma_{prompt}}$	$8.4 \cdot 10^{-5}$	$1.34 \cdot 10^{-5}$
σ_{del}	$10 \mu\text{b}$	$1.86(15) \mu\text{b}$

Table 3.1. Comparison of experimental parameters for the reactions populating the fission isomers in $^{240\text{f}}\text{Pu}$ ([PAN00, GAS01]) and $^{237\text{f}}\text{Pu}$ (this work), respectively.

nucleus $^{240\text{f}}\text{Pu}$ a population cross section of $10 \mu\text{b}$ has been measured [PAN00]. This is about a factor 5 larger than expected for the odd-N shape isomers of $^{237\text{f}}\text{Pu}$. In a preparatory experiment, employing the recoil shadow method, the value of $\sigma_{del} = 1.86(15) \mu\text{b}$ was determined in the framework of this thesis [MOR03].

In order to avoid further background from target impurities or backing materials, thick metallic Uranium targets have been used in both cases. Furthermore, as the compound nuclei produced via the $(\alpha, 2\text{n})$ reaction are stopped in the target, no Doppler-shift correction is required for the measured γ -ray energies. However, as a metallic Uranium target is highly oxidising, the production and handling of the targets is extremely difficult, as any contact to oxygen has to be avoided, thus requiring a dry Argon atmosphere during the target production as well as during the transport from the hot lab in Munich to the IKP in Cologne and during the mounting into the MINIBALL target chamber.

In the spectroscopy of $^{240\text{f}}\text{Pu}$ performed by Pansegrau et al. [PAN00] a ^{238}U target with a thickness of $\sim 1.5 \text{ mg/cm}^2$ was used. In those experiments the angular-dependent flight time distribution of the fission fragments from the target to the detector varied by approximately 10 ns. Compared to the isomeric half-life of 3.8 ns, during the first 3 half-lives of $^{240\text{f}}\text{Pu}$ fission fragments from delayed fission could not be separated from the abundant background of prompt fission events. Therefore only $\approx 18\%$ of the isomeric fission events in $^{240\text{f}}\text{Pu}$ could be analysed. As the half-lives in $^{237\text{f}}\text{Pu}$ are much larger ($t_{1/2} = 110 \text{ ns}$ and $t_{1/2} = 1180 \text{ ns}$), nearly all of the isomeric events can unambiguously be separated from prompt background, thus allowing to study $^{237\text{f}}\text{Pu}$ even in view of the rather small isomeric population cross section ($\approx 2 \mu\text{b}$ for $^{237\text{f}}\text{Pu}$ compared to $10 \mu\text{b}$ in $^{240\text{f}}\text{Pu}$)

3.2 Experimental set up

Excited states within the second potential minimum deexcite into their respective isomeric ground state either via γ -ray emission or by emission of conversion electrons. Subsequently the shape isomeric ground state decays via fission with a half-life of 110 ns and 1180 ns, respectively,

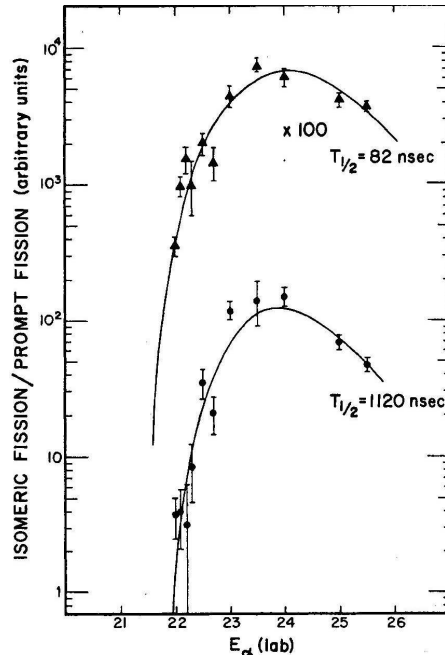


Figure 3.2: Excitation functions for the isomeric-to-prompt-fission yield ratios in ^{237}fPu [VAN73]. The ratios of the two isomers are given in arbitrary units, where the short-lived ratio has been multiplied by a factor of 10^9 , and the long-lived component has to be multiplied by a factor of 10^7 to give peak ratios consistent with measured absolute values [RUS71, BRI71].

in the case of ^{237}Pu . In view of the small population cross section an efficient trigger is required for both the fission fragments and the γ rays with a maximum solid angle coverage. The γ -rays were detected using the MINIBALL spectrometer described in chapter 3.2.1, while the corresponding fission fragments were detected in a 4π -array of parallel plate avalanche counters (PPACs) described in chapter 3.2.2. The schematics of the experimental set up is shown in Fig. 3.3. A compact 4π PPAC array encloses the target, whilst being surrounded by the germanium γ -ray detectors of the MINIBALL spectrometer [EBE01].

3.2.1 MINIBALL Detector

The γ rays emitted in the experiment were detected using the MINIBALL spectrometer [WEI03] (see Figure 3.4). The MINIBALL detector array is a high-resolution γ -ray spectrometer, which was developed and built for the investigation of reactions with low γ -ray multiplicities and optimised for large photopeak efficiency by optimum solid angle coverage with Ge crystals without anti-Compton shielding. The MINIBALL array consists of eight sixfold segmented triple Ge cryostats, in our case arranged around the target chamber with a distance to the target of ~ 10 cm. Four detectors are arranged at 45° degrees and four at 135° with respect to the beam axis.

The MINIBALL detectors have an average relative efficiency of 55%. Grouping the 24 Ge crystals in a compact geometrical arrangement $\approx 17\%$ solid angle coverage could be achieved

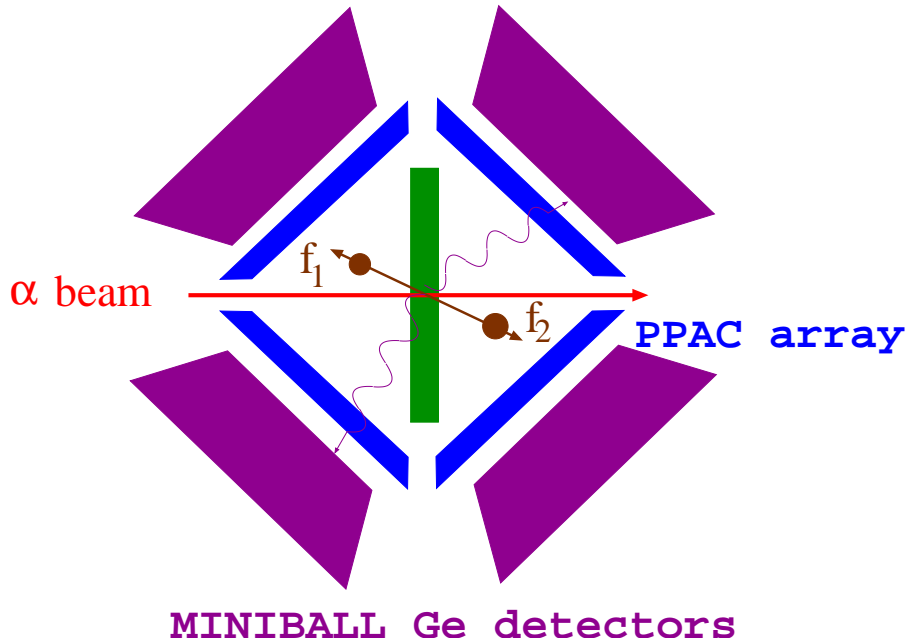


Figure 3.3: Schematic view of the experimental set up used in the high resolution γ -spectroscopy experiment of ^{237}Pu : the ^{235}U target is surrounded by a 4π array of 8 trapezoidal PPAC modules and 8 MINIBALL triple-cluster cryostats, each containing three sixfold segmented germanium crystals.

with our setup, leading to a photopeak efficiency of approximately 9% at 1.3 MeV. Using a thick metallic target, the resulting compound nuclei are stopped in less than 0.1 ps and γ rays are therefore emitted at rest in the centre of the spectrometer, thereby avoiding the need for a Doppler correction. Each Ge detector module can process a count rate of up to 20 kHz, before pile-up will deteriorate the energy measurement, as the signal fall-time of the preamplified signal is $50 \pm 5 \mu\text{s}$.

3.2.2 Parallel Plate Avalanche Counter (PPAC) array

A Parallel Plate Avalanche Counter (PPAC) is a versatile, cheap, easy-to-build and handle gas detector for ionising particles. If ionising particles enter the gas-filled detector volume, along their trajectory electron-ion pairs are produced. If the gas pressure and the electric field between the plates are sufficient, the electrons are accelerated to the anode creating an avalanche of secondary electrons, whose collective charge is then detected and measured at the anode. Simultaneously the mirror charges induce a signal at the cathode. The fall time of the anode signal (~ 5 ns) is governed by the slow drift velocity of the ions and limits the acceptable count rate in the PPAC module with deterioration by pile up. Due to the very short signal rise times, PPACs have a very good time resolution (< 0.5 ns). By segmenting one of the two electrodes (in our case the anode back plate of the detector module) a position sensitive detection is possible (see Figure 3.5).

In order to achieve an efficient detection of fission fragments, a compact array of 8 trapezoidal

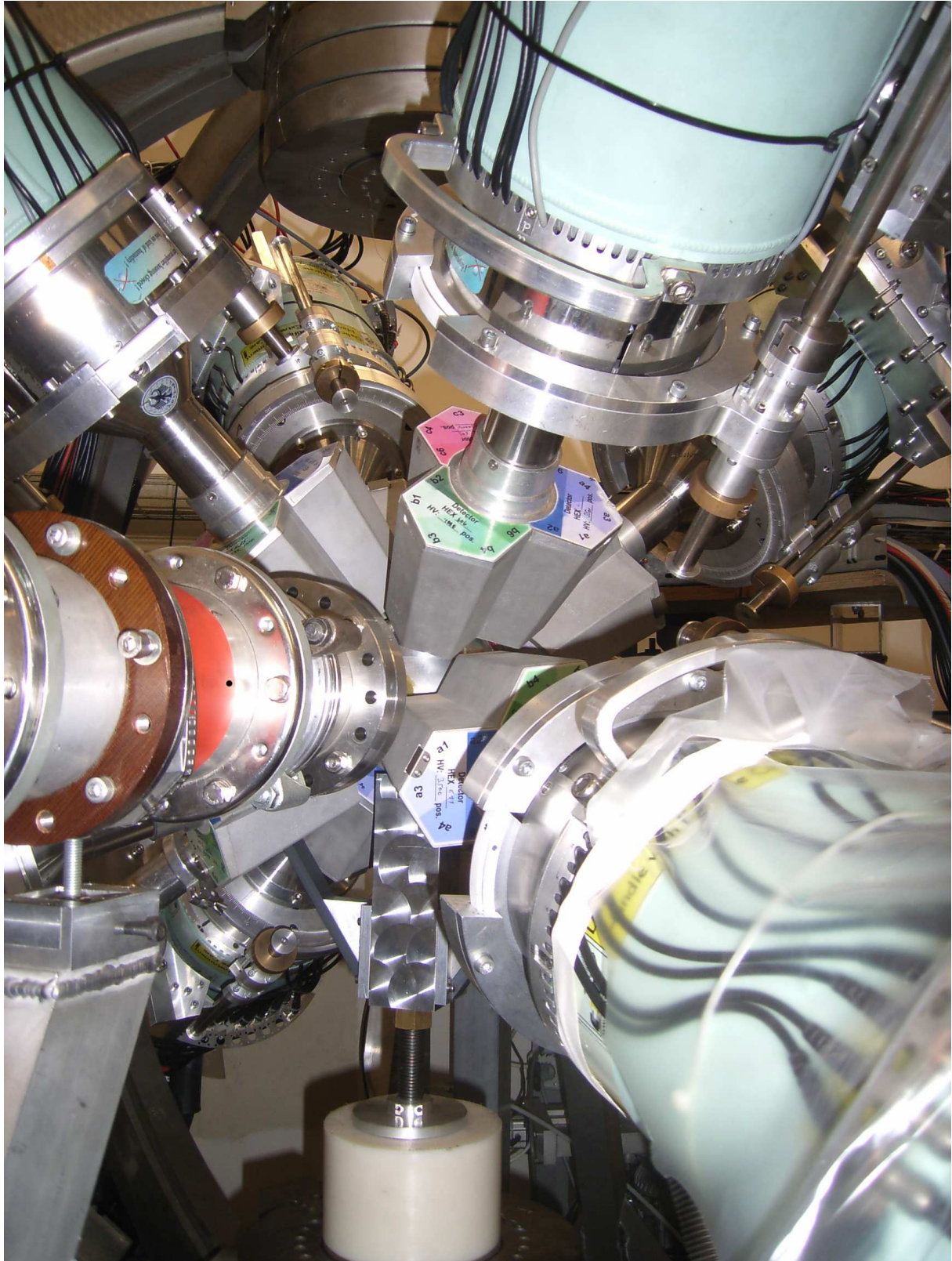


Figure 3.4: MINIBALL spectrometer as used for the present experiments on ^{237}fPu at the Tandem accelerator of IKP, Cologne. The target chamber at the centre of the set up contains the PPAC array and the target, while the beam is entering from the left.

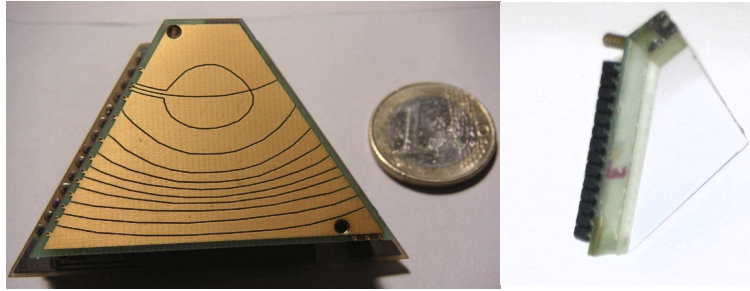


Figure 3.5: Left: a photograph of the segmented PPAC anode board. Right: a photograph of one of the 8 trapezoidal PPAC modules (seen from the entrance foil with the preamplifier electronics at the back side).

parallel plate avalanche counters (PPAC) was built ($d\Omega/4\pi = 74\%$). The design of the PPAC array shown here is an adaption to the design initially realised by D. Pansegrau [PAN98] for Heidelberg experiments on ^{240}fPu . The individual PPAC module is set up (see Figure 3.5) with a segmented anode back plate onto which an epoxy spacer frame carrying the cathode foil is glued. On top of this cathode foil a further spacer frame carrying the entrance window is positioned (see Fig. 3.8 for a schematic overview). Details on the PPAC design are given at the end of this section. The time at which the fission fragments are detected in the PPAC (relative to the beam pulse) depends on the time of the fission process and the time of flight of the fragments (arbitrarily set to $t=0$ for prompt fission fragments), which is mainly given by the fragment emission angle, resulting in a strong variation of the fragment velocities behind the target due to their angular-dependent flight path within the thick target. Thus the velocity of the fragments is dependent on the fission fragment mass distribution and the energy loss in the target. The position-sensitive PPAC modules enable a reconstruction of the flight path and the emission angle of the fragment from the target. Thus an optimised time of flight distribution for the different flight paths can be achieved, reducing the width of the fission fragment time distribution and thereby increasing the experimental efficiency for the delayed fission fragment detection by an improved separation sensitivity between prompt and delayed fission events.

Geometry and Segmentation of the PPAC modules

By detecting both fission fragments the determination of the fission time with respect to the prompt α beam pulse is significantly improved and thereby the distinction between prompt and delayed fission is enhanced. PPACs intrinsically exhibit a good time resolution and are able to cope with a high fission fragment rate (up to ≈ 20 kHz), they are the preferred choice in this type of experiments [PAN98]. The PPAC array used in this thesis will be described in the following section, with respect to the experimental necessities and the method of construction of the PPAC modules. The main objective in the construction of the PPAC array was to distinguish between the prompt fission fragments (from the $^{235}\text{U}(\alpha, 2n)^{237}\text{Pu}$ reaction) and the delayed fission fragments from the $^{235}\text{U}(\alpha, 2n)^{237\text{f}}\text{Pu}$ reaction.

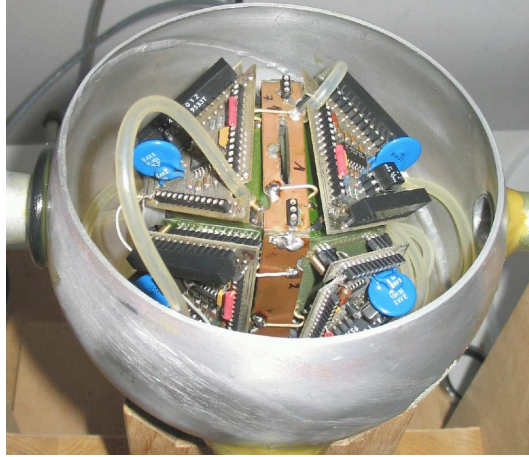


Figure 3.6: The 4π PPAC array in its target chamber (diameter ≈ 15 cm). Visible are 4 of the eight PPAC modules together with their preamplifiers and the gas feeding lines. The ^{235}U target is inserted from the top via the narrow slit opening between the two hemispheres.

The compound nucleus ^{237}Pu is stopped within 0.1 ps in the ^{235}U target, from where it subsequently decays via fission. The two maxima of the mass distribution of the fission fragments are situated around $N = 100$ and $N = 140$, respectively [COL61] with typical kinetic energies of 75 to 100 MeV. The energy loss of the fission fragments in the target is small enough, so that both fission fragments can leave the target in opposite direction. The energy loss in the target is governed by the Bethe-Bloch equation [POV01] and depends on the charge of the target material, the charge and energy of the fission fragment, the position within the target and the exit angle from the target. With an expected target thickness of ≈ 3 mg/cm², the typical energy loss is expected to be in the region of 40 to 50 % and for large exit angles amounts to up to 99 % of the initial kinetic energy of about e.g. 75 MeV for the heavy fission fragment.

The time at which the fission fragments are detected in the PPAC (relative to the beam pulse) is given by the fission lifetime and the time of flight of the fission fragments, which depends on the fragment flight path and the fragment mass and velocity. Whilst the fragment flight path is given by the geometry of the PPAC array, the fragment velocity depends on the fragment mass distribution and the energy loss experienced in the target, which in turn is dependent on the exit angle θ_{frag} from and the position within the target. Using a position-sensitive PPAC, the flight path and the exit angle can be measured, whilst the variation of the fragment mass and the position of fission in the target can not, leading to an increase of the width of the fragment flight distribution. As in the analysis (see chapter 4.2) a correction to the fragment flight time is used, the set up of the segmented PPAC anode has to be designed in such a way that a narrow flight time distribution is obtained.

Thus the detector system has to fulfill the following requirements: As the flight time distribution is linearly dependent on the length of the flight path, the distance between target and detector should be as small as possible. Furthermore, a compact arrangement of the PPAC array is beneficial to the MINIBALL germanium detector array as the photopeak efficiency is

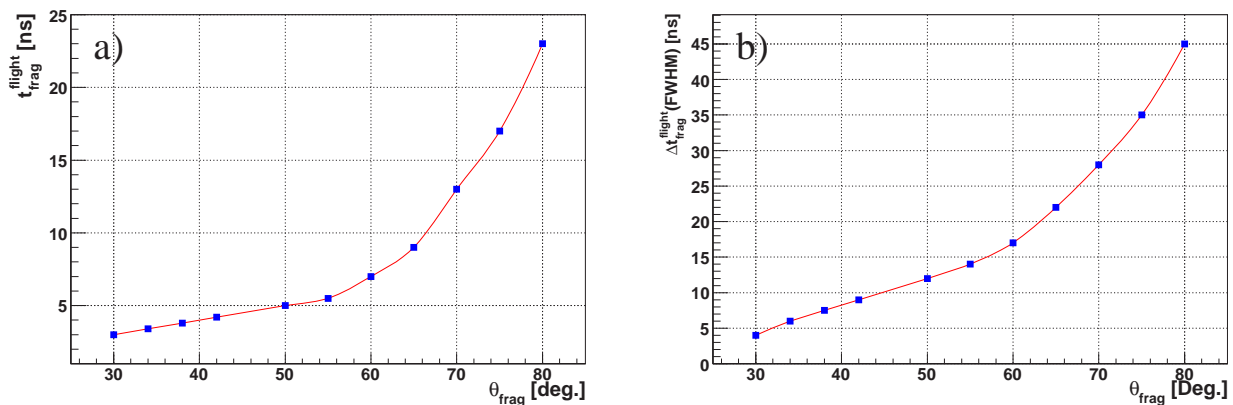


Figure 3.7: Panel a): angular dependent fission fragment time of flight for a low energy (75 MeV) high mass ($A = 132$) fission fragment to one of the PPAC modules is displayed. Panel b): angular dependent width of the flight time distribution is shown. Both spectra are calculated for a 3 mg/cm^2 thick ^{235}U target and the axis perpendicular to the detector surface has been chosen as $\theta_{frag} = 0^\circ$.

dependent on the solid angle covered (distance MINIBALL to target $\sim 10.5 \text{ cm}$). As the width of the flight time distribution and the flight time vary with the exit angle, the PPACs were segmented. The 13 anode segments (see Fig. 3.5) were chosen such that they covered regions of nearly equal flight times. For large exit angles ($65^\circ \leq \theta_{frag} \leq 77^\circ$) the width (FWHM) of the flight time distribution will be $\sim 20\text{-}35 \text{ ns}$ compared to $\sim 4\text{-}12 \text{ ns}$ for $30^\circ \leq \theta_{frag} \leq 48^\circ$ as can be derived from the simulation calculations of the flight time distribution of fission fragments displayed in Fig. 3.7. So it is necessary to minimise the flight path for fission fragments with large exit angles. The time resolution of the PPACs should be less than the expected width of the flight time distribution (i.e. $\leq 1 \text{ ns}$). Furthermore, as the flight time and the flight path for the fission fragments, emitted back to back, can vary significantly, it is important that both fragments are detected in kinematical coincidence for an accurate reconstruction of the flight time and the time of fission. Therefore a large solid angle coverage is desirable.

To determine the optimum geometry and segmentation of the PPAC array, the flight time distribution of the fission fragments was simulated as a function of the exit angle from the target for a target thickness of 3 mg/cm^2 . The following factors were considered in the simulation: i) the flight path, which is dependent on PPAC geometry and the fission axis. ii) the energy loss in the target, which is dependent on the exit angle and the position of fission in the target. iii) the kinetic energy of the fission fragments, which is dependent on the fragment mass (taken from [COL61]. Fig. 3.7 a) displays the resulting flight - time distribution for a low - energy (75 MeV) and thus heavy - mass ($A = 132$) fission fragment, while panel b) shows the corresponding width of the distribution from angular and energy straggling effects.

In the investigation of ^{240}Pu [PAN98] it was shown that the best geometry consists of two four - sided pyramids, back to back with the target placed at the centre of a "double pyramid".

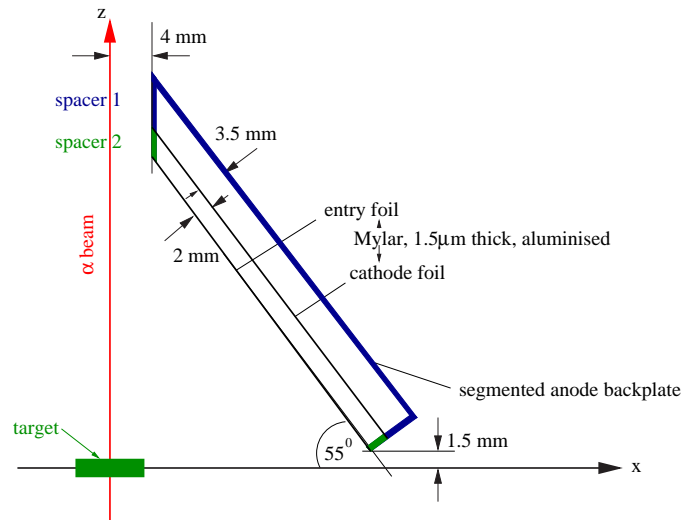


Figure 3.8: Construction of a PPAC module. A cut through the x-y plane of the PPAC array is shown, where the beam axis is defining the z-axis.

In this geometry the α beam enters and leaves the detector at the top of the pyramids, and it was found that the typical flight time of the fission fragments is 1.5 to 2.5 ns for a target thickness of 1.7 mg/cm^2 . Fig. 3.8 shows a cut through the PPAC array in the x-y plane, the α beam follows the z axis. The 1 mm thick spacer and foil holder frames have been manufactured by casting liquid epoxy resin into a specially developed mould. Fig. 3.9 shows a schematical top view of one of the trapezoidal modules, indicating all relevant dimensions, while Fig. 3.10 shows the 3 main parts of each module, the segmented anode back plate and the two epoxy spacer and foil holder frames. The back plate of the counter represents the segmented anode, to which the first of the two spacer frames is glued, which at the same time carries the $1.5 \mu\text{m}$ thick cathode foil (aluminium-coated Mylar foil). The second spacer is then placed on top of the cathode foil, which is serated at the edges to enable a gas flow between the two gas volumes, the entrance window is then glued to this spacer frame (entrance window: $1.5 \mu\text{m}$ thick aluminised Mylar foil).

The distance between the PPAC and the target (see Fig. 3.8) could not be reduced any further, as the individual epoxy frames of the PPAC modules could not be produced thinner than 1 mm thickness. Furthermore, the PPAC could not be produced smaller, as this would have increased the amount of "dead" solid angle due to the epoxy frame material, thereby reducing the detection efficiency. Also a reduced size would have increased the detection rate per segment, thus increasing the likelihood of sparking between the field plates of the PPAC modules. The entrance window and the cathode foil are $1.5 \mu\text{m}$ thick single sided aluminised Mylar foils. Figs. 3.9 and 3.8 show the schematical drawings required as a starting point to build the mould from which the epoxy resin frames were cast.

From the simulations of the fission fragment flight time distribution the segmentation of the PPAC array was derived. The shape of the segments was chosen such that each segment covered regions with a similar flight time range. Fig. 3.5 shows the anode back plate with

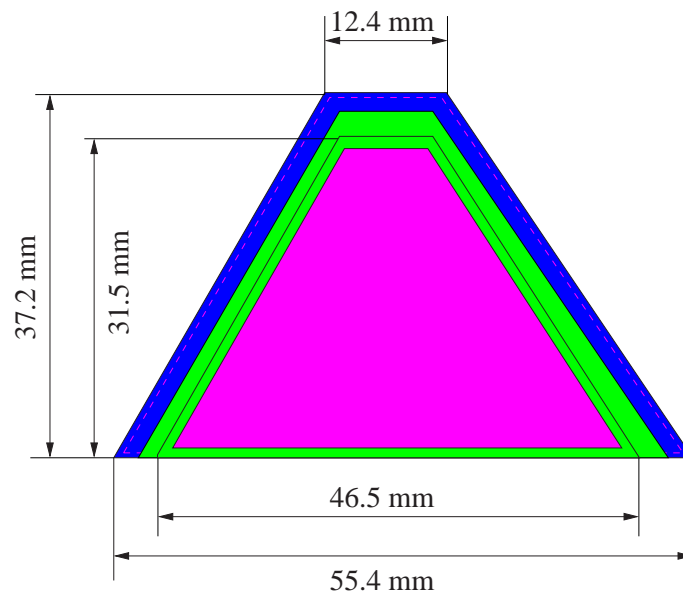


Figure 3.9: Schematic top view of a PPAC counter with all relevant dimensions. Indicated in blue is spacer frame 1, in green spacer frame 2 and the entrance window is indicated in magenta.

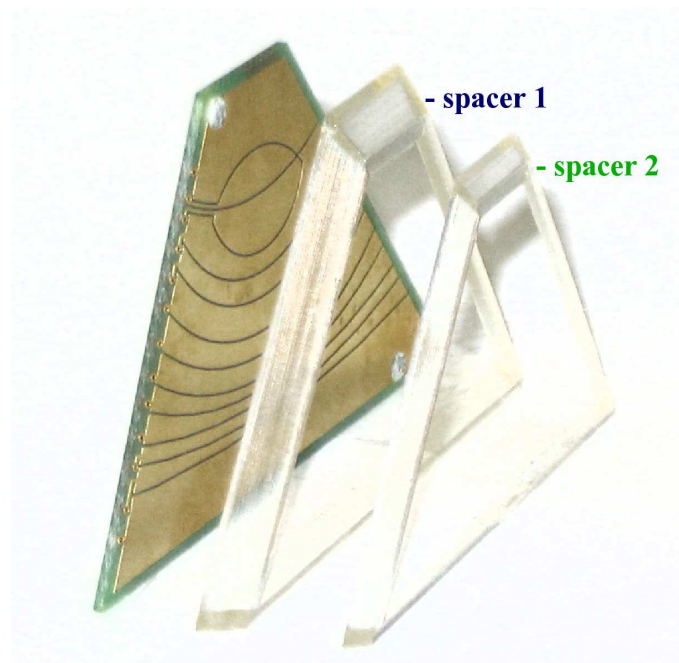


Figure 3.10: From left to right the 13-fold segmented anode back plate, the epoxy spacer frame between the anode back plate and the cathode ("spacer 1"), and the spacer frame between the cathode foil and the entrance window ("spacer 2") are shown.

the 13 individual segments of the PPAC array. For a ^{235}U target of thickness 3 mg/cm^2 , the average flight time varied from 3 ns to 23 ns. The difference in the mean flight time covered in (the innermost) segments 1 to 5 is 0.4 ns for an average width of the flight time distribution of 3 ns. For segments 6 to 9, corresponding to exit angles between $40^\circ \leq \theta_{frag} \leq 55^\circ$, this value is increased to $\sim 4\text{-}6$ ns for an increased width of the flight time distribution of about 12 ns. For large exit angles the energy loss in the target is significantly increased, for this reason segments 9 to 13 shown in Fig. 3.5 have been combined during the analysis into a common channel. Furthermore, the energy loss of the fission fragments in the entrance foil to the PPACs is typically 10 % and the range of a 75 MeV fission fragment of mass $A \approx 132$ is 4 mg/cm^2 . The angular coverage of the active detector volume is given by $30^\circ \leq \theta_{frag} \leq 77^\circ$ (where θ_{frag} is the angle between the beam and the fragment exit angle from the target). The solid angle covered is 74 %.

If a fission fragment enters the detector volume between the cathode foil and the anode back plate, electron-ion pairs are produced in the detector gas (in our case isobutane, operated at 5 mbar pressure), causing an avalanche of secondary electrons in the electric field (operating voltage $\sim 410\text{ V}$, trip voltage 440 V_x). This charge distribution is then accelerated to the anode back plate in the electric field with a typical distribution width of 1.5 mm (at a distance of 3.5 mm). The charge distribution on the anode induces a mirror charge on the cathode, which is five to six times wider than the initial charge distribution. For this reason the segmented back plate was chosen as the anode, so that the electrons are accelerated towards the segmented back plate. The signal amplitude (typically 150 mV behind the preamplifier) from the cathode foil was used as a trigger for the time measurements.

Set up of the PPAC array

The PPAC array consists of eight of the trapezoidal PPAC modules as described before, put together forming an octaeder, which is held together by a central frame into which the target is inserted via a narrow slit. The modular design of the PPAC array was chosen such that individual modules can easily be accessed and replaced if needed. In order to improve the signal-to-noise ratio of the PPAC signals, the preamplifier board was connected directly to the anode plate via a plug and socket connection on the back side of the PPAC module. The 4π PPAC arrangement allows to detect both fission fragments in coincidence with large solid angle coverage of $\sim 74\%$. In view of the fact that a target of 3.7 mg/cm^2 thickness was used, as opposed to the 3 mg/cm^2 used for the simulation of the segment time of flight, segments 9 to 13 were hard wired on the PPAC anode board to one segment as the Bragg peak for the high-mass, low-energy fragments lies within the ^{235}U target and therefore the signal yield from these segments is negligible. Fig. 3.11 shows a picture of the complete PPAC array prior to the installation in the target chamber, the gas connections and the electronics cabling are performed inside the target chamber.

The eight modules are hooked up in parallel via flexible rubber hoses to the gas control system, operated in flow-through mode at a constant isobutane pressure of 5 mbar. The four

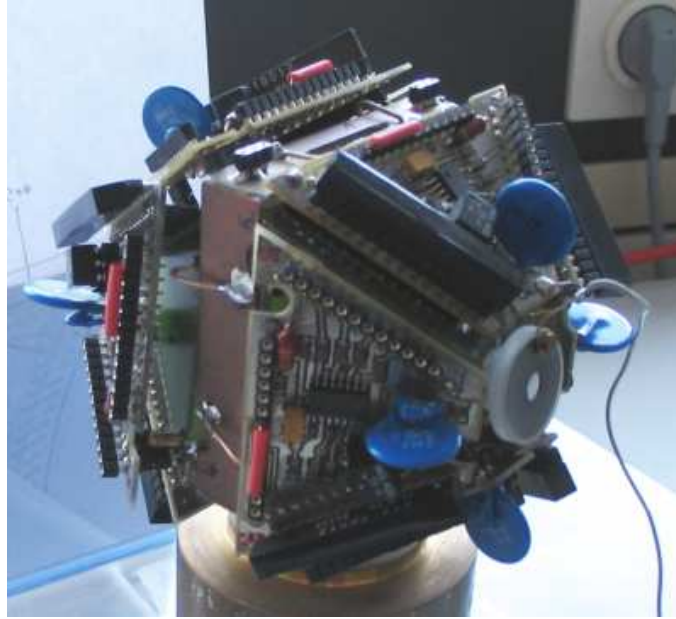


Figure 3.11: The assembled PPAC array prior to its installation in the target chamber. The slit for the insertion of the target can be seen on the top part of the central frame, while the entrance aperture to the target chamber is visible at the right hand side.

electric connections (HV supply, cathode signal, 2 anode signals) from the PPAC are guided through to the target chamber to the feed through flange using adapted coaxial cables. The spherical target chamber is made of 1 mm thick aluminium and has an external diameter of 15 cm. The gas supply and the electronics cabling is fed through two tube extensions to the chamber and guided to the PPAC array. The vacuum pressure typically obtained in the target chamber was 8×10^{-6} mbar under operational conditions of the PPAC array.

3.3 Readout electronics and data acquisition

The MINIBALL array is not only a novel γ -spectrometer in view of its position-sensitive γ -ray detection capabilities, innovative concepts have also been implemented for its signal processing electronics of the 24 germanium crystal core signals and the 144 detector segments. The preamplified MINIBALL signals are read out using CAMAC-based XIA DGF-4C digital electronics modules [XIA]. The "digital gamma finder" (DGF) modules digitise the preamplified charge signals from the Ge crystals using digital filters and subsequent field-programmable gate arrays (FPGAs) and digital signal processors (DSPs) at a sampling rate of 40 MHz and a readout time of $10 \mu\text{s}$. The DGF modules also allow to execute a user-specific pulse shape analysis algorithm in real-time (a feature that was not used in our experiment).

The signals from the PPAC array were digitised in CAEN V775 VME-based time-to-digital converters (TDCs) [CAEN]. The TDCs have an event buffer memory of 32 events, thus whenever 32 signals have been digitised, the corresponding TDC data have to be written to file or disk, leading to a TDC deadtime of $10 \mu\text{s}$. For the timing correlation between events with fission

fragment signals collected in the TDC buffers and γ -ray data registered in the DGF modules, a logic OR signal from all of the PPAC modules is fed into an additional DGF module, which serves as a time-stamping module ("TS DGF" in Fig. 3.12), deriving the event time from the master clock with a clock rate of 40 MHz.

For the data acquisition (DAQ) the MAR_aB Φ U system (MBS And Root based Online/Offline Utility) was used [MAR]. MAR_aB Φ U is based on the GSI Multi Branch System (MBS), that was developed to simultaneously collect data from various detector systems and data buses. The data from the individual data channels are written into individual memory buffers. Once a data buffer is full, a readout cycle is started, and the data are saved into a listmode format to disk. Using MAR_aB Φ U, this raw data are then sorted into individual events using an event-building process (see chapter 4.1), by matching the time (time stamp) allocated to each data buffer to the event time. It is therefore possible to correlate the particle and γ times. Furthermore, MAR_aB Φ U is able to create ROOT trees, which is a compact data format facilitating the offline analysis of the data using the ROOT framework [ROOT].

3.4 Hardware trigger

Fig. 3.12 shows a block diagram of the readout and trigger electronics used in the presented experiments. Only those events have been validated, where at least one γ ray and two corresponding fission fragments have been registered. The timing signals from the PPAC anodes and cathodes are processed in timing filter amplifiers (TFAs), whose output is then fed into constant fraction discriminators (CFDs). The CFD signals from the PPAC cathodes are used to create the particle trigger in coincidence with the beam pulse, to gain the required timing information (chap. 3.5). In order to select only those events where two fission fragments had been detected, the electronic signals from the PPAC array are separated into a front-side and a back-side hemisphere. A valid event requires the presence of at least one PPAC anode signal from either of the two hemispheres, reflecting the kinematical coincidence between two fission fragments. This signal is then used as the trigger signal for the readout electronics. Since for both the particle and γ events a signal readout time of $\sim 10 \mu\text{s}$ is required by the hardware, during which the system will not process any other signals, a $10 \mu\text{s}$ -long busy signal is generated. Only trigger signals are accepted in the absence of this busy signal. The TDCs are operated in a "Common Stop" mode, where the individual PPAC- and Ge-timing signals act as a start signal and the beam pulse is the stop signal. This then allows to reconstruct the relative time of the event.

3.5 The experiment

Following the planning of the experiment and the preparation of the setup described above, the setup was installed at the IKP in Cologne, where the MINIBALL array was located during the winter shut down period of the CERN-ISOLDE facility. Table 3.2 shows the relevant experimental count rates and intensities obtained during the beam time in Cologne. To populate the

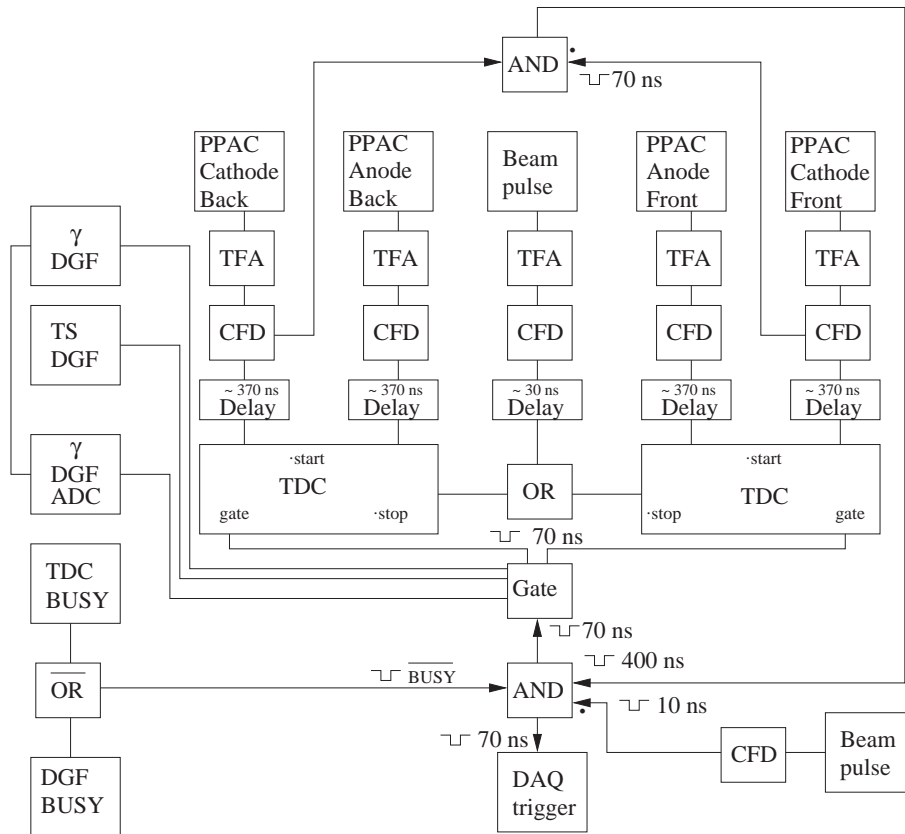


Figure 3.12: Block diagram of the signal processing electronics used. Only if the front - half and the back - half of the PPAC array trigger simultaneously, the system will be triggered as long as neither the DGFs or the TDCs are busy reading out the data. Indicated with a dot are the time decisive inputs to the logic coincidence units, and the signal widths of the logic signals.

Beam	α
Beam intensity	1 nA
Beam pulse period	400 ns
Beam pulse width	4 ns
Beam on target (Hrs)	396
Target	^{235}U
Target thickness	3.7 mg/cm^2
Overall Ge count rate	17 kHz
Overall PPAC count rate	1.2 kHz
Overall fission events	10^9

Table 3.2 Experimental parameters and rates for the experiment performed at the IKP Cologne to perform spectroscopy in the superdeformed second minimum.

fission isomers in ^{237}Pu a 24 MeV pulsed α beam was focused onto a 3.7 mg/cm^2 metallic ^{235}U target. The pulse period was chosen to be 400 ns, allowing ≈ 2.5 half-lives of the short-lived fission isomer in ^{237}Pu to be measured, whilst covering only $\approx 30\%$ of the half-life of the long-lived isomer. In a preparatory experiment, in which a 24 MeV pulsed α beam was focused onto a ^{232}Th target, the quality of the beam pulsing system running at a frequency of 5 MHz was investigated. Aiming at a clean time range of 400 ns between two selected pulses, the probability of spurious HF-generated pulses with $\Delta t = 200 \text{ ns}$ was measured to be $\leq 10^{-7}$, thus excluding their potential misinterpretation as delayed fission signals (occurring on the level of 10^{-5}). Using 1 nA of beam intensity, the average MINIBALL detector count rate was at approximately 17 kHz with an average fission fragment count rate of 1.2 kHz in the PPAC array. In total 500 Gb of data was recorded for the nearly 400 hours of beam time, in which $\sim 10^9$ prompt fission events were recorded. Following the experiment, the data channels were calibrated as described in the following chapter 4. The results are presented in chapter 5 and will be discussed in chapter 6.

Chapter 4

Preparation of experimental data

Spectroscopy of ^{237f}Pu was performed during a 3-week MINIBALL campaign at the IKP in Cologne. In the following chapter, the calibration and analysis of experimental data will be discussed. Starting with the event-building procedure (chap. 4.1), required to match all data between the different detectors, the calibration of the fission fragment (chapter 4.2) and γ ray data (chapter 4.3) will be discussed, to finally obtain a background-corrected γ -ray spectrum of ^{237f}Pu .

4.1 Event building

As described in chapter 3.3, the MINIBALL γ ray data was read out using CAMAC-based digital electronics modules [XIA], whilst the corresponding PPAC data was read out using VME-based TDC modules [CAEN]. For the data acquisition (DAQ) the MAR_aB_QU system was used [MAR]. To correlate the event data from the individual modules, the DAQ system has a master clock, known as the time stamping module, which assigns an event time (time stamp) to each data channel written to file on occurrence of the hardware trigger (see chap. 3.4), thereby also activating the DAQ. Once the data is written to file, the event-building procedure scans all data channels and correlates those non-zero channels with a matching time stamp into an event. Fig. 4.1 shows an example of how the PPAC data is correlated to the time stamp and consequently to the MINIBALL data.

The hardware trigger (see chap. 3.4) of the electronics readout system opened a gate for the MINIBALL ADC system with a width of 1600 ns, in our case spanning four cycles of the pulsed beam ($\Delta t = 400$ ns).

Figure 4.2 shows the particle and γ ray coincidence peak as a function of the time stamping value, from this we can see that the coincidence peak is situated at $T \sim 12.5$ ns. A time window of ± 500 ns was chosen, so that the random background peaks of two neighbouring beam pulses can be used in the timing calibration of the PPAC and the MINIBALL detector array, thus allowing to discriminate random coincidences from those γ rays originating from the actual beam pulse. Therefore in the event-building procedure only those γ rays registered within ± 500 ns of the registered time of the fission fragment were considered to belong to the same event. This width

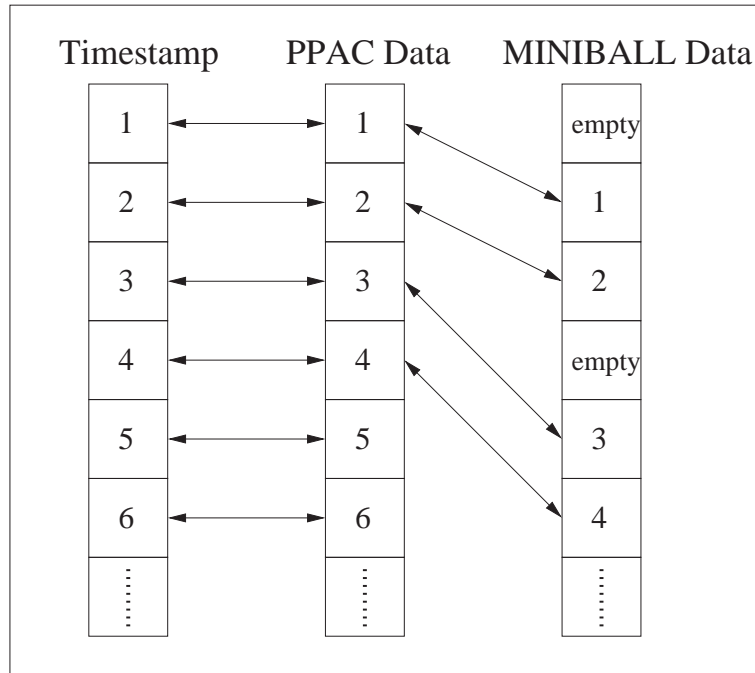


Figure 4.1: Example of the event-building procedure. Individual events from the different detector types are time-stamped with their event time, only non-zero events with matching time-stamps are correlated to an event.

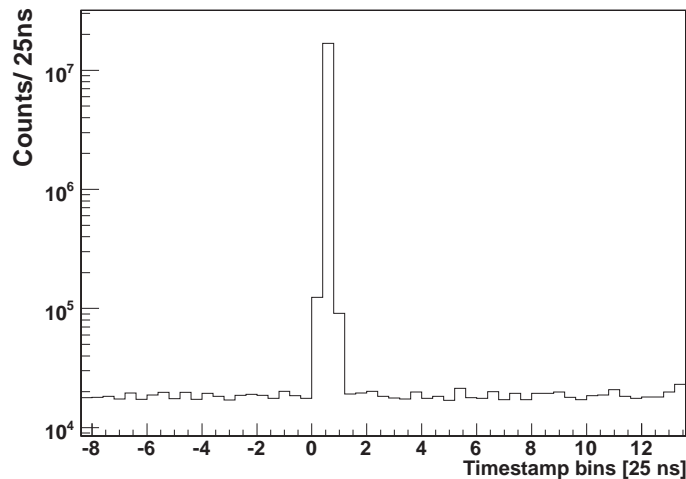


Figure 4.2: Time structure of the events recorded. The peak at the centre of the spectrum represents the coincidence peak between fission fragments and γ rays, obtained when the DAQ is triggered. The number of emitted γ rays in coincidence with fission fragments is up to three orders of magnitudes higher than those from background γ rays. The event time, being the time interval where digitally processed energy and time signals were considered to belong to the same event, was chosen such that only those γ rays registered within ± 500 ns (20 timestamp bins) relative to the fission fragments were accepted and reconstructed to an event.

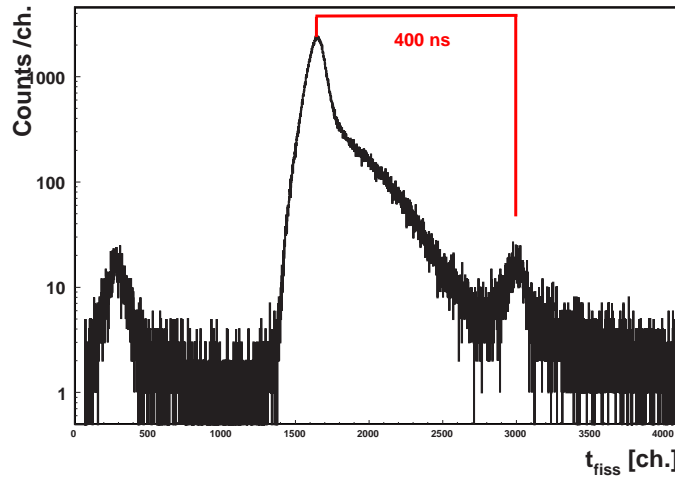


Figure 4.3: Time structure of γ rays in one of the individual MINIBALL Ge detectors. In the centre of the spectrum the correlated γ rays from the prompt fission following the $^{235}\text{U}(\alpha,2n)$ reaction are visible. This spectrum was used for the γ time calibration (see chap. 4.3.2).

was chosen in order to use the two neighbouring beam pulse peaks in the spectra for the timing calibration of the individual detector components.

Figure 4.3 shows a typical time spectrum of one individual MINIBALL Ge detector, resulting from the above described event - building procedure. At the centre of the spectrum those γ rays occurring with the correlated fission fragments and the beam pulse can be seen. To the left and right of this peak two further peaks in γ - ray intensity can be seen, belonging to the neighbouring beam pulses, and thus forming random background.

4.2 PPAC data calibration

The function of the 4π PPAC array was to detect the fission fragments following the $^{235}\text{U}(\alpha,2n)^{237}\text{Pu}$ reaction, and to distinguish these as either prompt fission background or belonging to the decay of the fission isomers populated in ^{237}fPu . The cathode signals delivered a time signal relative to the beam pulse, while the anode signals provided a position - sensitive signal to allow for a correction on the angular - dependent fragment time of flight (see chap. 3.2.2). Fig. 4.4 shows the typical anode time spectrum. Indicated are the nine signal bins, into which the 13 anode segments have been combined. As both output signals from the delay lines providing the anode signals were registered, the fragment position could be determined from the ratio between the timing signals of the two anode delay line readouts (see chap. 3.2.2). The position of the fission fragments detected with the segments of a PPAC module could be determined to an accuracy of ~ 3 mm. Only those events where both anode signals and a cathode signal were recorded for one fission fragment in a PPAC module were used in the further data analysis. 85 % of all fission events fulfilled this condition. Furthermore, the coincident fission fragments had to be registered within ± 150 ns.

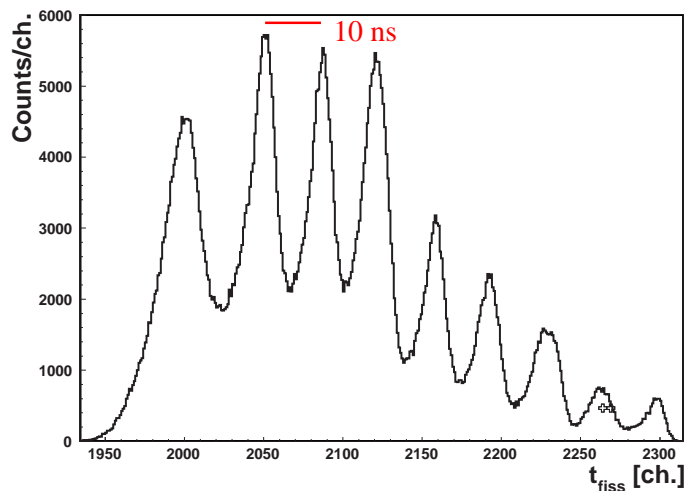


Figure 4.4: Typical anode time spectrum of one of the eight PPAC modules. Shown are the segments 1-9 of PPAC counter 1 situated on the back-side hemisphere of the PPAC array. The peak positions of the nine segments are 10 ns apart, given by the delay-line readout. The difference in intensities is due to the solid angle covered by the individual segments of the PPAC cathode.

Figure 4.5 shows a typical cathode time spectrum of one of the PPAC module signals. All TDC signals were recorded using a "common stop" mode, i.e. the TDC was started with the individual PPAC time signals and stopped by the beam pulse. The time spectrum was calibrated by analysing the central position of the three beam pulse signals present in the spectrum, being separated by 400 ns each. Only those events where both fission fragments were detected with time signals delayed by at most 370 ns with respect to the prompt beam pulse are distinguished as a delayed fission event. If a ^{237}Pu nucleus is produced in the $^{235}\text{U}(\alpha, 2n)$ reaction and subsequently undergoes prompt fission decay emitting two fragments in opposite directions, one fragment may be identified as being prompt, however, the energy loss of the second fragment in the thick ($3.7\text{mg}/\text{cm}^2$) target may make this appear as a delayed fission fragment as it is slowed down on its trajectory through the target into the detector. So by applying the following conditions it was decided on whether events either belonged to the strong background of prompt fission or to the desired rare delayed fission component: For each event two fission fragments had to be detected, where the anode segment that registered the fission fragment was identified by the maximum energy registered in one of the nine anode signal bins. Due to angular straggling in the thick ^{235}U target, all pairs of fission fragments were detected with a relative angular difference of 180 ± 30 degrees. Moreover, according to the angular-dependent flight time distribution of fission fragments, both cathode signals had to be delayed by 70 to 90 ns with respect to the prompt beam pulse. Unfortunately the energy loss of the fission fragments in the target (and consequently the spread of the flight time distribution) was so high that only 270 ns of the 400 ns wide beam pulse window could effectively be used in the further analysis

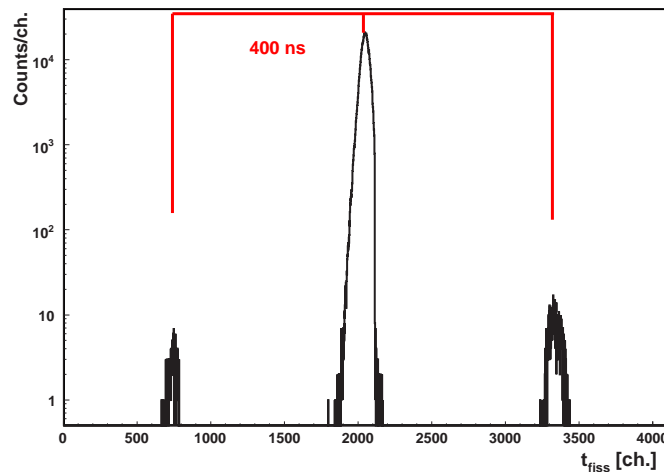


Figure 4.5: Typical cathode time spectrum from one of the eight PPAC modules. Shown is the TDC time spectrum, where the PPAC start signal is stopped with the beam pulse. There are three peaks visible in the spectrum, where the dominant middle peak represents the desired beam pulse, while the other two arise from neighbouring beam pulses at ± 400 ns. Using a ^{232}Th target, the probability of the beam pulse HF system to produce spurious pulses with $\Delta t = 200$ ns was tested to be less than 10^{-7} .

of ^{237}fPu . The time calibration was performed for each individual run, in order to allow for a continuous compensation of eventual time signal drifts. Applying these conditions, the fission time spectrum in Fig. 4.6 was generated. The delayed fission component consists of two fission isomers, a short-lived isomer with a half-life of 110 ns and a long-lived isomer with a half-life of 1120 ns [RUS71, VAN73, SPE74], the actual half-lives detected are discussed in chapter 4.6. Fig. 4.6 shows the fission time spectrum after the first 24 hours of beam time. The shoulder in the peak is due to a drastic increase in the angular dependent flight time at large exit angles due to the thick target.

4.3 MINIBALL data calibration

The MINIBALL germanium detector array was used to detect the γ rays emitted from the $^{235}\text{U}(\alpha, 2n)^{237}\text{fPu}$ reaction. Prior to and following the beamtime, the 24 MINIBALL Ge detectors were calibrated using a ^{152}Eu source placed at the target position (see Table 4.3 for the corresponding individual characteristic γ transitions). Figure 4.7 shows a typical example of the energy calibration curve for one of the germanium detectors. Performing this calibration the energy resolution (FWHM) of the MINIBALL detector array is shown to be 2.9 keV at $E_\gamma = 1.3$ MeV (equivalent to $\frac{\Delta E}{E} = 0.22\%$). A linear fit was performed to calibrate the MINIBALL detector array, as the quadratic term in a second order polynomial fit would be smaller than 0.0034 %.

Exploiting the two-photon cascades in ^{152}Eu , the calibration data can also be used to deter-

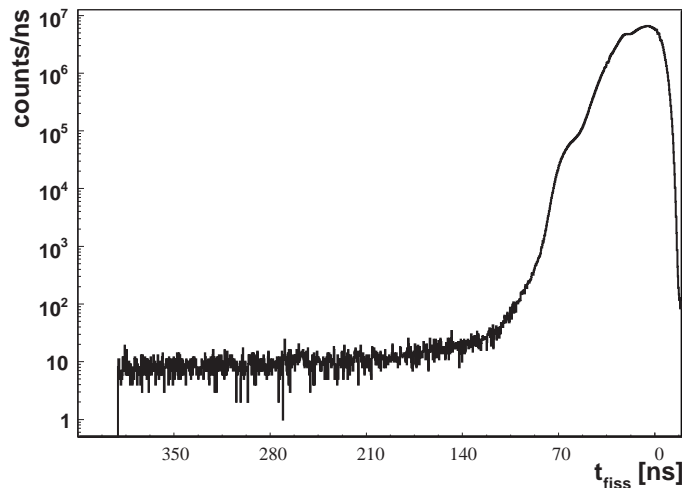


Figure 4.6: Fission time spectrum relative to the beam pulse of the first 24 hours of beam time, as accumulated for all eight PPAC modules corrected for shifts in time.

mine the absolute photopeak efficiency curve of the germanium detectors, taking into account the coincidence ratios between the corresponding γ transitions listed in [FIR96] together with the characteristics of the γ ray calibration source (Tab. 4.3).

In order to monitor the stability of the MINIBALL detector energy calibration during the three-week MINIBALL campaign, the position of background γ -rays arising from scattered neutrons reacting with the target chamber and the Ge detectors, X-rays from Pb and the 511 keV γ rays resulting from electron-positron pair annihilation were analysed as a function of the run time and time-dependent modifications of the energy calibration were applied on a run-by-run basis. Figure 4.8 shows the γ -ray energy spectrum summed over all 24 MINIBALL detectors, resulting from a coincidence with prompt fission (region A in Fig. 4.13). Data were taken during the MINIBALL campaign for 2 hour long runs, the background transitions are indicated. For all 263 runs and for each Ge detector the energy calibration was checked and compared to the energy calibration performed using the ^{152}Eu source. It turned out that the energy calibration fluctuated only by up to 0.5% over the three-week beam time period. This change in the energy calibration was corrected for.

4.3.1 MINIBALL photopeak efficiency

In addition to the energy calibration, the absolute photopeak efficiency of the MINIBALL spectrometer was measured using a ^{152}Eu source (190 kBq). Exploiting the coincident γ cascades of the 121 keV/1408 keV and 344 keV/778 keV transitions, respectively, which are listed in Table 4.1 together with their respective coincidence ratios [FIR96], by gating on one of the γ transitions in a single Ge crystal the photopeak efficiency for the corresponding coincident transition could be determined simply by counting the number of registered photopeak events in the rest of the MINIBALL array. This resulted in a photopeak efficiency of $\varepsilon_{ph} \sim 8.6\%$ at 1.3 MeV γ energy,

E_γ [keV]	Intensity per desintegration	Coincident with
121.780	0.286	1408.030
244.664	0.0745	-
344.306	0.267	778.880
411.114	0.0224	-
443.968	0.0310	-
778.880	0.129	344.306
867.330	0.041	-
964.013	0.146	-
1085.817	0.0998	-
1112.050	0.135	-
1408.030	0.208	121.780

Table 4.1: Properties of the ^{152}Eu γ ray calibration source used for the MINIBALL germanium detector energy and efficiency calibration (taken from [PEL82, FIR96] and references therein).

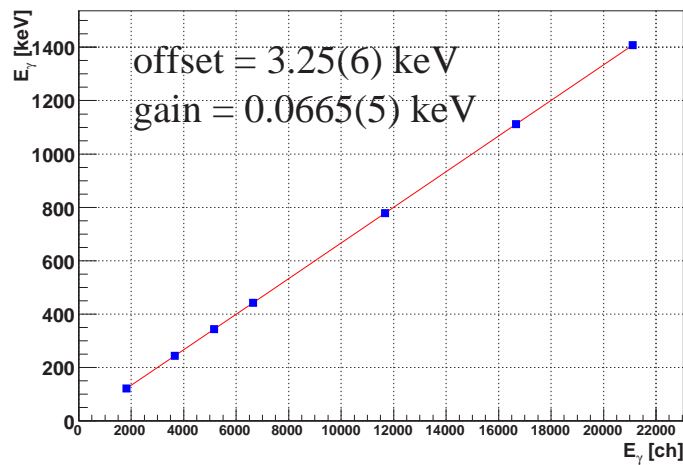


Figure 4.7: Typical linear γ -ray energy calibration curve detected in one of the MINIBALL germanium detectors, determined using a ^{152}Eu source.

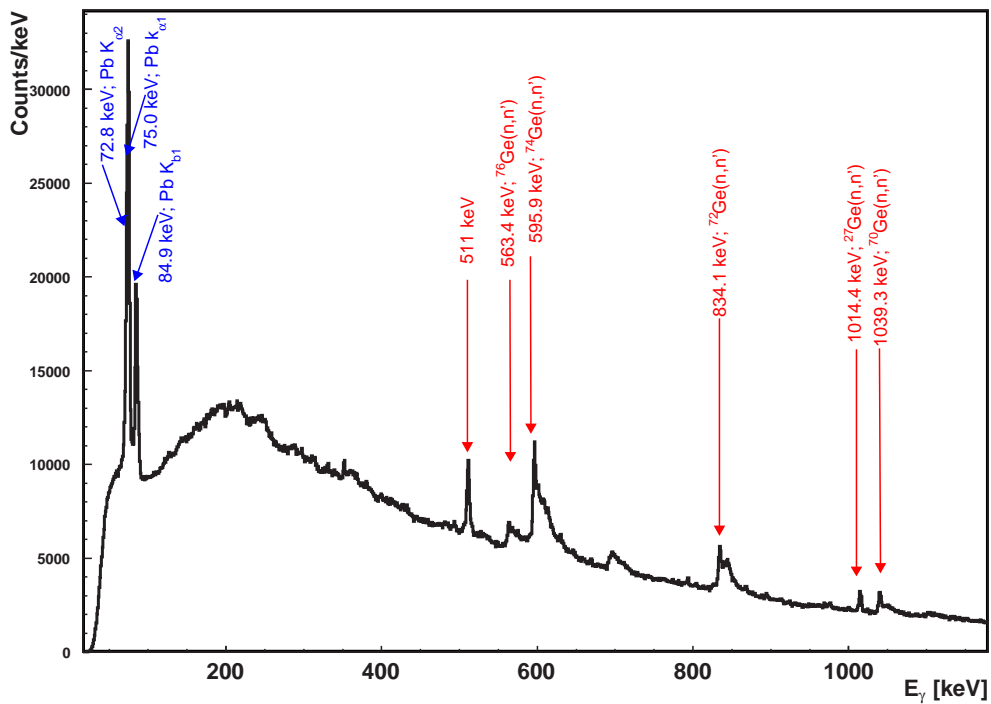


Figure 4.8: γ -ray energy spectrum following the $^{235}\text{U}(\alpha, 2n)$ reaction measured with all MINIBALL detectors. Indicated are the strong background γ rays resulting from neutron reactions with the aluminium target chamber, germanium in the MINIBALL detector array (marked in red) and Pb X-rays (blue) resulting from scattered α -beam particles on the Pb entrance aperture to the target chamber. The marked transitions were used for a run-by-run stabilisation of the energy calibration.

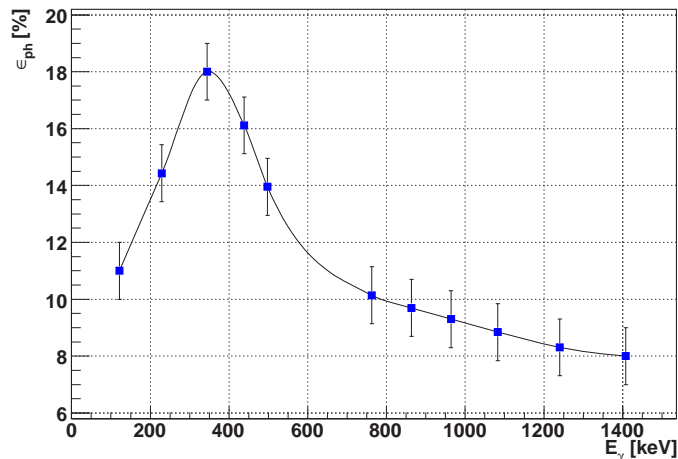


Figure 4.9: Absolute γ -ray photopeak efficiency for the MINIBALL detector array. Shown are the measured photopeak efficiencies using a ^{152}Eu source (square symbols) together with the resulting (interpolated) efficiency curve (solid line).

which is in good agreement with earlier measurements [WEI03, STR05]. Figure 4.9 shows the measured photopeak detection efficiency curve of the MINIBALL detector array, which later will be used for the correction towards absolute γ -ray intensities. It shows that a maximum detection efficiency of 18% was achieved at ~ 350 keV. The CFD trigger threshold was set to ~ 80 keV in the DGFs for the MINIBALL detectors. The decrease in γ efficiency below ~ 250 keV is due to the absorption of γ rays in the target chamber, MINIBALL detector housing, etc..

4.3.2 MINIBALL time calibration

In a similar process to calibrating the PPAC times also the time calibration of the MINIBALL spectrometer was performed. Figure 4.10 shows the TDC time spectrum for γ rays relative to the pulsed α beam. The beam was pulsed with 5 MHz ($\Delta t = 400$ ns) with a pulse width of approximately 4 ns, so the centroids of the three peaks visible in Fig. 4.10 are separated by 400 ns. By applying a linear fit to the time-dependent centroids of the registered time peaks in the TDC spectrum, a time calibration for each of the germanium detectors was performed. The γ -timing spectrum is dominated by background from prompt fission events, while the tail to longer times visible in Fig. 4.3 can be attributed to delayed γ rays from (n, γ) reactions in the target chamber and detector materials as well as to delayed γ rays from fission fragments.

Figure 4.11 shows the E-T correlation measured with one of the germanium detectors, exhibiting a strong uncompensated walk of the constant fraction discriminator for γ energies below 300 keV. This was corrected for in the analysis, so that the low-energy γ rays now only exhibit a width of the time distribution of 100 ns compared to 330 ns prior to the correction. Fig. 4.12 shows the energy dependent time resolution of the MINIBALL detectors, which is significantly reduced below 300 keV. In this energy regime the photoelectric effect starts to

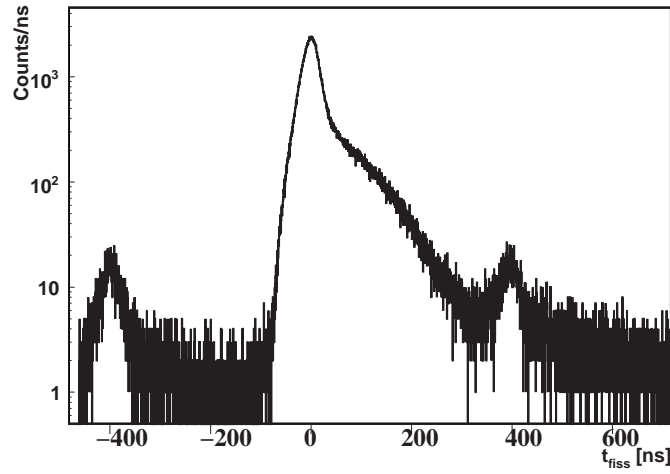


Figure 4.10: Calibrated time structure of γ rays in one of the individual MINIBALL Ge detectors. In the centre of the spectrum the correlated γ rays from the prompt fission following the $^{235}\text{U}(\alpha,2n)$ reaction are visible. This spectrum was used for the γ time calibration (see chap. 4.3.2).

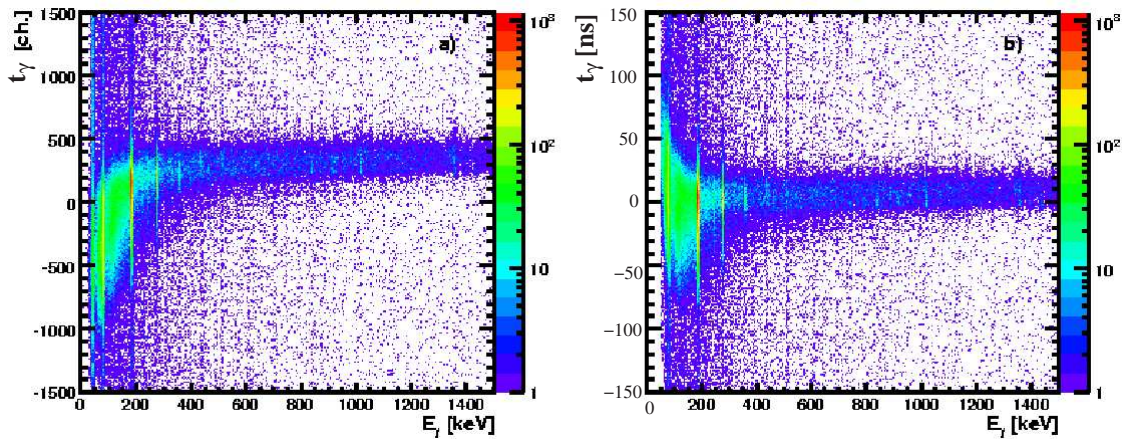


Figure 4.11: Left: energy - time correlation of γ rays registered in one of the germanium detectors is displayed, prior to the correction of the CFD walk effect. Right: the energy - time correlation of γ rays in the same detector is shown following the walk correction.

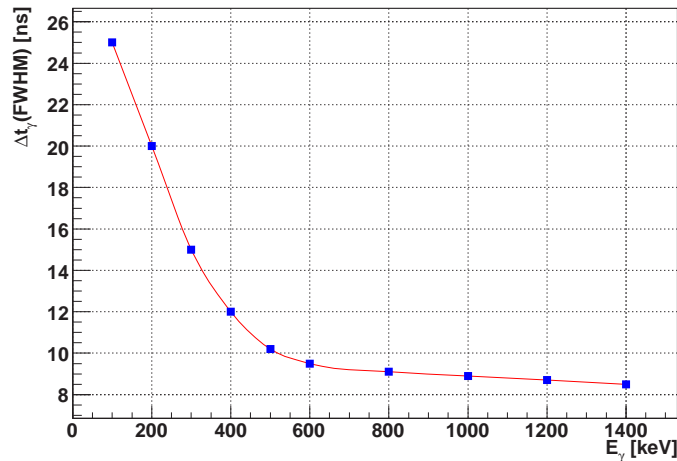


Figure 4.12: Energy dependent time resolution of a typical MINIBALL germanium γ -ray detector. The large decrease of the resolution (Δt_γ (FWHM)) at low γ energies is due to the inherently reduced time resolution of the detector material in this energy range (see text).

dominate over Compton scattering, which determines the detector response for higher energies. Here the incoming photon is directly absorbed by the detector material, while the resulting photo electron is accelerated in an electric field towards the core contact of the Ge detector, where it induces an electric signal. The smaller this γ energy is, the shorter the interaction length of the photons in the front part of the detector material and the longer the drift of the photo electrons towards the electrical contacts, thus giving rise to the significant broadening of the time resolution.

4.3.3 Background correction

Figure 4.13 displays the timing correlations between fission fragments and γ rays. The dominant component stems from the prompt γ rays arising from the prompt fission events (region A), whilst the interesting events with prompt γ rays in coincidence with isomeric fission fragments can be found in region B, the separation of the two components is obtained by gating on the walk-corrected energy-dependent time signal of the MINIBALL detectors and the coincident fission fragments. A third component (region C) is visible, comprised of delayed γ rays following the delayed fission of shape isomers. A fourth region D is indicated, this is used for the subtraction of random background. γ rays emitted from the decay of shape isomeric excited states of ^{237}Pu occur within the typical lifetime of rotational states (\approx picoseconds after the excitation of the shape isomer), while the isomeric ground-state decays via delayed fission after the lifetime of the respective shape isomer. Therefore the time window accessible for the analysis of fission fragments belonging to the shape isomers from the short-lived 115 ns isomer in ^{237}Pu covers approximately two half-lives, whilst for the long-lived isomer ($t_{1/2} = 1120$ ns) only a fraction of $\approx 20\%$ of isomeric decays could be analysed.

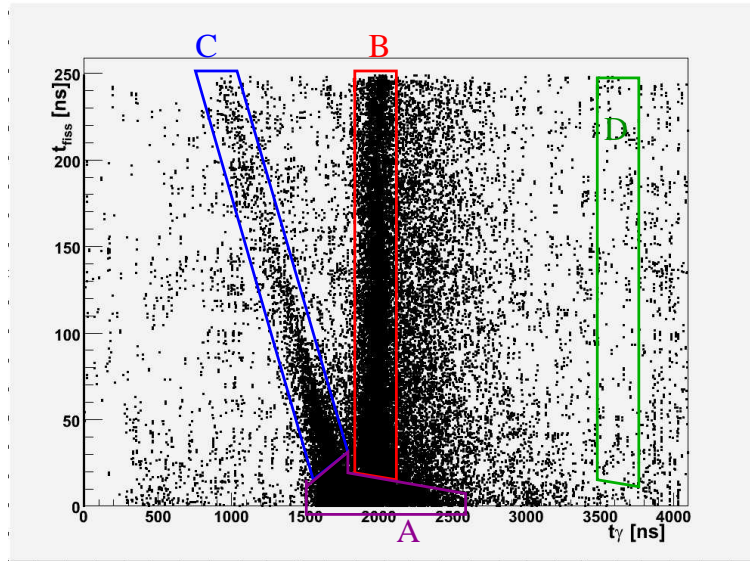


Figure 4.13: Timing correlation between fission fragments and γ rays. Highlighted are four different regions. Region A corresponds to the prompt γ -rays in coincidence with prompt fission fragments. Region B contains prompt γ -rays in coincidence with delayed fission fragments, while region C corresponds to the fission γ rays from the delayed fission fragments and region D (see Fig. 4.8) represents a region of random background.

Having calibrated the MINIBALL and PPAC data, the prompt γ -ray energy spectrum in coincidence with delayed fission events could be extracted. Gating only on those fission events, where both fission fragments are delayed by at least 70 to 90 ns (due to the energy loss in the thick ^{235}U target) with respect to the prompt α beam pulse, and selecting prompt γ rays within ± 30 ns of the beam pulse, results in the final spectrum of γ rays belonging to the shape isomers in $^{237\text{f}}\text{Pu}$ (see Fig. 4.13 region B). Figure 4.14 a) shows the γ -ray energy spectrum, summed over all 24 Ge detectors, obtained by gating on region B in Fig. 4.13 containing prompt γ rays in coincidence with delayed fission events. A background component from neutron-induced γ rays is visible (indicated with dashed lines in the spectrum of Fig. 4.14 a), furthermore it is assumed that a random background of γ rays is also present. For this reason the γ ray spectrum shown in Fig. 4.8 is normalised to the neutron-induced γ rays present in Fig. 4.14 a) and added to a random background component of γ rays obtained by gating on region D in Fig. 4.13 resulting in the background spectrum shown in Fig. 4.14 b). Subsequent subtraction of the γ ray spectrum shown in Fig. 4.14 b) from the spectrum in Fig. 4.14 a) results in the γ ray energy spectrum shown in Fig. 4.14 c). It was the task of the analysis described in chapters 5 and 7 to extract a level scheme for $^{237\text{f}}\text{Pu}$ from this rather fragmented complex γ -ray energy spectrum.

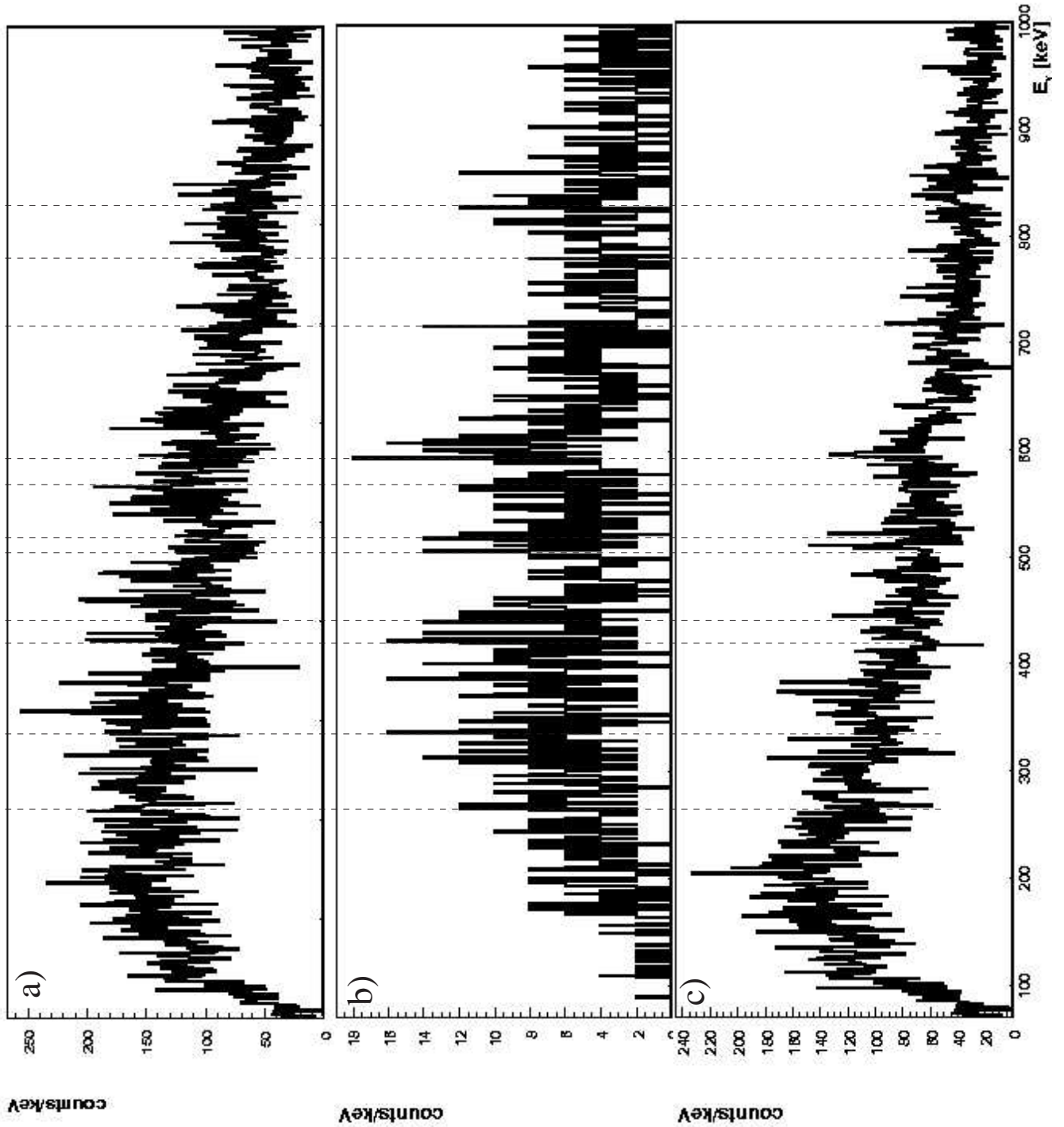


Figure 4.14: a) γ -ray spectrum following the $^{235}\text{U}(\alpha, 2n)$ reaction, obtained after gating on region B (prompt γ -rays in coincidence with delayed fission events) of Fig. 4.13. Background from neutron-induced γ rays is visible and indicated with dashed lines. Figure 4.14 b): background component obtained by taking random coincident γ -rays (Fig. 4.13 region D) and adding these to the normalised prompt fission γ -rays seen in Fig. 4.14 a). Fig. 4.14 c) Background-corrected prompt γ -ray energy spectrum following the $^{235}\text{U}(\alpha, 2n)$ reaction, obtained after gating on region B of Fig. 4.13 and subsequent normalised background correction (Region A and D of Fig. 4.13).

Chapter 5

Extraction of experimental results

Following the calibration, event building and subtraction of random background from the experimental data, a detailed analysis of the experimental findings was performed. For the two known fission isomers in ^{237}Pu half lives of $t_{1/2} = 110$ ns and $t_{1/2} = 1180$ ns, respectively, were reported [RUS71, VAN73, SPE74]. In order to verify the consistency of the present data with the published properties of the two fission isomers in ^{237}Pu , the isomeric decay curve of ^{237}Pu as displayed in Fig. 5.1 was analysed. The spectrum displays the time spectrum of fission fragments detected with respect to the α -beam pulse, exhibiting the tail of the prompt fission component extending up to $t_{frag} \approx 15$ ns, followed by a delayed component originating from a superposition of both fission isomers. An exponential fit applied to the decay curve in the delayed time region (beyond 15 ns) exhibits a half-life of 165 ns (solid line), originating from a superposition of contributions from the two fission isomers in ^{237}Pu with $t_{1/2} = 110$ ns and $1.1 \mu\text{s}$, respectively. Using a two-component fit with fixed decay constants for the two isomeric contributions (dashed and dash-dotted lines in Fig. 5.1) results in a relative intensity of $\frac{\sigma_{long}}{\sigma_{short}} \sim 10$ in agreement with literature values, where a value of $\frac{\sigma_{long}}{\sigma_{short}} = 9.7$ has been reported [VAN73].

From the fission fragment lifetimes we conclude that indeed states in the second potential minimum of ^{237}Pu were populated. Inspecting the γ -ray spectrum displayed in Fig. 4.14, we see a highly fragmented distribution of γ rays, as expected for an odd nucleus. In the following sections it will be described how the level structure of ^{237}Pu was extracted from these data (see chapters 5.2 and 6). The first step presented in the following section will be to disentangle the inclusive γ -ray energy spectrum of Fig. 4.14 into its disjunct contributions from the two fission isomers, thus enabling to build level schemes separately for each isomer and then to merge these two independent level-schemes into a common level-scheme describing the nuclear structure of ^{237}Pu .

5.1 Disentanglement of the γ spectrum

Having shown that states in the superdeformed minimum of ^{237}Pu were populated, the next task of the analysis was to separate the underlying contributions from the long-lived (high-spin) isomer from the short-lived (low-spin) isomer. In chapter 4.3 the MINIBALL Ge detector

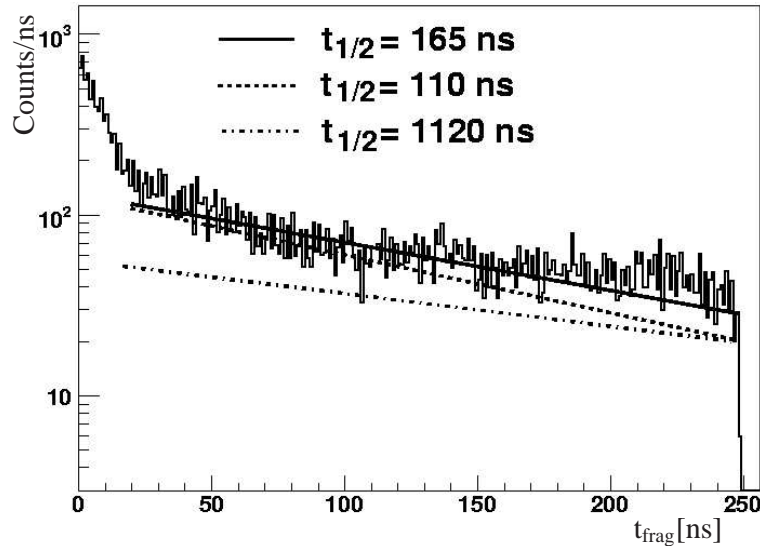


Figure 5.1: Time spectrum of fission fragments measured with respect to the prompt beam pulse. An isomeric decay curve is visible in the delayed time regime, exhibiting an integral life-time of 165 ns (solid line), consisting of a superposition of contributions from the two fission isomers in ^{237}Pu ($t_{1/2}=110$ ns and $1.1\mu\text{s}$, dashed and dashed-dotted lines, respectively). The relative intensities of the two isomeric contributions are consistent with the published isomeric population ratio $\sigma_{long} : \sigma_{short}$ [VAN73].

resolution was found to be 2.9 keV, only those transitions in Fig. 4.14 exhibiting a line width of about this value were accepted as a "real" γ transition. In this way 149 γ transitions were identified, only these γ rays were considered in the following discussion. Using the same technique as applied to measuring the overall lifetime of all fission fragments in Fig 5.1, we can gate on each of these individual γ transitions and inspect the corresponding coincident fission fragment decay curve. This results in the individual isomeric half-life connected to this specific γ transition. In this way for each γ transition the decay time for the corresponding fission fragments measured with respect to the beam pulse were analysed and tabulated. As a typical example Fig. 5.2 shows the decay curve for the 204 keV γ transition. It was found to belong to the long-lived fission isomer, since the exponential fit to fission fragment times establishes a half life of 730 (30) ns for this transition.

Table A1 (see Appendix A) lists all γ -ray transitions identified in the spectrum shown in Fig. 5.4 with a line width corresponding to the resolution of the germanium detectors. Furthermore the half-lives for the coincident fission fragments of each of the γ transitions and the number of counts in the respective peak are shown.

Following the assignment of the decay time to each of the 149 γ transitions, the resulting distribution (see Tab. A) of the half-lives has been plotted in Fig. 5.3. Two components can be distinguished, first a well-localised peak around 115 ns, which corresponds to the half-life of the short-lived fission isomer (see Fig. 5.3). 97 γ transitions contribute to this component. A second component (52 transitions) contains the remaining long-lived transitions with half-lives

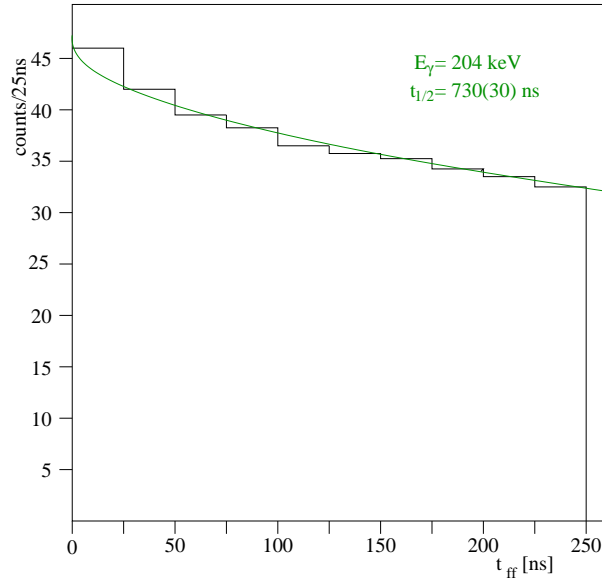


Figure 5.2: An example of an individual γ - transition half-life. Shown is the measured time difference between the beam pulse and the detected fission fragments gated on the 204 keV γ -transition. An exponential fit to the decay curve results in a half-life of 730 (30) ns, thus qualifying this transition as originating from the long-lived fission isomer.

up to $\sim 1.2 \mu\text{s}$. However, due to the limitation of the available delayed fission time window to $\approx 270 \text{ ns}$ (seen in Figure 5.1) and thus to only a fraction of the half-life of the long-lived fission isomer, an unambiguous identification of the long-lived fission isomeric component in the half-life distribution was not possible. Nevertheless, the correct population ratio between the two isomers inferred from Fig. 5.1 justifies to identify the long-lived γ transitions with the decay of the $1.1 \mu\text{s}$ isomer.

Fig. 5.4 shows again the complete energy spectrum of prompt γ rays in coincidence with delayed fission fragments as already displayed in Fig. 4.14. Marked by red arrows are those γ transitions identified as belonging to the short-lived isomer, while the green arrows indicate transitions corresponding to decays of the long-lived isomer.

5.1.1 Isomer - specific γ - ray spectra

In order to facilitate the search for rotational excitations in the γ data, the prompt γ -ray spectrum in coincidence with delayed fission fragments was disentangled into its two constituting fission isomer components. An iterative procedure was used to achieve this goal. A first γ spectrum for the short-lived isomer was generated by selecting only those short-lived γ rays in coincidence with fission fragments within $15 \text{ ns} \leq t_{frag} \leq 65 \text{ ns}$ (see Fig. 5.1). This spectrum should reliably contain predominantly contributions belonging to the short-lived isomer. In Table A we see that the γ transition at 172.8 keV is the transition with the highest intensity for the short-lived isomer. Normalising to this transition in Fig. 5.4 and subsequently subtracting the short-lived component from the inclusive spectrum results in the complementary contribu-

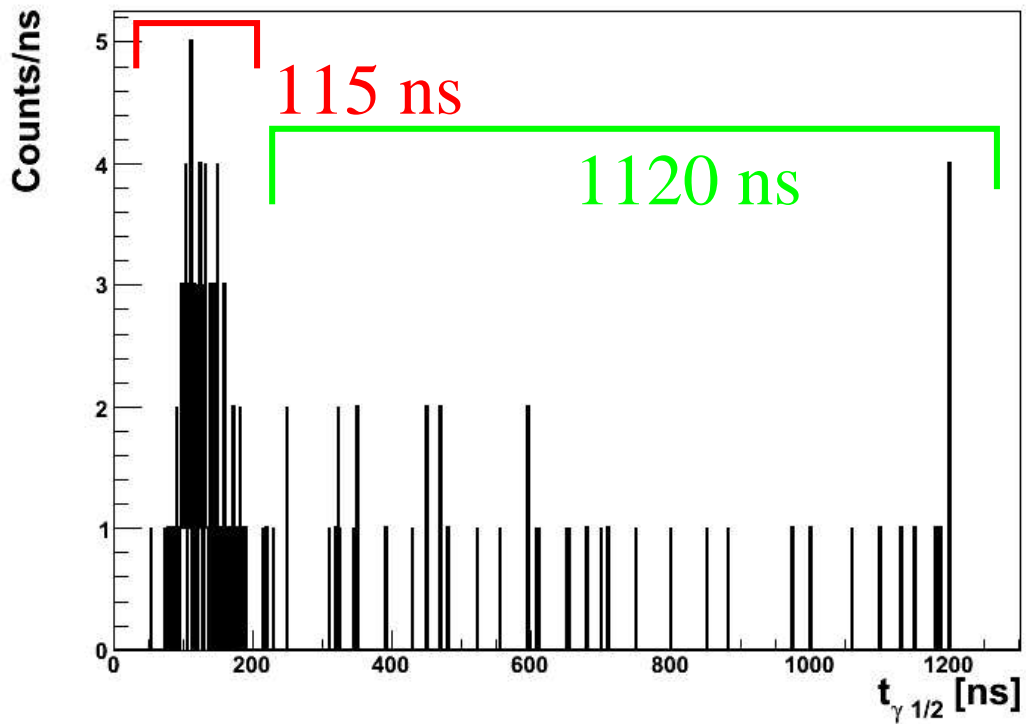


Figure 5.3: Spectrum of lifetimes for the 149 γ -transitions. A peak at $t_{1/2} = 115(15)$ ns is visible as is a collection of γ rays with halfives longer than 115 ns as predicted by the fission fragment decay curve analysed in Fig. 5.1.

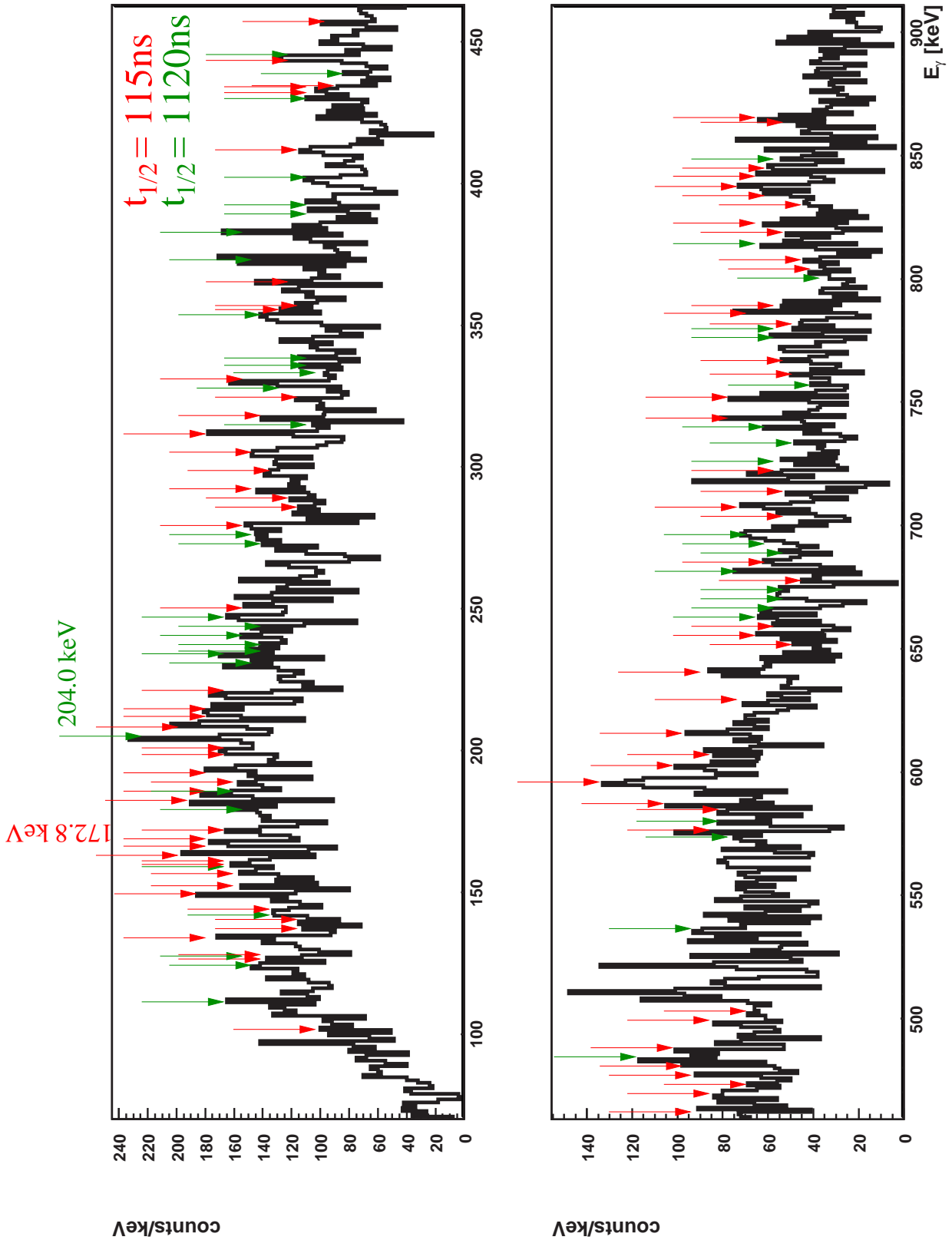


Figure 5.4: Energy spectrum of prompt γ rays in coincidence with delayed fission fragments. Indicated in red are those γ transitions which have been assigned to the short - lived isomer and in green those γ transitions belonging to the long - lived isomer.

tion from the 1120 ns isomer, potentially containing only a negligible amount of misidentified transitions belonging to the short-lived isomer. Fig. 5.5 a) shows the hereby obtained γ -ray energy spectrum belonging to the long-lived ($t_{1/2} = 1120$ ns) fission isomer. In the next iterative step the beforehand generated long-lived γ -ray component (normalised to the high intensity 204.0 keV γ transition of the spectrum in Fig. 5.4) was subtracted from the overall spectrum as shown in Fig. 5.4, thus finally resulting in the complementary contribution originating from the short-lived fission isomer. Fig. 5.5 b) displays the γ ray energy spectrum attributed to decays from the short-lived ($t_{1/2} = 115$ ns) isomer.

At first glance no immediately obvious evidence for rotational bands can be concluded from either of the two spectra in Fig. 5.5. However, with the knowledge that superdeformed shape isomers strictly follow a rigid rotor pattern, we have a tool at hand that allows to perform a rotational pattern search in the γ spectra of Fig. 5.5 as described in the following section.

5.2 Search for rotational bands

Superdeformed fission isomers are well-known to behave as rigid rotors, strictly following the rotational pattern of $E_\gamma = J(J+1)\frac{\hbar^2}{2\theta}$ and $E_{J+1} - E_J = 2(J+1)\frac{\hbar^2}{2\theta}$ (where E_γ denotes the transition energy, J the spin of the rotational band member and $\frac{\hbar^2}{2\theta}$ the rotational parameter with θ representing the rotational moment of inertia) [MET80, BET96, EIS70]. Fig. 5.6 shows the expected pattern in the γ -ray spectrum. It consists of a series of equidistant transitions with an energy difference determined by the rotational parameter (indicated in red) and a series of transitions whose difference in angular momentum can vary by $\Delta J = 1$ or 2 (indicated in blue). From previous measurements performed in the superdeformed actinide region [THI02] we know that superdeformed fission isomers strictly behave as very rigid rotors, allowing us to exploit this structural patterns as criteria in the search for excited rotational bands.

An automated rotational pattern search was conducted for each of the two isomeric γ -ray energy spectra displayed in Fig. 5.5. The γ spectra were scanned in keV steps, each time applying a peak search algorithm in order to identify γ transitions with a fixed required line width corresponding to the detector resolution (2.9 keV). These γ transitions are displayed in Table A.1, this list of transitions was then scanned for a rotational pattern of (at least 4) subsequent transitions ($E_{J+1} - E_J = 2(J+1)\frac{\hbar^2}{2\theta}$) in equidistant energy steps determined by the rotational parameter (red transitions in Fig. 5.6). In order to allow for deviations from the typical rigid rotor value of $\hbar^2/2\theta = 3.4$ keV [THI02], a variation of up to $\pm 10\%$ relative to this value was incorporated in each step of the pattern search. Furthermore it is known that the intensity of the subsequent γ transitions steadily decreases with energy within the potential rotational band. So in a first iterative step 5 equidistant γ transitions were searched with an energy spacing determined by the rotational parameter and a line width given by the germanium detector resolution. Furthermore the intensity of each subsequent peak has to be lower than that of the first identified peak.

Only those line patterns were finally accepted as a rotational band, where at least 5 transi-

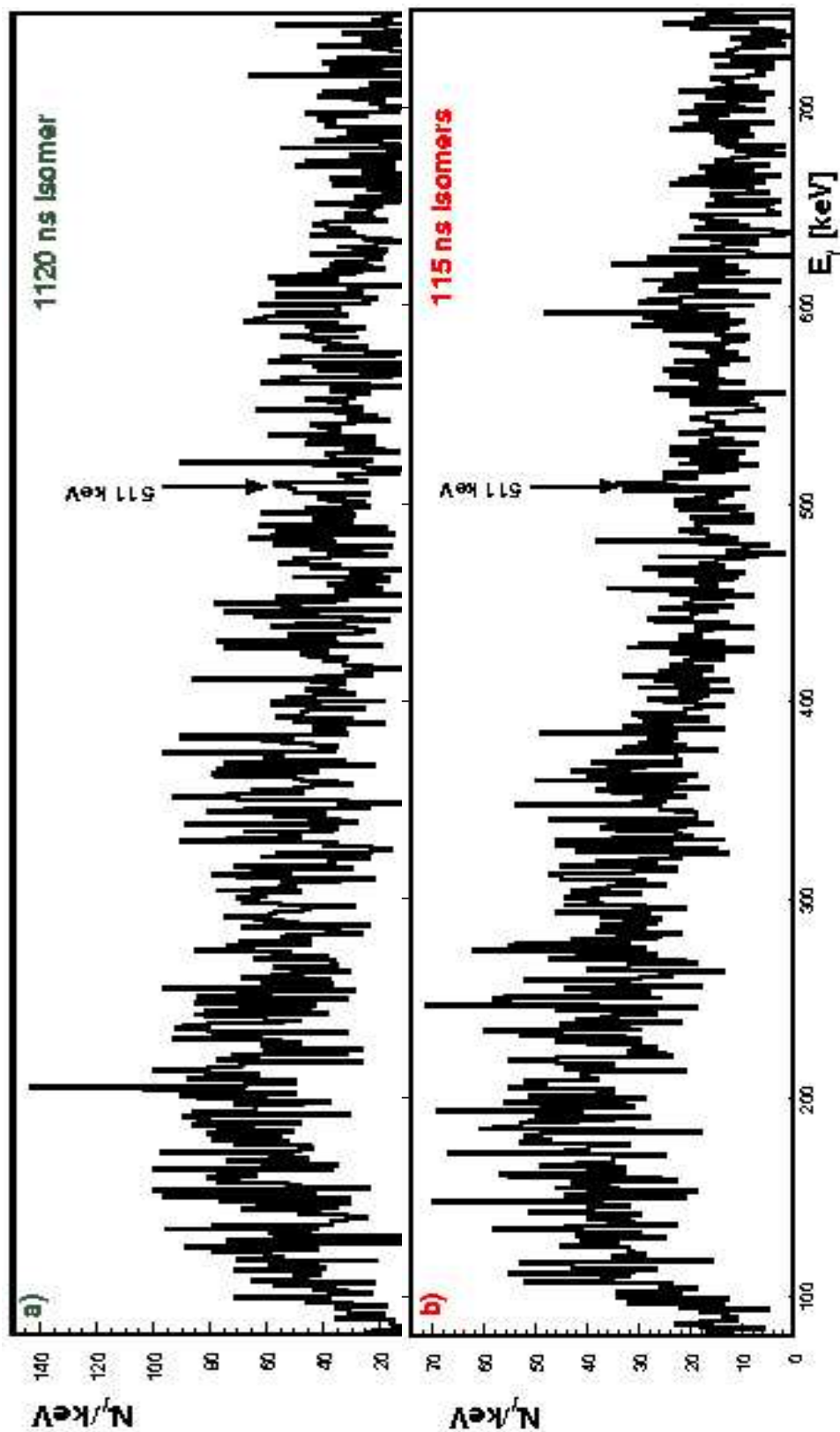


Figure 5.5: a) Energy spectrum of prompt γ -rays in coincidence with isomeric fission decay from the 1120 ns isomer. b) Energy spectrum of prompt γ -rays in coincidence with isomeric fission decay from the 115 ns isomer.

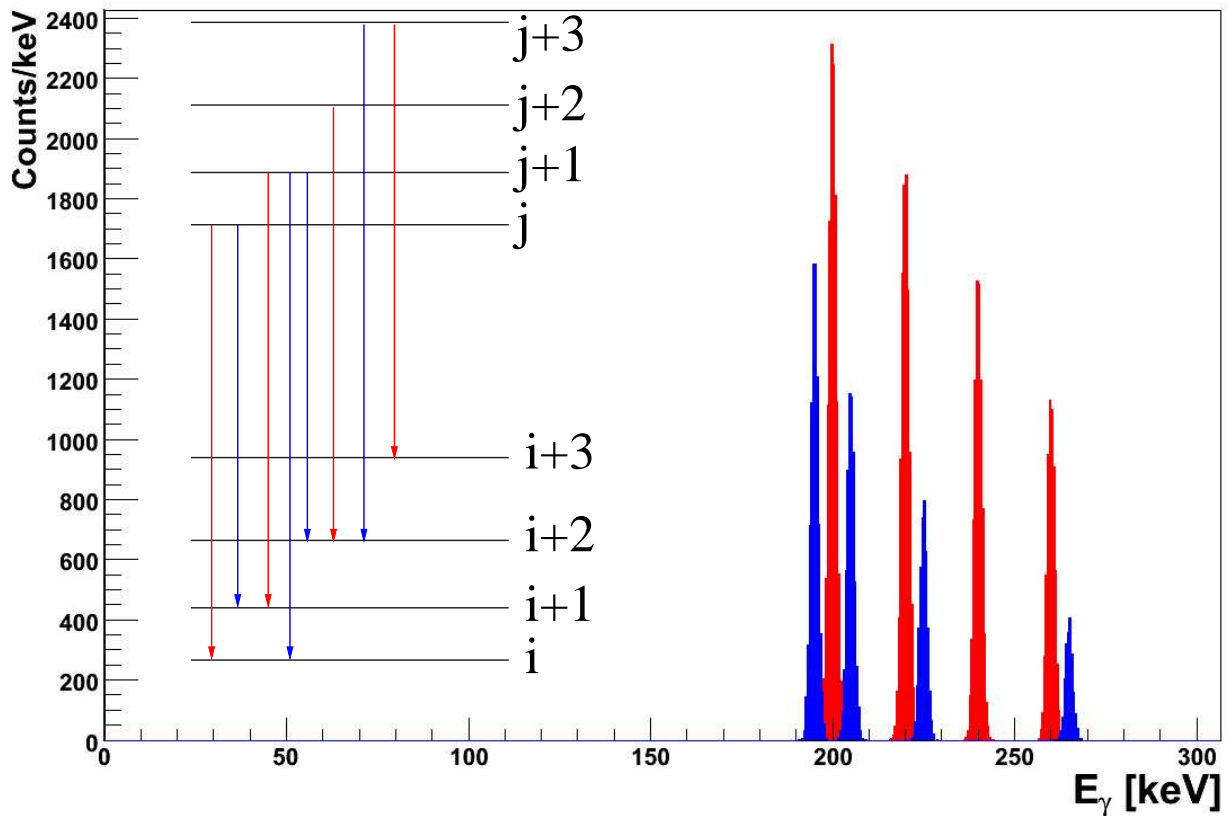


Figure 5.6: Example of a rotational γ -ray spectrum for an odd - neutron even - proton arbitrary rotational band. Indicated in red are those γ -transitions where $\Delta j = \text{const.}$ and in blue those transitions where $\Delta j \neq \text{const.}$ etc.. Also indicated is the expected level scheme for this test case.

E_γ [keV]	isomer	$\frac{\hbar^2}{2\theta}$
161.1	short	3.22 (23)
185.6	short	3.18 (16)
204.0	long	3.33 (13)
324.7	short	3.43 (22)
352.0	long	3.21 (26)
431.1	long	3.31 (10)
441.0	short	3.26 (21)
573.9	long	3.08 (18)
622.0	short	3.48 (14)

Table 5.1: Rotational bands identified in ^{237}Pu using a rotational pattern search. Indicated are the band head γ -transition energy, the rotational parameter and the assignment to the short - or long - lived isomer, respectively.

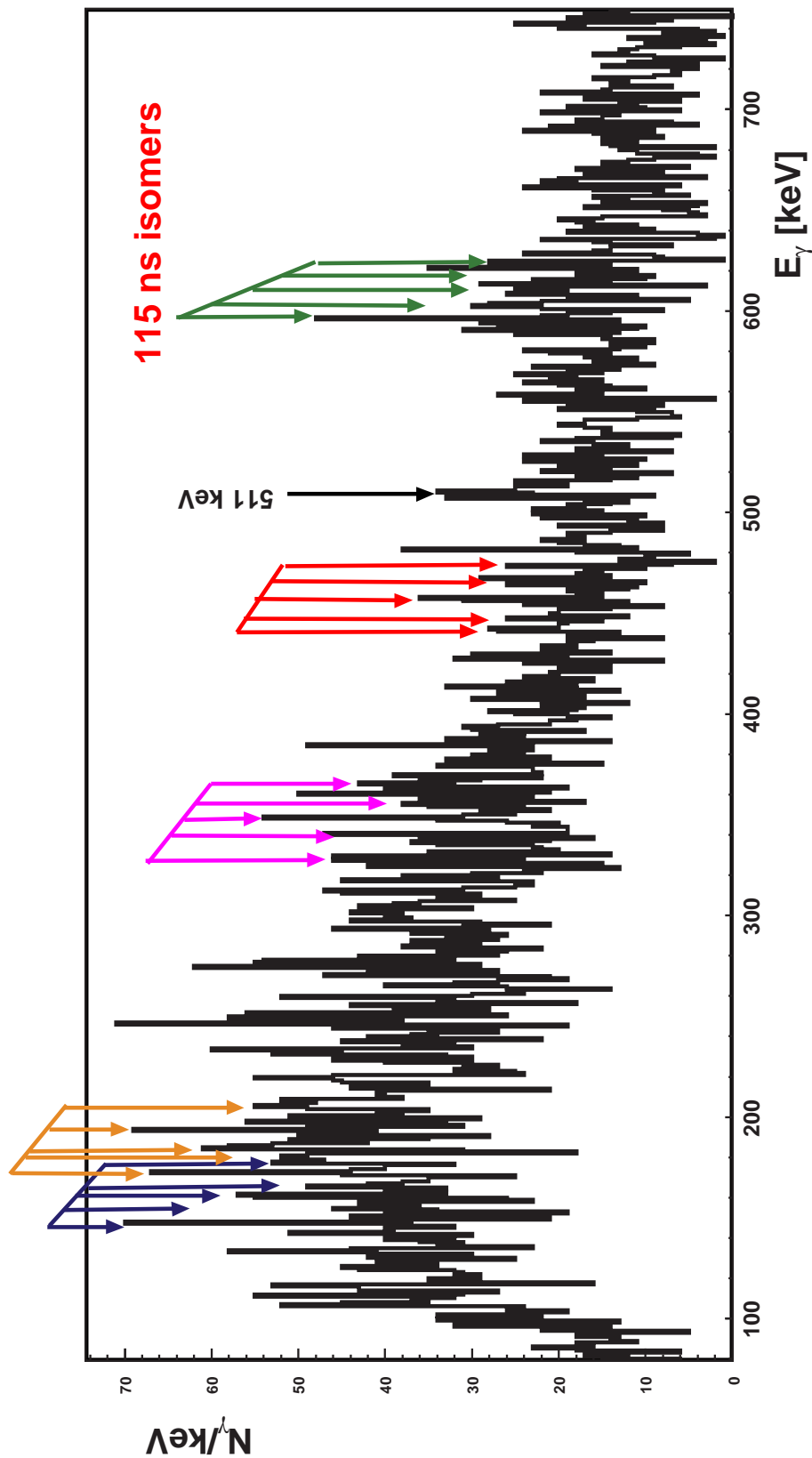


Figure 5.7: γ -ray energy spectrum in coincidence with isomeric fission decay from the 115 ns isomer with indicated rotational bands. Indicated are those 5 rotational bands that were identified by a pattern search algorithm (see text). The average corresponding rotational parameter was found to be $\hbar^2/2\theta = 3.31(22)$ keV.

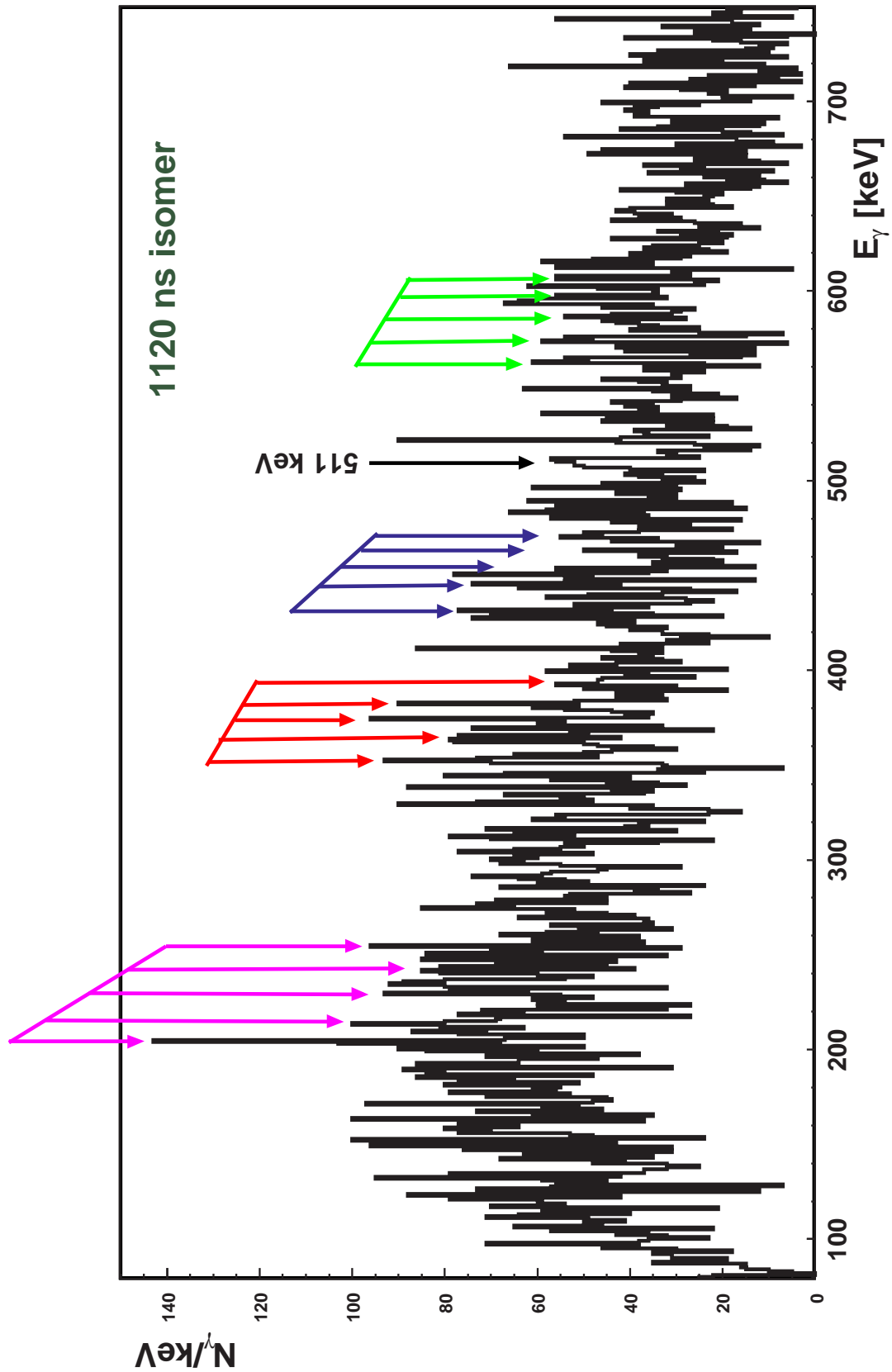


Figure 5.8: γ -ray energy spectrum in coincidence with isomeric fission decay from the 1120 ns isomer. Indicated are those 4 rotational bands, that have been identified by a pattern search algorithm (see text). The average corresponding rotational parameter was found to be $\hbar^2/2\theta = 3.23(26)$ keV.

tions could be identified fulfilling the rotational energy distance pattern with a superdeformed rotational parameter ($\hbar^2/2\theta = 3.4 \pm 0.3\text{keV}$) and where the corresponding transition intensities steadily decreased with energy within the rotational band. In total 9 rotational bands were identified for the two isomers in $^{237\text{f}}\text{Pu}$, Tab. 5.1 shows the individual rotational parameter for the nine identified rotational bands. Fig. 5.7 shows the γ -ray energy spectrum in coincidence with isomeric fission from the 115 ns isomer, indicated are the five rotational bands found here for the short-lived isomer.

Similarly for the long-lived isomer four rotational bands could be identified, as shown in Fig. 5.8. In both cases not only the equidistant transitions of spin $\Delta J = 1$ have been found, but also good candidates with spin $\Delta J = 0$ are found, used for the identification of the rotational band head spins, which will later on serve as additional valuable ingredients for the construction of a level-scheme (see chapter 6.1 for a detailed discussion on the construction of the level scheme in $^{237\text{f}}\text{Pu}$).

In a second step the rotational bands were confirmed by inspecting the corresponding $J(J + 1)$ behaviour of the "blue" transitions indicated in Fig. 5.6.

5.3 Angular distribution

Angular distributions provide a tool to distinguish between different multipolarities of γ transitions, so an attempt was conducted to apply this technique to the interpretation of our γ -ray data. A detailed discussion of angular distribution theory can be found in references [PEL82] and [STE75], in the following section only a brief introduction to the description of angular correlations is given, our experimental findings are then presented.

The γ -ray angular distributions have been parameterised in the usual way by even Legendre polynomials according to:

$$W(\Omega_\gamma) = 1 + a_2 P_2(\cos\theta_\gamma) + a_4 P_4(\cos\theta_\gamma), \quad (5.1)$$

where the angular distribution coefficients a_K describing the dipole ($K = 2$) and quadrupole ($K = 4$) contributions are defined by

$$a_K = \alpha(I_i) \cdot A_K(\gamma). \quad (5.2)$$

where A_K is the angular correlation coefficient and $\alpha(I_i)$ is the statistical tensor component. As the nuclei produced were stopped in the target with a stopping time of less than 0.1 ps, deorientation effects did not have to be considered.

The angular distribution with respect to the beam axis has been inspected for the nine band head transitions from the rotational bands identified in chapter 5.2, in an attempt to confirm the transition type from the band heads. As an example for one of the potential rotational band head transitions Fig. 5.9 shows the angular distribution of the 573.9 keV transition. However, due to the limited statistics available in the fission isomeric transition, no clear distinction between

dipole or quadrupole characteristics could be concluded. In a similar way the experimental angular distributions of the other 8 band head transitions were fitted with theoretical angular distribution curves. However, in view of the limited statistics available for these rare γ transitions it is not surprising that within error bars for none of the band heads the resulting angular coefficients allowed for an unambiguous distinction between a dipole (pure a_2) and a quadrupole transition (a_2 and a_4).

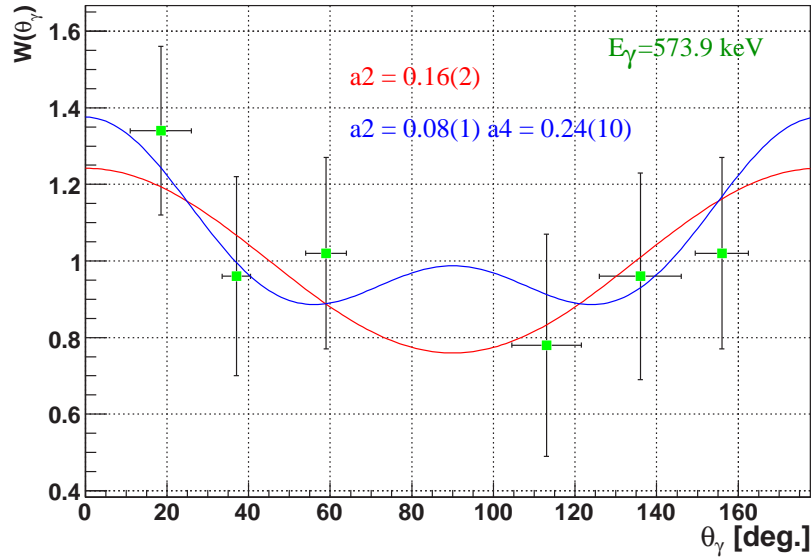


Figure 5.9: Angular distribution for the rotational band head γ transition at 573.9 keV. Shown in addition to the experimental data are the fitted theoretical angular distributions assuming pure dipole (red line) and dipole plus quadrupole (blue line) characteristics.

In the following chapter 6 a discussion of the experimental findings as presented in this chapter will be given. A level scheme for the excited states in ^{237}fPu is proposed and consequently compared to theoretical calculations within the framework of Nilsson model as well as the relativistic mean-field based Hartree-Fock-Bogoliubov (HFB) theory.

Chapter 6

Discussion of the experimental results

The spectra displayed in Figs. 5.7 and 5.8 show the suggested 9 rotational bands identified for the two isomers in $^{237\text{f}}\text{Pu}$, which may appear at first glance as a rather high density of rotational bands. Nevertheless, this number of rotational bands corresponds to what has also been found in the first minimum of other actinide isotopes. Fig. 6.1 shows the rotational bands built on the ground-state band of the first minimum of ^{237}Pu . Eight excited rotational bands have been identified in ^{237}Pu below an excitation energy of 1 MeV [FIR96]. Similar numbers of rotational bands are known for the odd - neutron, even - proton nuclei around ^{237}Pu as listed in Table 6.1.

Furthermore we can compare the moments of inertia of the rotational bands in the first minimum to those in the superdeformed second minimum of ^{237}Pu . Fig. 6.2 displays the moments of inertia of rotational bands in the first and second minimum in ^{237}Pu , ^{239}Pu , ^{240}Pu , ^{241}Pu and ^{243}Pu (open symbols for the second minimum and full symbols for the first minimum) as a function of the excitation energy (where the excitation energy of the second minimum is set to 0). It can be seen that the spin-dependent moments of inertia for rotational bands derived in $^{237\text{f}}\text{Pu}$, similar to those in $^{240\text{f}}\text{Pu}$, show a clear trend towards the superdeformed rigid rotor

Isotope	rotational bands
$^{237\text{f}}\text{Pu}$	9
^{237}Pu	9
^{237}U	11
^{239}U	12
^{239}Pu	6
^{241}Pu	7
^{243}Pu	11

Table 6.1: Number of rotational bands identified for the odd - neutron, even - proton nuclei around ^{237}Pu below an excitation energy of 1 MeV [FIR96].

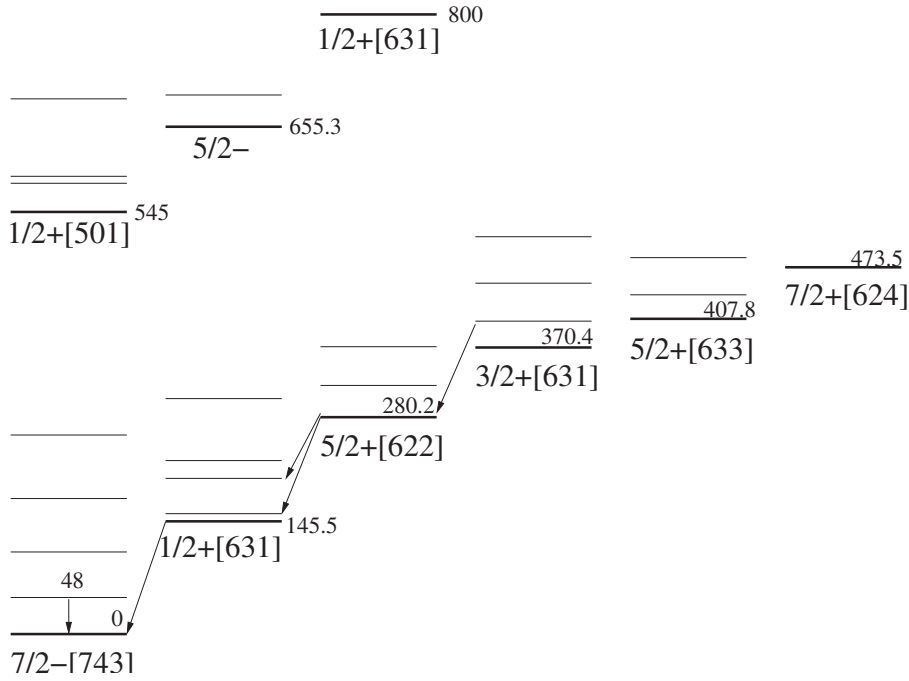


Figure 6.1: Rotational bands in the first minimum of ^{237}Pu , taken from [NNDC].

limit (indicated by the blue dashed line in Fig. 6.2).

6.1 Construction of fission - isomeric level schemes

Following the identification of rotational bands, level schemes, for both isomers, could be derived using a Ritz combinatorial technique [EGI07]. The Ritz combinatorial principle is an empirical approach that uses sums and differences of transition energies in order to construct level schemes for nuclei whose excitation spectra are highly fragmented and complex. The Ritz combinatorial program used here to build the level schemes for ^{237}fPu was provided by T. von Egidy [EGI07]. The program requests that any known information on the level structure be implemented along with the γ transitions identified as belonging to the nucleus of interest (including the transition intensities). The γ transitions are then compared to the known level structure and by addition and subtraction the construction of a consistent level scheme is attempted. The program then returns a list of suggested levels and transitions built on the input transitions and levels.

In a first step isomeric ground - state bands were constructed assuming a rigid - rotor pattern of the rotational band members for a superdeformed rotational parameter of $\hbar^2/2\theta \approx 3.4$ keV. From the previously published data on ^{237}fPu the ground - state spins of the two isomers could not be unambiguously concluded, leaving the alternative of $J = 3/2$ and $J = 5/2$ for the short - lived isomer and $J = 9/2$ and $J = 11/2$ for the long - lived isomer, respectively [SPE74, RUS71, VAN73, GUEN79, RAF83]. For this reason level schemes with alternative tentative assignments for a ground state spin of $3/2$ and $5/2$ for the short - lived 115 ns isomer and $9/2$ and $11/2$ for the long - lived 1120 ns isomer, respectively, were constructed. As the isomers preferably deexcite

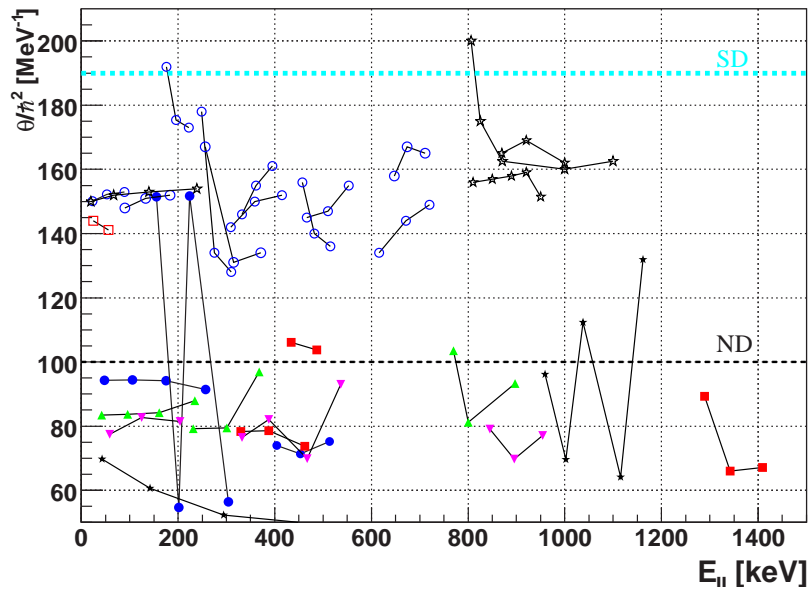


Figure 6.2: Moments of inertia of rotational bands in ^{237}Pu (circle), ^{239}Pu (square), ^{240}Pu (stars), ^{241}Pu (triangle) and ^{243}Pu (inverted triangle). Open symbols have been used for the second minimum, while full symbols denote rotational bands in the first minimum as a function of the excitation energy with respect to the ground state (the ground state excitation energy in the second minimum has been set to zero). The spin-dependent moments of inertia for the rotational bands derived in ^{237}fPu exhibit a clear trend towards the SD rigid rotor value. All moments of inertia besides ^{237}fPu are derived from the data shown in [FIR96]. The light blue dashed line represents the superdeformed rigid rotor limit (SD), while the black dashed line represents the normally deformed rotor (ND).

via in-band transitions to their respective ground states, from which they are depopulated into the ground-state rotational band, the ground state decays of the rotational band heads should exhibit the largest decay intensities. This feature was indeed identified in the isomeric γ spectra.

Moreover, rotational band members not only deexcite via in-band transitions within the rotational band to the band head, they also deexcite via inter-band γ transitions into lower-lying rotational bands. We can use these inter-band γ -ray transitions to allow for an identification of the band head spin J of the rotational band. Therefore, in a second analysis step the nine rotational band heads identified in chapter 5.2 were implemented into the Ritz algorithm as known levels without a spin assignment, in order to identify their corresponding inter-band transitions. Only those transitions whose energies were within 0.2 keV of the predicted level distances were accepted by the Ritz algorithm. Applying these conditions, level schemes for both the short-lived and the long-lived isomer could be constructed.

For the two alternative ground-state spin scenarios of the short-lived 115 ns isomer, the starting conditions to the Ritz program therefore consisted of either a ground state band with spin $J=3/2$ or $J=5/2$ together with 5 excited rotational bands, with given level positions. However, the individual band head spins had yet to be confirmed. In a first iteration, the most probable excitation energies of the ground state rotational band were searched for. For a ground state rotational band with spin $J=3/2$ only 4 transitions with a deviation of less than 0.5 keV from the expected level distances were found, while on the other hand for a ground state rotational band with a band head spin of $J=5/2$ 72 transitions between levels with a deviation from the expected level distance of less than or equal to 0.1 keV were found.

Fig. 6.3 shows the level scheme deduced for the 115 ns isomer in ^{237}Pu . Applying the Ritz combinatorial technique it could be concluded that the ground-state spin of the short-lived isomer is $J=5/2$, as no transitions to a potential $J=3/2$ ground state could be observed.

In a similar way the level scheme could be derived for the 1120 ns isomer as displayed in Fig. 6.4. It was found that a $J=9/2$ ground state described the long-lived isomer best. In both level schemes we observe that the transitions from the excited rotational band heads have the highest intensity of all ground-state transitions of the rotational band members as expected. Fig. 6.5 shows the γ ray spectra for the two isomers, where those γ transitions are indicated which have been used to construct the level-schemes. From the 149 transitions identified (see Fig. 5.4 and Tab A.1), 143 were implemented into the level-schemes (Table A.2 and A.3 respectively for the short-lived and the long-lived isomer). The six γ transitions not implemented all lie above 630 keV, here the before mentioned peak correlation techniques (see Chapter 5.2) and Ritz combinatorial techniques were not able to identify a possible rotational band built above this energy. This does not mean that there are no rotational bands above 630 keV, however, these have so far not been experimentally identified.

While the relative energetic position of the short- and long-lived isomeric band heads previously was known only with a very large error margin to 300 ± 150 keV, our detailed γ -ray spectroscopy allows to search for a decay pattern that links the long-lived, high-spin isomer to the short-lived, low-spin fission isomer. The fact of the mere existence of a long-lived fission

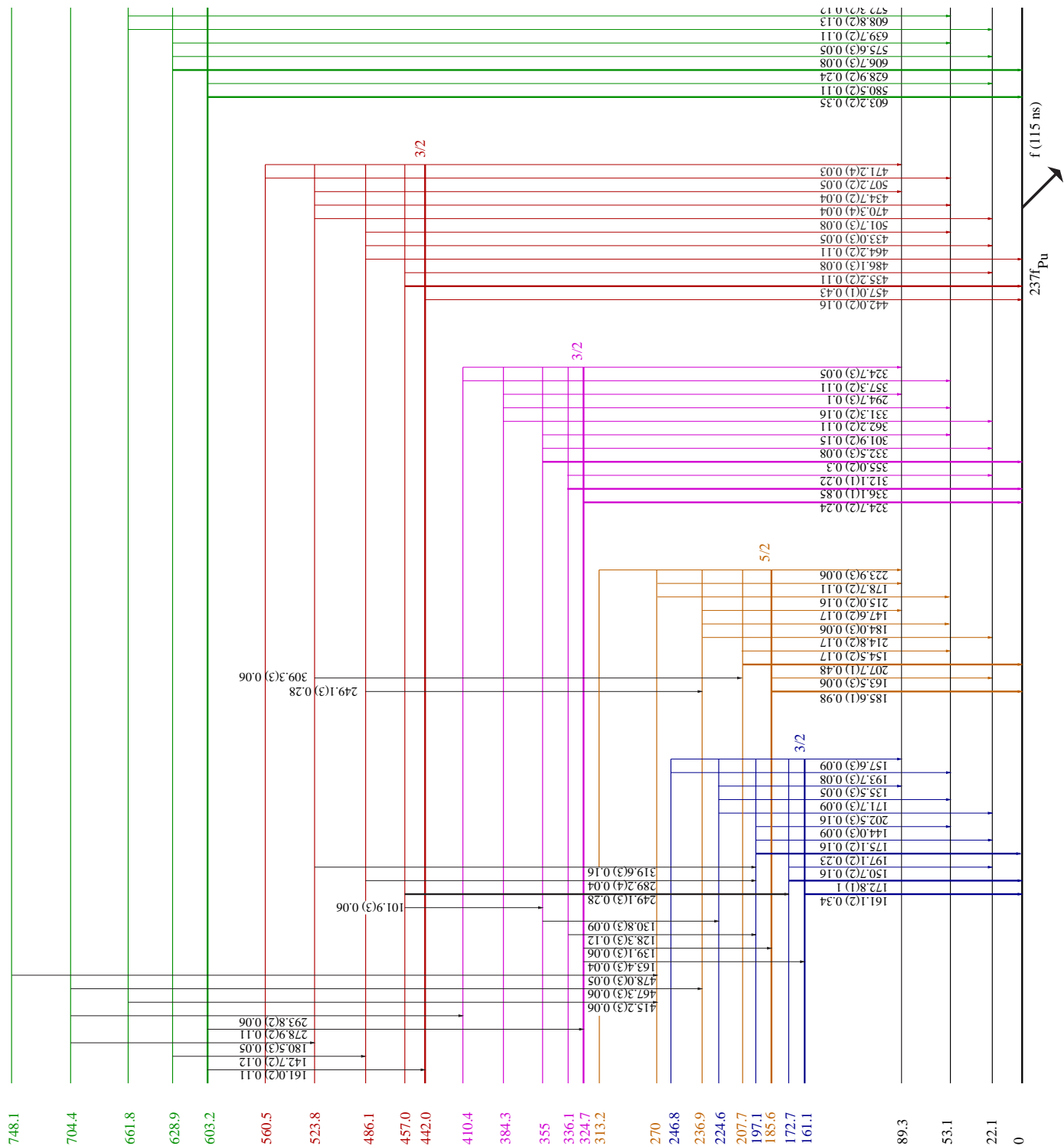


Figure 6.3: The decay scheme deduced for the 115 ns isomer in ^{237}fPu . The ground-state spin of the low-spin isomer was found to be $J = 5/2$, as no transitions to a potential $3/2$ or $7/2$ ground state were observed. The colour code refers to the identification of rotational bands as displayed in Fig. 5.7. Table A.2 in Appendix A shows the table of γ -ray transitions used to construct this level-scheme. Those transitions whose intensities are greater than 23% are indicated with thick lines.

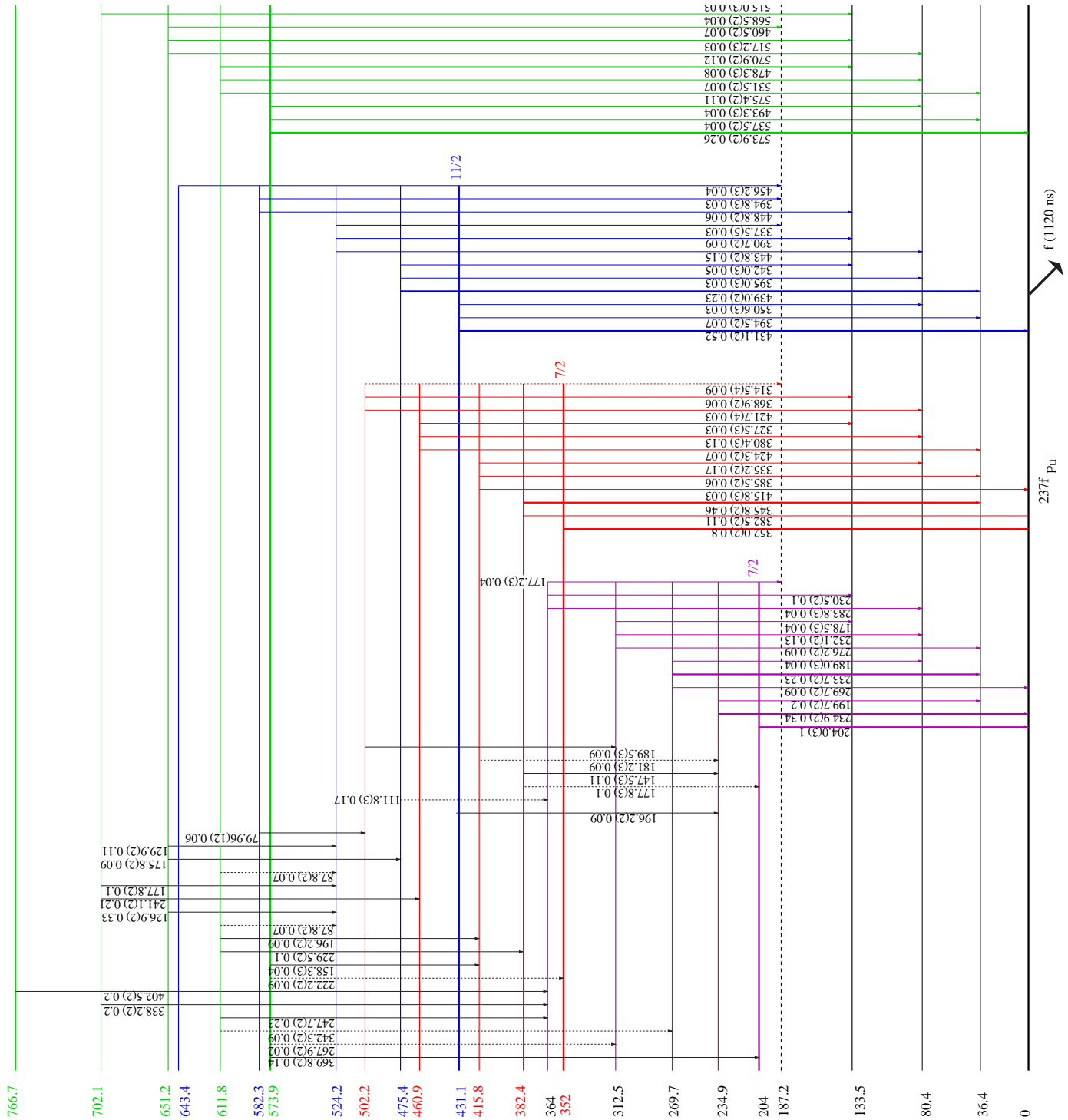


Figure 6.4: The decay scheme deduced for the 1120 ns isomer in ^{237}fPu . The ground-state spin of the high-spin isomer was deduced to be $J = 9/2$, as no transitions to a potential $7/2$ or $11/2$ ground state have been observed. The colour code refers to the identification of rotational bands as displayed in Fig. 5.8. Solid lines indicate connecting transitions between excited bands with deviations of the measured transition energies with respect to the expected level distances derived from the Ritz combinatorial analysis of up to 0.1 keV, while the dashed lines represent transitions with deviations of up to 0.2 keV. Table A.3 in Appendix A shows the table of γ -ray transitions used to construct this level-scheme. Those transitions whose intensities are greater than 23% are indicated with thick lines.

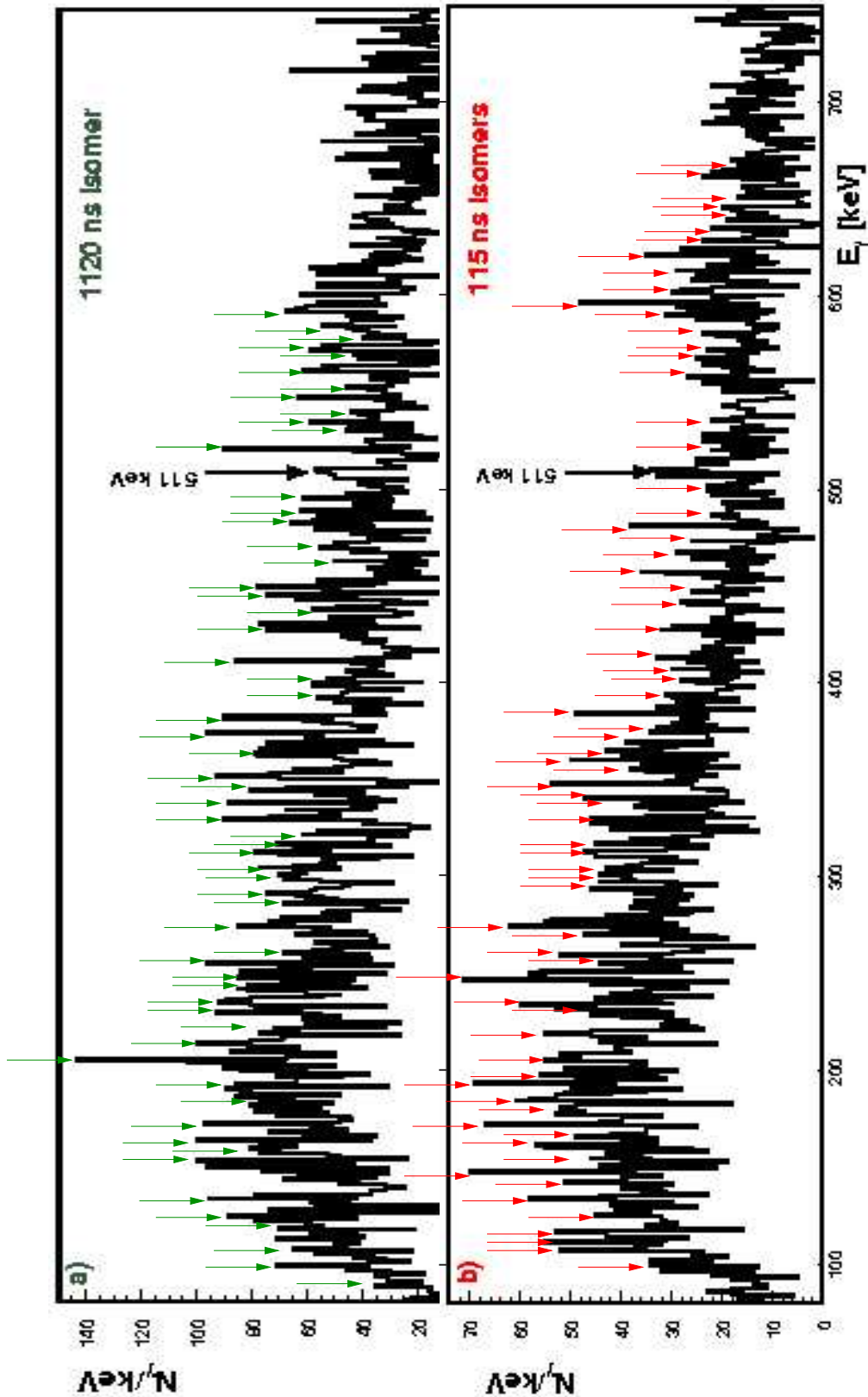


Figure 6.5: a) Energy spectrum of prompt γ -rays in coincidence with isomeric fission decay from the 1120 ns isomer. b) Energy spectrum of prompt γ -rays in coincidence with isomeric fission decay from the 115 ns isomer. Indicated in both spectra are those γ transitions which have been implemented into the deduced level-schemes (See Tables A.2 and A.3 in Appendix A).

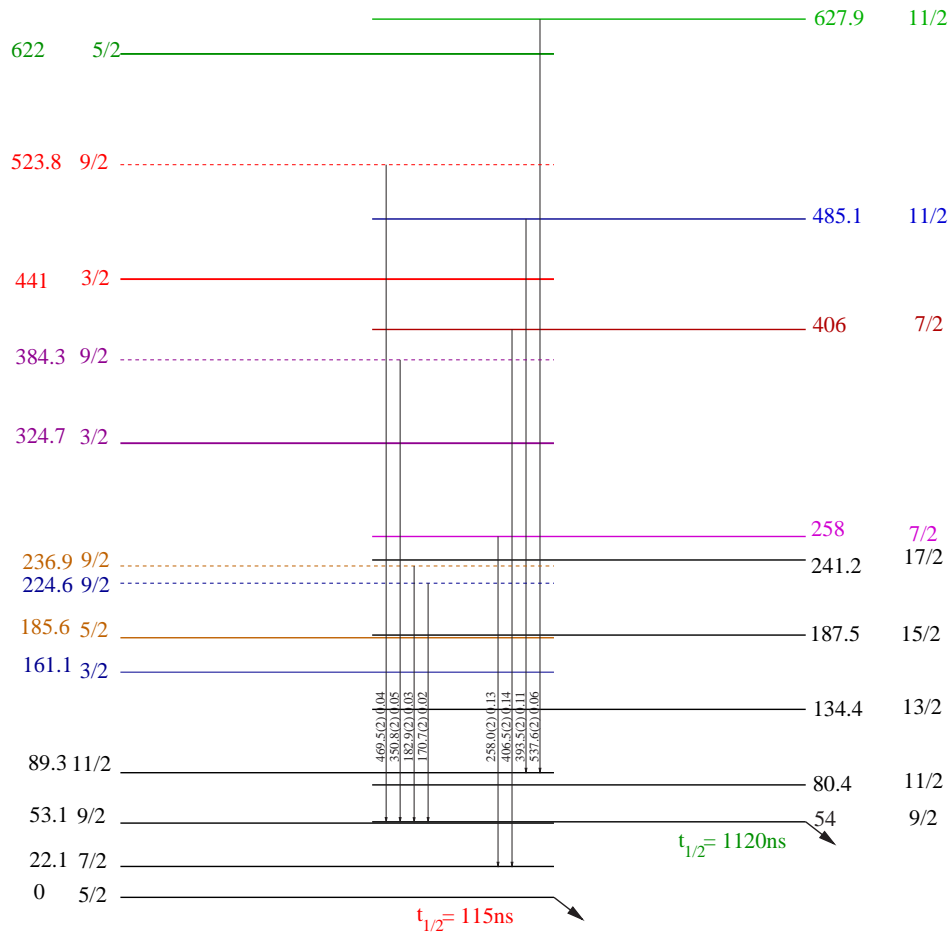


Figure 6.6: Level scheme of the second minimum of ^{237}Pu , combining the rotational band structure included in Figs. 6.3 and 6.4. Indicated are linking transitions between the two isomers, pinpointing the excitation energy for the ground-state of the high-spin isomer to 54 keV.

isomer with a ground state spin of $J = 9/2$ points to an excitation energy not too far above the $9/2$ state of the low-spin isomer, otherwise fission would be hindered by a strong direct γ -decay branch. Indeed our γ -ray spectrum reveals a series of 4 transitions linking the band heads of the $1.12\ \mu\text{s}$ isomer to the ground-state rotational band for an excitation energy of the $9/2$ isomeric ground state of 54(2) keV. Moreover, 4 transitions can be found depopulating the rotational bands of the low-spin isomer into the ground state of the high-spin isomer. It is rather this interwoven consistent network of linking transitions than the obviously limited statistical relevance of the individual transitions that endorses the credibility of this new single-particle picture in the second minimum.

A limitation for the possibility of spin assignments applies for $J = 1/2$ bands. The reason behind this is given by the Coriolis force. The rotational motion in odd- A nuclei is influenced by the presence of the last valence nucleon. This coupling effect provides further evidence on the one-particle motion in deformed nuclei; moreover, it constitutes a link between the motion

of the individual particles and the collective rotation of the nucleus as a whole [BOM75]. The effect of the Coriolis force is that for $K = 1/2$ bands the level order of the rotational band can be inverted for large decoupling parameters [EIS70]. The rotational energy of a state is given by;

$$E_{rot} = \frac{\hbar^2}{2\theta} (J(J+1) + a(-1)^{J+1/2}(J+1/2)\delta(K, 1/2)), \quad (6.1)$$

where

$$a = \sum_j (-1)^{j-\frac{1}{2}} (j + \frac{1}{2}) |C_{j\frac{1}{2}}^{(a)}|^2, \quad (6.2)$$

is the so called decoupling parameter. For $K = 1/2$, the rotational energy (of eq.6.1) is, apart from a constant, proportional to $(J + (1 + \sigma a)/2)^2$, where $\sigma = (-1)^{J+1/2}$ is the signature. Thus, the branches with different signatures have energy parabolas displaced in opposite directions along the J -axis. When the decoupling parameter a is numerically larger than unity, these displacements lead to an inversion of the normal spin sequence [BOM75, EIS70]. For bands with $K \neq 1/2$, $a = 0$ and the rotational bands behave according to the known rotational pattern of $E_{rot} = \frac{\hbar^2}{2\theta} (J(J+1))$. To identify $J=1/2$ bands it is necessary to have a theoretical calculation not only able to reproduce the single-particle states identified here but also giving a value of the decoupling parameter for the suggested $J=1/2$ bands and to search for these in the γ spectrum. A comparison to theoretically predicted single-particle states will be given in section 6.3.

6.2 Lifetime considerations

With the spectroscopic information contained in Fig. 6.6 conclusions can also be drawn on the lifetimes of specific states, exploiting the knowledge from neighbouring nuclei. In the neighbouring odd- N isotope ^{239}Pu similar to ^{237}Pu a double isomer has been identified. However, in contrast to ^{237}Pu with its two fission isomers, the 2.6 ns isomer sitting on top of the $8\mu\text{s}$ fission isomer is a spin isomer. The decay scheme of this isomer was studied by Backe et al. via conversion electron spectroscopy [BAC79], resulting in the proposed level scheme depicted in Fig. 6.7.

The 2.6 ns spin isomer decays with a branch of 41 % into the $7/2^{(+)}$ state on top of the $5/2^{(+)}$ fission isomeric ground state. Therefore the partial γ lifetime of the isomer amounts to $2.6\text{ ns}/0.41 \approx 6.34\text{ ns}$. Scaling this partial lifetime with the E_γ^3 dependence of the γ transition energies (178.7 keV for the E1 transition $9/2^{(-)} \rightarrow 7/2^{(+)}$ in ^{239}Pu compared to 31.9 keV for the $9/2 \rightarrow 7/2$ transition in ^{237}Pu) results in a partial fission lifetime for the isomeric $9/2$ ground state of 1115 ns. In the investigation of ^{239}Pu the lifetime was explained due to a large K-hindrance [BAC79]. Furthermore, Specht et al. measured the fission fragment angular anisotropies of the

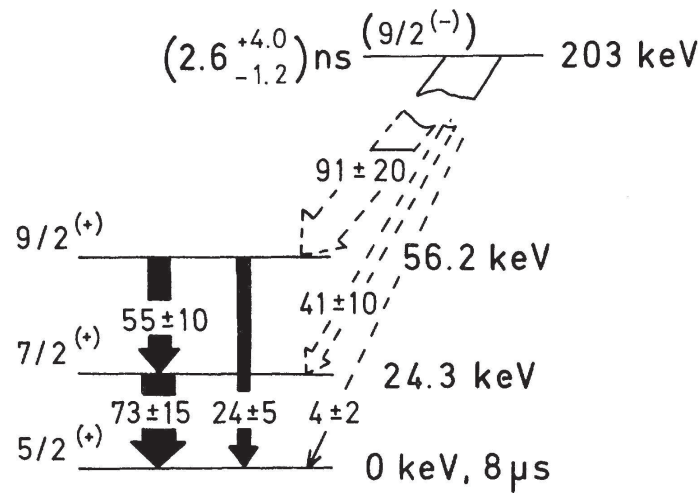


Figure 6.7: Proposed decay scheme of the 2.6 ns isomer in ^{239}fPu as measured by Backe et al. [BAC79]. The intensities of the feeding transitions are corrected for internal conversion, assuming multiplicities of E1(147, 179 keV) and M2 (203 keV). The positive parity of the 5/2 state was suggested by comparison with theory, as no $5/2^-$ state is predicted near the Fermi surface [BAC79].

two isomers in ^{237}Pu and found for the long-lived isomer an anisotropy $W(\theta)/W(90^\circ)$ ($\theta = 13^\circ$ and 55°) 1.41(14) and for the short-lived isomer an anisotropy of 0.58(16) was obtained [SPE74]. Already the fact of a difference in the anisotropy of the two fission isomers allowed for the conclusion that the higher-lying $1.1 \mu\text{s}$ isomer predominantly decays via fission rather than by electromagnetic transitions to the short-lived isomer. Thus the γ decay time within the second minimum must be much larger than the measured fission half-life of 1120 ns, otherwise the observed half life would be closer to 560 ns, in ^{237}fPu the K-hindrance must therefore be larger than in ^{239}fPu .

A second conclusion can be drawn from the rotational band structure in the second minimum of ^{237}Pu . Inspecting the level scheme in ^{237}fPu with its rather large density of rotational bands below 800 keV excitation energy in the second minimum, a coupling between the $I = 5/2$ band at 603 keV and the $I = 11/2$ band at 627.9 keV to the octupole vibration of the ground state band could occur. This collective mode ($K^\pi = 0^-$) has been identified at 554.7 keV in the neighbouring fission isomer of ^{240}Pu . In addition, from the plunger-measurements of the $B(E2)$ value of ^{240}Pu [SPE72] we know that the converted low-energy transitions have a typical lifetime of 2-3 ps. Although we do not know the side-feeding intensities, from the ratio of intensities between inter-band transitions depopulating the band head and the in-band rotational transitions we can derive a lifetime of the ground state transition with respect to the converted transition. This way a lifetime of $\geq 10 \text{ ps}$ for the $5/2 \rightarrow 5/2$ transition at 622 keV in the short-lived isomer can be inferred.

6.3 Comparison to theoretical single-particle level schemes

Having established an experimental level scheme for ^{237}Pu , an attempt can be made to identify single-particle orbits by comparing with theoretical predictions. For this purpose the experimental findings were compared to three different sets of calculations, the first one performed, already 30 years ago, by Hamamoto and Ogle using a deformed Woods-Saxon potential [HAM75] (see chapter 6.3.1), a second one using the deformed oscillator potential of the Nilsson model taken from [DAO07] and [NIL69] (see chapter 2.2), and finally a comparison to a modern mean field theory, the relativistic Hartree-Fock Bogoliubov (HFB) theory performed by Ring et al. [DAO07] (see chapter 2.4).

6.3.1 Early Woods-Saxon-type calculation

In the study of ^{239}Pu (Fig. 6.7) low-lying excited rotational states on top of a $8\mu\text{s}$ fission isomer, fed by a higher-lying 2.6 ns spin isomer had been identified by Backe et al. [BAC79]. For the ground state of the $8\mu\text{s}$ isomer a spin and parity of $5/2^+$ was suggested, while for the 2.6 ns spin isomer a ground state spin of $9/2^-$ emerged. Comparing these values to the then available theories, it was found that the only state close to the Fermi surface for ^{239}Pu is the [633] $5/2^+$ state with $\Lambda=3$ and $K=5/2$, as predicted by the calculations of Hamamoto and Ogle [HAM75]. In these calculations the single-particle Hamiltonian was diagonalised with a deformed Woods-Saxon-potential in a large basis of harmonic oscillator wave functions. The spin-orbit force was increased by 20% compared to standard parameters. This increase of the spin-orbit force was neglected by most theories due to the lack of experimental information at large deformations.

The calculations performed by Hamamoto and Ogle investigated the single-particle level scheme using the deformed Woods-Saxon potential of Ehrling and Wahlborn [EHR72] with values for the quadrupole and hexadecupole deformation in the spherical harmonic expansion of $\beta_2 \approx 0.66$ and $\beta_4 \sim 0.06$, respectively. At the time there was no spectroscopic information available other than lifetime [VAN73, RUS71] and g-factor measurements [KAL74] of ^{237}Pu , however earlier shell structure calculations [BOH69] already indicated that the second potential minimum corresponds to a deformation of $\beta_2 \approx 0.6$. By varying the single-particle potential parameters within a reasonable range, Hamamoto and Ogle searched for two isomeric states which were consistent with the then available experimental information.

Fig. 6.8 shows the single-neutron energy levels as calculated by Hamamoto and Ogle. The calculations predict a $5/2^+$ [862] state close to or at the Fermi surface. However, for $\beta_2 \sim 0.6$ and $\beta_2 \sim 0.65$ magic neutron numbers 142 and 148, respectively, were predicted. These findings were in contrast to measurements performed by Metag et al. [MET74], which indicated already then that the magic neutron number for superdeformed fission isomers should be $N=146$. Therefore these early calculations proved insufficient to explain even basic experimental properties.

However, as computer performance has increased drastically in the past 30 years, nowadays systematic parameter studies can easily be performed. Therefore a deformed Woods-Saxon

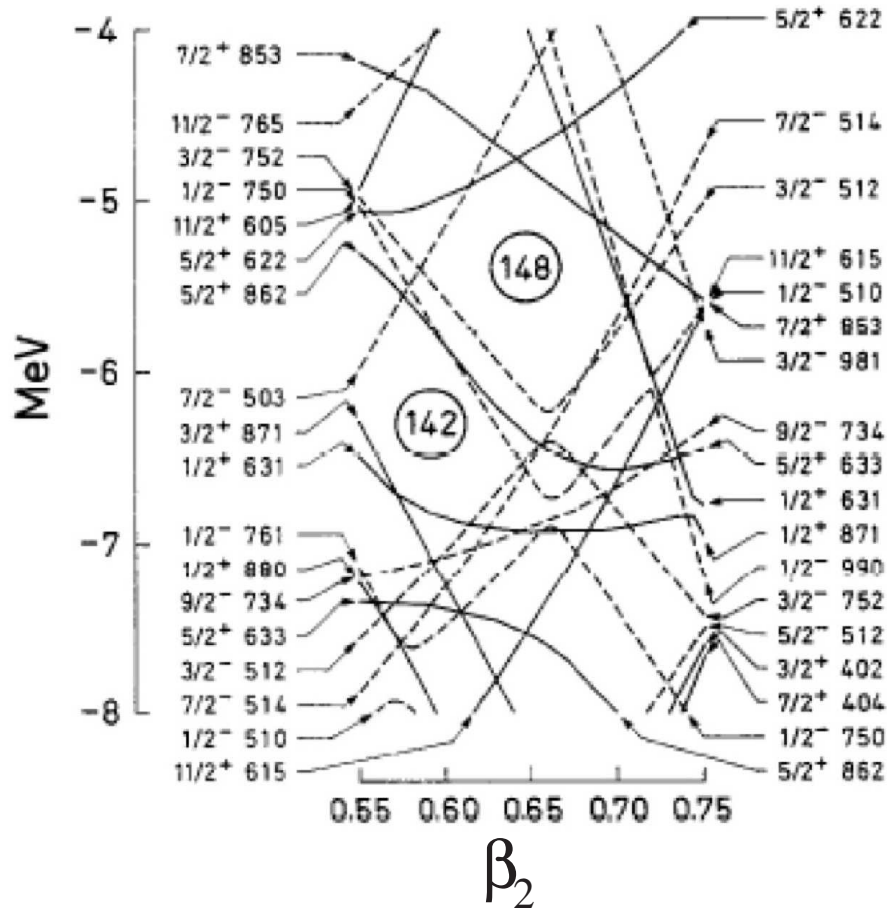


Figure 6.8: Single-neutron energies as a function of the nuclear deformation β_2 for a deformed Woods-Saxon potential for ^{237}Pu [HAM75].

code was obtained from Dudek et al. [LOJ98], in order to vary the Woods-Saxon parameters for a comparison with experimental findings. Fig. 6.9 shows the single-neutron energies for $\beta_2 = 0.58$ and a constant $\beta_4 = 0.08$. For the first time in such calculations the correct value for the deformed magic neutron number of $N = 146$ could be reproduced. In these calculations the spin-orbit force that had been increased by Hamamoto and Ogle [HAM75] by 20% was only increased by 17% relative to the standard parameters.

In addition the calculation shown in Fig. 6.9 also reproduces our experimental findings for the isomeric ground state with $J = 5/2^+$ [862] and $J = 9/2^-$ [734], respectively. Unfortunately besides the two $J = 3/2$ states predicted above the ground state no further single-particle levels were found in the calculation that could be correlated with any of our experimental findings. Indicated in red is the $J = 1/2$ band proposed by the Woods-Saxon calculation. Due to the Coriolis force, this band may decouple from this position and either be shifted in energy or couple to close-lying bands, altering their spin values, thereby resulting in either of the experimentally found excited $J = 7/2$ or $J = 11/2$ bands.

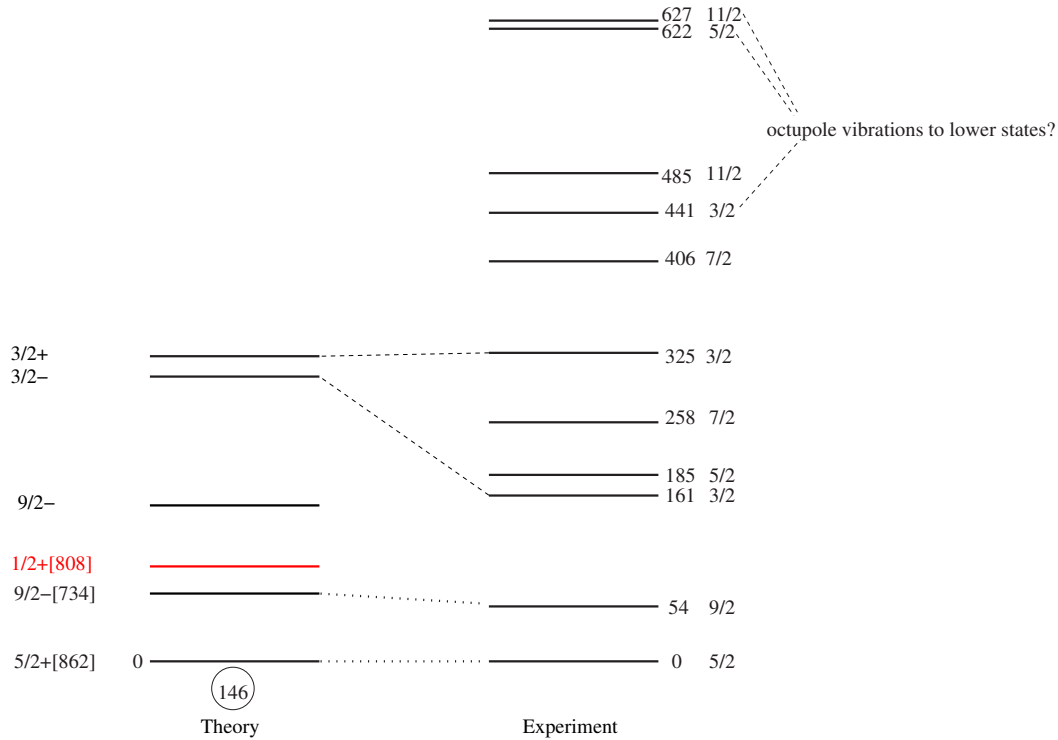


Figure 6.9: Single-particle levels from Woods-Saxon calculations in ^{237}Pu [DAO07] compared to the experimental findings presented in Chap. 6.1 for $\beta_2 = 0.58$. Indicated in red is the $J = 1/2$ band proposed by the Woods-Saxon calculation. Due to the Coriolis force, this band may decouple from this position and either be shifted in energy or couple to close-lying bands, altering their spin values. Also indicated are possible (experimental) candidates for an octupole coupling to lower states.

6.3.2 Comparison of experimental results to Nilsson calculations

The Nilsson model calculates nuclear energy surfaces as a function of deformation on the basis of a modified oscillator potential [NIL69] as described in chapter 2.2. In particular quadrupole and hexadecupole deformations are considered. The behaviour of the energy surface is normalised to that of a liquid drop using a generalised Strutinsky prescription. Furthermore single-particle energies can be extracted, the energy at the Fermi surface is predicted using five parameters (see Eq. 2.12), the neutron number, the quadrupole and hexadecupole deformation ($\beta_2 \sim P_2$ and $\beta_4 \sim P_4$, respectively) and two shell parameters κ and μ in the single-particle Hamiltonian $H_{s.p.}$. In a series of calculations, κ , μ , β_4 and β_2 , (see Figs. 6.10, 6.11 and 6.13, respectively) were varied to reproduce the experimental findings of the (deformed) magic neutron number $N = 146$ and an $I = 5/2$ state at the Fermi surface.

From the measurements performed by Metag et al. [MET74] the deformed neutron shell closure for superdeformed isomers was deduced to be located at $N = 146$. In all of the early theoretical calculations [HAM75, MOS71, NIL69, PAU73], the magic neutron number varied between 142 and 148, while none of them succeeded to reproduce $N = 146$. Hamamoto and Ogle

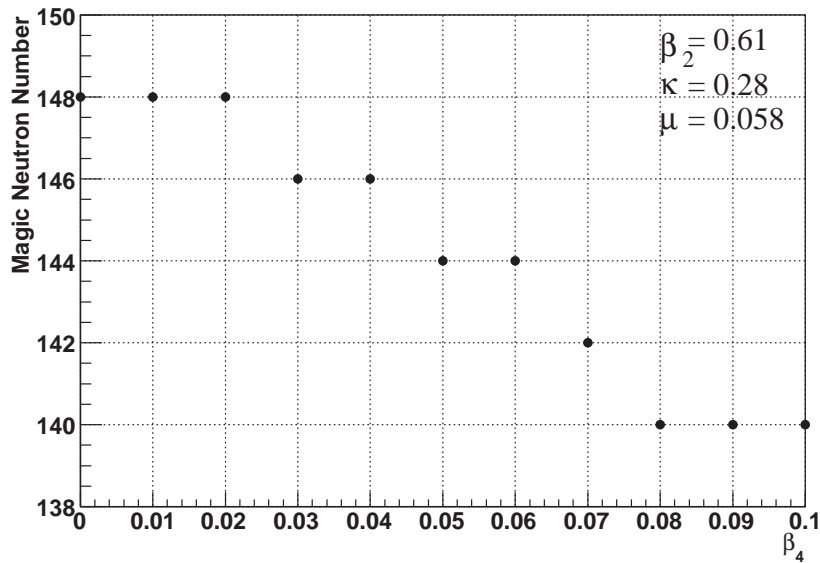


Figure 6.10: Deformed magic neutron numbers for ^{237}fPu as a function of the hexadecupole deformation β_4 and for constant parameters for β_2 , κ and μ as calculated within the Nilsson model. Only for $\beta_4 = 0.03$ or 0.04 the experimentally observed magic neutron number of $N = 146$ could be reproduced.

increased their spin-orbit force compared to standard values used by other theory groups by about 20 %, thus resulting in a neutron shell gap at $N = 148$. In our calculations κ and μ were varied in Eq. (2.12) in order to investigate the parameter space, where the Nilsson model would be able to reproduce the $N = 146$ magic neutron number for different values of β_4 at a constant superdeformed $\beta_2 \approx 0.6$.

Fig. 6.10 shows the evolution of the deformed shell gap for a variation of β_4 and constant values of κ and μ . Only for $\beta_4 = 0.03$ and $\beta_4 = 0.04$ a magic neutron number $N = 146$ can be reproduced. Furthermore it was found that for most neutron shell gaps and varying β_4 the $5/2^+[862]$ level is at or near the Fermi surface for ^{237}fPu , strongly indicating that this level indeed can be identified as the ground state single-particle level in ^{237}fPu .

Fig. 6.11 shows the evolution of magic neutron numbers in the landscape spanned by the coupling parameters κ and μ for fixed values of $\beta_2 = 0.6$ and $\beta_4 = 0.04$, respectively. There is only one region with $N = 146$ as magic neutron number, and again the $5/2^+[862]$ level is found at the Fermi surface.

Exemplifying these Nilsson calculations, Fig. 6.12 shows the single-particle states calculated for $\mu = 0.058$ and $\kappa = 0.28$ and $\beta_4 = 0.04$ around the superdeformed magic neutron number $N = 146$. Comparing these values to those of Table 6.2 we see that for the first minimum in the actinide regime a value of $\mu = 0.0613$ and $\kappa = 0.316$ are expected, respectively. The standard set of parameters is only the starting point for the Nilsson calculations and variations of up to 10 % in κ and μ are allowed [GUS67]. Inspecting Fig. 6.11 we see that both the standard parameter set and the parameter set identified in this work, lie in the region reproducing the magic neutron

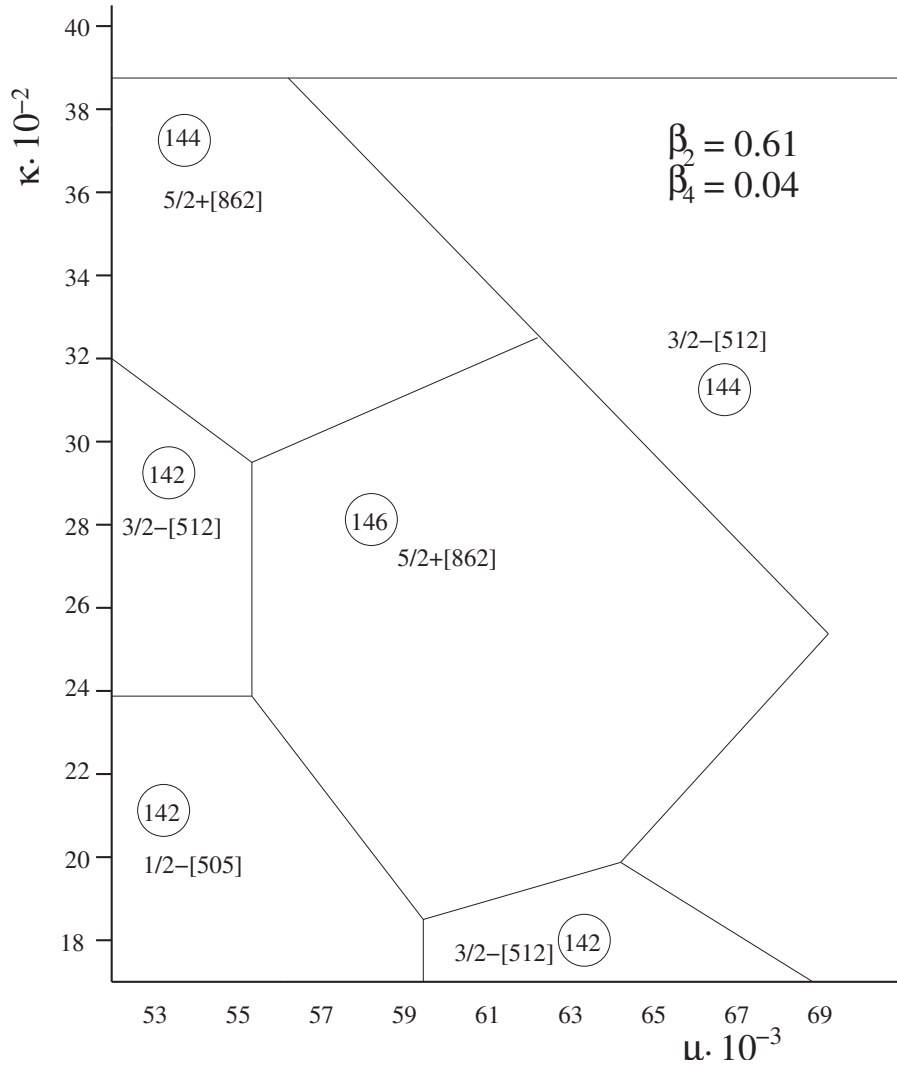


Figure 6.11: Evolution of deformed magic neutron numbers in the (superdeformed, $\beta_2 = 0.61$) second potential well of ^{237}Pu for a constant value of the hexadecupole deformation $\beta_4 = 0.04$, as a function of the coupling parameters κ and μ . Only one region with $N = 146$ appears, reproducing the experimentally identified deformed magic neutron number [MET74]. For each region the closest orbit to the Fermi surface is indicated.

Region	κ	μ
$N, Z < 50$	0.08	0
$50 < Z < 82$	0.0637	0.60
$82 < N < 126$	0.0637	0.42
$82 < Z$	0.0577	0.65
$126 < N$	0.0635	0.325
$126 \geq N$	0.0613	0.316

Table 6.2 Standard parameters κ and μ of the Nilsson Hamiltonian [GUS67].

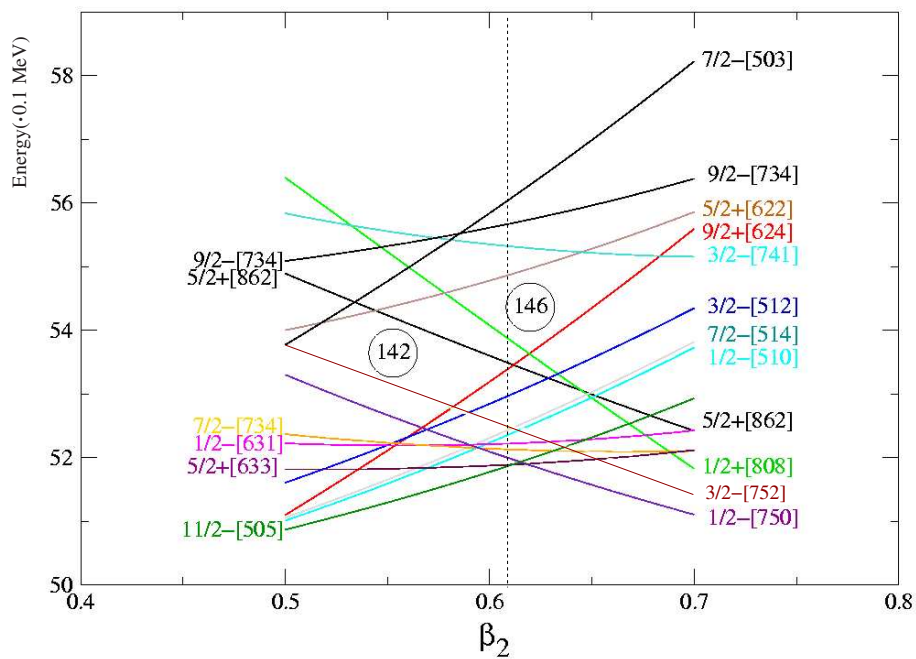


Figure 6.12: Evolution of the single-neutron energies in ^{237}fPu as a function of β_2 , obtained from Nilsson calculations with fixed parameters of $\beta_4 = 0.04$, $\kappa = 0.28$ and $\mu = 0.058$. The vertical dashed line marks $\beta_2 = 0.61$, where the calculated single-particle sequence best fits to the measured level structure in ^{237}fPu ($N = 143$).

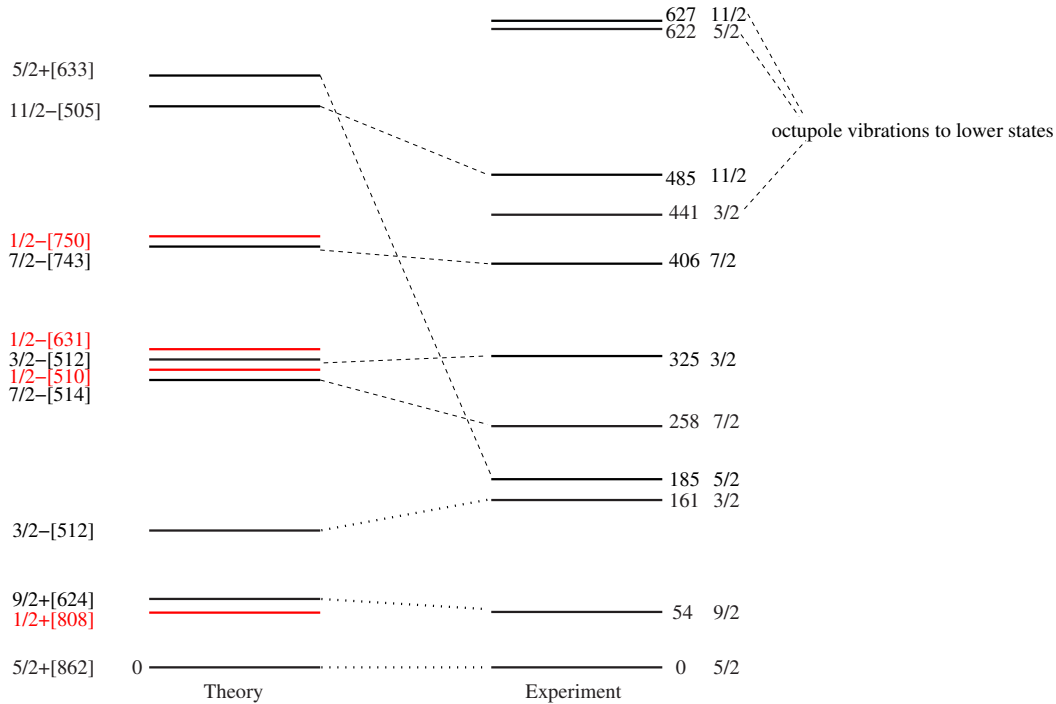


Figure 6.13: Single-particle levels from Nilsson model calculations compared to the experimental findings presented in chapter 6.1 for $\beta_2 = 0.61$. So far pairing has not been included in the calculations, so that the absolute energy of these levels cannot be predicted (the relative positions will stay the same). Indicated in red are the $J = 1/2$ bands proposed by the Nilsson model. Due to the Coriolis force, these may decouple and either be shifted in energy or couple to close-lying bands, altering their spin state. Also indicated are possible experimental candidates for an octupole coupling to lower states.

number $N = 146$. Inspecting the single-neutron structure of ^{237}Pu as displayed in Fig. 6.12, we see that for $\beta_2 \sim 0.61$ the configuration of single-particle states calculated using the Nilsson model is closest to the level structure measured in this thesis (indicated by the vertical dashed line).

Fig. 6.13 shows the single-particle states for ^{237}Pu for $\beta_2 = 0.61$, $\beta_4 = 0.04$, $\mu = 0.058$ and $\kappa = 0.29$ compared to the single-particle energies measured in this thesis (see chap. 6.1). As pairing has not been included in the calculations, an exact prediction of the single-particle energies is so far not possible, nevertheless the ground state predicted by the Nilsson model is a $5/2^+[862]$ orbit. Our measurements also suggest an $I = 5/2$ state at the Fermi surface. Furthermore we see that not only the experimentally determined ground-state spin of the 115 ns isomer is in agreement with the theoretical calculations, but also the ground state spin of the 1120 ns isomer, calculated to be an $I = 9/2^+[624]$ state.

As previously stated (see chapter 6.1) it was experimentally not possible to identify rotational bands with spin $1/2$, as these do not follow the same strict rigid rotor pattern as found for bands with higher spins. Moreover, the decoupling parameter in $K = 1/2$ bands, responsible for this deviation in the rotational pattern, can lead to single-particle states energetically so close to

each other that they may couple and the resulting single - particle state may have a different spin compared to the theoretically predicted state [BOM75]. This could explain why the predicted energy of the $5/2^+$ [633] relative to the other rotational bands is so much higher in Fig. 6.13. Furthermore, in $K=1/2$ bands with a large principal quantum number N , these bands can decouple and be shifted by as much as 1 MeV [EIS70]. The fact that pairing has so far been excluded does not alter the position of the rotational bands relative to one another unless these are coupled to a $J=1/2$ state and thereby shifted in energy.

It was seen in the study of ^{240}Pu [GAS02] that higher - lying rotational bands can be octupole vibrations coupled to lower - lying bands, which in our case of ^{237}Pu could explain the three higher - lying single - particle states at $I=5/2$ (622 keV), $I=9/2$ (575 keV) and $I=3/2$ (441 keV), which are not conclusively reproduced in the Nilsson model calculations.

6.3.3 Relativistic Hartree - Fock Bogoliubov calculations

The Hartree - Fock - Bogoliubov (HFB) theory [BEN03, KUC91, MAN75, PAA07, RIN80] provides a unified description of ph - and pp -correlations in nuclei and, when the self-consistent HFB equations are formulated in coordinate space, allows for a treatment of continuum effects in the presence of pairing. Most applications of HFB theory, which use a finite-range meson-exchange representation, describe the nucleus as a system of Dirac nucleons, coupled to effective mesons and the electromagnetic field.

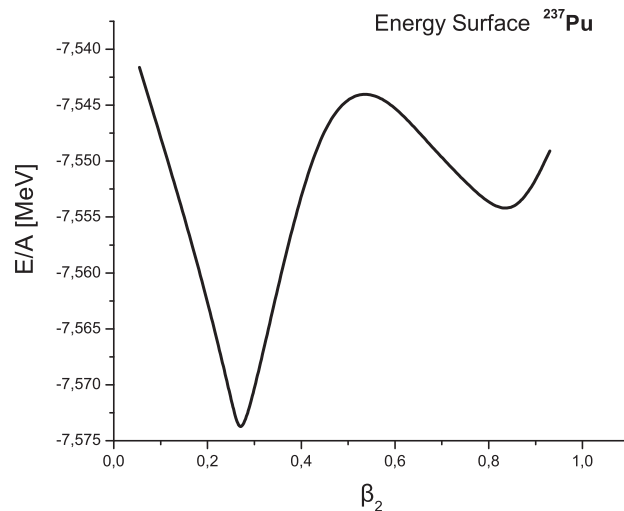


Figure 6.14: Potential energy surface for ^{237}Pu using a HFB diagonalisation [DAO07].

Fig. 6.14 shows the potential energy surface calculated for ^{237}Pu using a relativistic Hartree-Fock - Bogoliubov code [DAO07]. We see that a second minimum for ^{237}Pu is predicted, however located at a (hyperdeformed) value of $\beta_2 = 0.8$ rather than at $\beta_2 \approx 0.6$ as expected for superdeformed shape isomers. Thus it may not be surprising that a calculation of the single - particle structure in the second minimum resulting from HFB calculations, as shown in Fig. 6.15 was not

able to reproduce the deformed shell gap expected at $N = 146$. Nevertheless the $5/2^+[862]$ orbital is found to be at the Fermi surface as in all previous calculations either from Woods-Saxon or Nilsson-type calculations. A small variation of the parameter sets for the HFB code yields no improvement to the calculated single-particle spectra. Thus at least for the moment the HFB model is not able to reproduce realistic single-particle spectra for superdeformed fission isomers in the actinide region. In Woods-Saxon and Nilsson type calculations a variation of the parameter sets used led to an identification of the superdeformed magic neutron number $N = 146$ and a consequent suggestion of the single-particle level structure in ^{237}Pu . The results obtained from the HFB code are gained from a set of parameters currently able to describe the ground state properties of many nuclei in the periodic table. In a similar way it should be possible to alter the parameter sets for the HFB code, leading to a better description of the ground state properties of the same nuclei and a description of binding energies, nuclear radii, charge distributions, nuclear deformation parameters and fission barriers. This process however is very time consuming, it therefore might take some time before a HFB calculation describing the single-particle structure of ^{237}Pu becomes available.

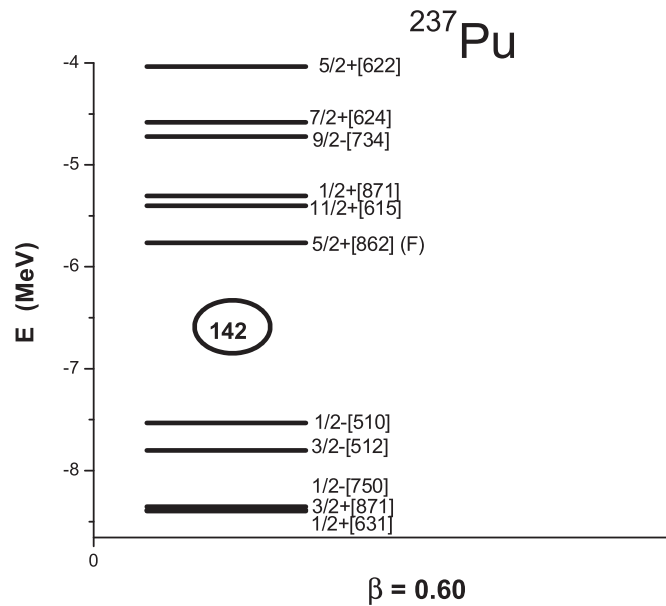


Figure 6.15: Single-particle states for neutrons in ^{237}Pu at $\beta = 0.6$ using a HFB diagonalisation. [DAO07].

Chapter 7

Conclusions and Outlook

The aim of this thesis was for the first time to investigate experimentally the single-particle level structure in the superdeformed actinide regime. In an experiment performed at the Cologne Tandem, using the highly efficient MINIBALL germanium detector array in conjunction with a small compact PPAC array constructed for this experiment, γ ray spectroscopy was performed. From the results of this experiment a detailed level-scheme of the superdeformed second minimum of ^{237}Pu was obtained. Furthermore the results were compared to theoretical models and a first tentative assignment of Nilsson quantum numbers was shown.

Inspecting the γ ray spectrum obtained during the three-week long experiment, 149 fission isomeric γ transitions were identified below 870 keV excitation energy and an isomeric lifetime was assigned to these. Subsequently the γ ray spectrum was disentangled into the two components, associated with the short-lived, low-spin isomer (115 ns) and the long-lived, high-spin (1120 ns) fission isomer. Nine rotational bands were identified, using an automated search in these spectra. Level schemes for the two fission isomers could be constructed using a Ritz combinatorial technique, allowing to identify the isomeric ground state spins of $5/2$ for the short-lived and $9/2$ for the long-lived isomer, respectively. γ transitions not only from the excited rotational bands to the ground-state band, but also inter-band transitions between excited rotational bands were found for both isomers, leading to an even more conclusive picture. Furthermore the excitation energy of the $9/2$ ground-state of the long-lived isomer was determined to be 54.0(3) keV above the $5/2$ ground state of the 115 ns isomer. Comparing the results to Nilsson calculations using a deformed harmonic oscillator potential, a deformed Woods-Saxon potential calculations and relativistic Hartree-Fock-Bogoliubov calculations resulted in a tentative assignment of the Nilsson quantum numbers $5/2^+$ [862] for the ground state single particle state of the short-lived isomer and $9/2^+$ [624] for the long-lived isomer in the superdeformed second potential minimum of ^{237}Pu . Furthermore the Nilsson single-particle states $3/2^-$ [512] and $7/2^-$ [514] could be identified for excited rotational bands. Thus Nilsson orbitals could be identified and characterised by their quantum numbers, for the first time in the second minimum of actinides, as the previous assignment of single-particle states in ^{239}Pu was based on theoretical calculations unable to reproduce the magic neutron number $N=146$ [MET74]. A detailed knowledge of the single-particle structure in the superdeformed actinide

regime enables to fine-tune theoretical models in this region, which will consequently lead to an improvement of predictions for e.g. the super-heavy element regime or fission barriers of heavy elements in the r-process path.

From the results obtained in this thesis (see chapter 6) it can be seen that there is still a large amount of spectroscopic information needed to fully understand the behaviour of shape isomers on the microscopic level. From the results presently obtained in $^{237\text{f}}\text{Pu}$ it seems that a significant conversion electron branch is present within the second minimum, with a strongly converted $9/2^+ \rightarrow 7/2^+$ transition at 31 keV - 18 keV (L_{III}) = 13 keV followed by the 23 keV rotational transition from the $7/2^+ \rightarrow 5/2^+$ transition. This rotational transition should be similar to the strong ^{239}Pu 6.3 keV L_{III} transition followed by an M-transition at 19.3 keV [BAC79]. In this scenario, similar to ^{239}Pu , in ^{237}Pu we now have an isomeric state, here the 1120 ns fission isomer, which can be populated, transported away from the strong background of δ -electrons and implanted onto a catcher foil, where it will consequently partially decay into the short-lived 115 ns isomer. Using, for example, a quadrupole-channel made of permanent magnets the electrons from the short-lived isomer could then be investigated in a silicon detector, shaded from the dominant prompt background of δ -electrons. Such future conversion electron measurements could result in a direct proof of the ground state spin assignment of 5/2 as derived from the present γ spectroscopy studies. Moreover, the superdeformed moment of inertia that has been assumed for the ground state rotational band in the present work could be directly accessed. Furthermore such measurements could prove that the higher-lying isomer indeed decays within the second minimum and would allow to verify the excitation energy and spin of the long-lived 1120 ns isomer.

The most promising case for further γ spectroscopic studies is given by ^{239}Pu . This nucleus can be studied via the $^{238}\text{U}(\alpha, 3n)$ reaction. Future measurements can draw from the advantageous fact that conversion electron spectroscopy in the second minimum has already been performed [BAC79]. Comparing these results to the now available theoretical models and the consequent assignment of Nilsson quantum numbers and combining this with the two-quasi-particle bands found in ^{240}Pu [GAS01] will yield a rather detailed picture around the magic neutron number $N=146$ for superdeformed actinide fission isomers.

Appendix A

Table of γ - energies and relative intensities

The following tables contain all experimental spectroscopic information derived from γ transitions that could be attributed to the decay of fission isomeric excited states in ^{237}Pu . These transitions, first listed inclusively in Tab. A have been disentangled into the contributions from the two fission isomers in ^{237}Pu (see Chap. 5.1), resulting in the separate Tables A.2 and A.3, respectively. These transitions and their respective properties have been used as input parameters for the construction of the isomeric level scheme using a Ritz combinatorial technique as described in Chap. 6.1, resulting in the spin assignments also included in Tables A.2 and A.3.

E_γ [keV]	Intensity	halfife [ns]	E_γ [keV]	Intensity	halfife [ns]	E_γ [keV]	Intensity	halfife [ns]
101.9(3)	0.06	111	293.8(2)	0.06	145	606.7(3)	0.08	121
111.8(3)	0.17	810	294.7(3)	0.10	128	608.8(2)	0.13	135
126.9(2)	0.33	710	301.9(2)	0.15	92	615.5(3)	0.04	91
128.3(3)	0.12	105	309.3(3)	0.06	95	628.9(2)	0.24	74
129.9(2)	0.11	610	312.1(1)	0.22	112	639.7(2)	0.11	116
130.8(3)	0.09	107	314.5(4)	0.09	540	651.3(2)	0.09	121
135.3(3)	0.05	145	319.6(3)	0.16	123	658.8(4)	0.04	116
139.1(3)	0.06	166	324.7(2)	0.24	112	662.5(2)	0.01	1180
142.7(2)	0.12	104	331.3(2)	0.16	101	664.8(2)	0.03	186
144.0(3)	0.09	116	332.5(3)	0.08	133	670.4(2)	0.03	173
147.5(3)	0.11	750	335.2(2)	0.17	974	675.0(2)	0.03	852
147.6(2)	0.17	118	336.1(1)	0.85	140	678.5(2)	0.03	112
150.7(2)	0.16	108	338.2(2)	0.20	594	681.0(3)	0.02	470
154.5(2)	0.17	65	342.3(2)	0.09	430	684.9(2)	0.03	1200
157.6(3)	0.09	128	345.8(3)	0.46	596	689.3(2)	0.05	147
158.3(3)	0.04	595	352.0(2)	0.80	1200	693.4(2)	0.03	523
161.0(2)	0.11	107	355.0(2)	0.30	106	696.7(2)	0.03	310
161.1(2)	0.34	96	357.3(2)	0.11	150	699.1(2)	0.03	611
163.4(3)	0.04	128	362.2(2)	0.11	100	705.5(2)	0.09	188
163.5(3)	0.06	128	369.8(2)	0.14	280	706.7(3)	0.02	105
171.7(3)	0.09	102	380.4(3)	0.13	310	709.3(2)	0.06	150
172.8(1)	1.00	106	382.5(2)	0.11	270	714.9(2)	0.04	110
175.1(2)	0.16	100	390.7(2)	0.09	250	722.2(2)	0.04	180
177.8(2)	0.10	740	402.5(2)	0.20	345	726.0(2)	0.03	220
178.7(2)	0.11	98	415.2(3)	0.06	79	738.9(2)	0.03	350
180.5(3)	0.05	140	431.1(2)	0.52	900	741.5(2)	0.06	99
181.2(3)	0.09	240	433.0(3)	0.05	133	748.5(2)	0.04	105
184.0(3)	0.06	125	434.7(2)	0.04	119	753.3(4)	0.01	320
185.6(1)	0.98	98	435.2(2)	0.11	80	758.5(3)	0.02	104
193.7(3)	0.08	89	439.0(2)	0.23	640	759.2(2)	0.07	106
197.1(2)	0.23	105	442.0(2)	0.16	119	771.9(2)	0.08	430
202.5(3)	0.16	103	443.8(2)	0.15	715	774.2(4)	0.01	326
204.0(3)	1.00	730	457.0(1)	0.43	126	782.9(2)	0.05	118
207.7(1)	0.48	105	464.2(2)	0.11	132	788.4(2)	0.06	145
214.8(2)	0.17	133	467.3(3)	0.06	92	793.0(3)	0.02	88
215.0(2)	0.16	103	470.3(4)	0.04	102	800.0(2)	0.03	215
222.2(2)	0.09	410	471.2(4)	0.03	105	801.3(2)	0.04	109
223.9(3)	0.06	108	478.0(3)	0.05	132	807.0(2)	0.04	139
229.5(2)	0.10	480	478.3(3)	0.08	350	812.5(2)	0.04	450
230.5(2)	0.10	655	486.1(3)	0.08	160	815.7(2)	0.05	125
232.1(2)	0.13	330	501.7(3)	0.08	91	822.0(2)	0.04	160
233.7(2)	0.23	680	507.2(2)	0.05	141	826.8(2)	0.04	84
234.9(2)	0.34	430	531.5(2)	0.07	210	830.8(2)	0.04	133
241.1(2)	0.21	470	570.9(2)	0.12	1187	834.0(2)	0.03	97
247.7(2)	0.23	882	572.3(2)	0.12	136	838.3(2)	0.06	152
249.1(3)	0.28	127	573.9(2)	0.26	1400	842.3(2)	0.03	163
269.7(2)	0.09	300	575.4(2)	0.11	830	849.0(3)	0.02	323
276.2(2)	0.09	595	575.6(3)	0.05	115	863.2(2)	0.03	112
278.9(2)	0.11	87	580.5(2)	0.11	114	867.3(2)	0.03	120
289.2(4)	0.04	125	603.2(2)	0.35	109			

Table A.1: γ -ray energies and halfives for the most dominant γ -ray transitions measured below 870 keV.

E_γ [keV]	Rel. Intensity	Transition	E_γ [keV]	Rel. Intensity	Transition
101.9(3)	0.06	5/2 to 7/2	309.3(3)	0.06	9/2 to 7/2
128.3(3)	0.12	5/2 to 7/2	312.1(1)	0.22	5/2 to 7/2
130.8(3)	0.09	7/2 to 9/2	319.6(3)	0.16	9/2 to 7/2
135.3(3)	0.05	9/2 to 11/2	324.7(2)	0.24	3/2 to 5/2?
139.1(3)	0.06	3/2 to 5/2	324.7(3)	0.05	11/2 to 11/2?
142.7(2)	0.12	7/2 to 7/2	331.3(2)	0.16	9/2 to 9/2
144.0(3)	0.09	7/2 to 9/2	332.5(3)	0.08	7/2 to 7/2
147.6(2)	0.17	9/2 to 11/2	336.1(1)	0.85	5/2 to 5/2
150.7(2)	0.16	5/2 to 7/2	355.0(2)	0.30	7/2 to 5/2
154.5(2)	0.17	7/2 to 9/2	357.3(2)	0.11	11/2 to 9/2
157.6(3)	0.09	11/2 to 11/2	362.2(2)	0.11	9/2 to 7/2
161.0(2)	0.11	5/2 to 3/2	415.2(3)	0.06	9/2 to 11/2
161.1(2)	0.34	3/2 to 5/2	433.0(3)	0.05	7/2 to 9/2
163.4(3)	0.04	3/2 to 3/2	434.7(2)	0.04	9/2 to 11/2
163.5(3)	0.06	5/2 to 7/2	435.2(2)	0.11	5/2 to 7/2
171.7(3)	0.09	9/2 to 9/2	442.0(2)	0.16	3/2 to 5/2
172.8(1)	1.00	5/2 to 5/2	457.0(1)	0.43	5/2 to 5/5
175.1(2)	0.16	7/2 to 7/2	464.2(2)	0.11	7/2 to 7/2
178.7(2)	0.11	11/2 to 11/2	467.3(3)	0.06	11/2 to 9/2
180.5(3)	0.05	11/2 to 9/2	470.3(4)	0.04	9/2 to 9/2
184.0(3)	0.06	9/2 to 9/2	471.2(4)	0.03	11/2 to 11/2
185.6(1)	0.98	5/2 to 5/2	478.0(3)	0.05	13/2 to 11/2
193.7(3)	0.08	11/2 to 9/2	486.1(3)	0.08	7/2 to 5/2
197.1(2)	0.23	7/2 to 5/2	501.7(3)	0.08	9/2 to 7/2
202.5(3)	0.16	9/2 to 7/2	507.2(2)	0.05	11/2 to 9/2
207.7(1)	0.48	7/2 to 5/2	572.3(2)	0.12	9/2 to 11/2
214.8(2)	0.17	9/2 to 7/2	575.6(3)	0.05	7/2 to 9/2
215.0(2)	0.16	11/2 to 9/2	580.5(2)	0.11	5/2 to 7/2
223.9(3)	0.06	13/2 to 11/2	603.2(2)	0.35	5/2 to 5/2
249.1(3)	0.28	7/2 to 9/2?	606.7(3)	0.08	7/2 to 7/2
249.1(3)	0.28	5/2 to 5/2?	608.8(2)	0.13	9/2 to 9/2
278.9(2)	0.11	5/2 to 3/2	615.5(3)	0.04	11/2 to 11/2
289.2(4)	0.04	7/2 to 7/2	628.9(2)	0.24	7/2 to 5/2
293.8(2)	0.06	11/2 to 11/2	639.7(2)	0.11	9/2 to 7/2
294.7(3)	0.10	9/2 to 11/2	651.3(2)	0.09	11/2 to 9/2
301.9(2)	0.15	7/2 to 9/2	658.8(4)	0.04	13/2 to 11/2

Table A.2: γ -ray transitions, and their relative intensities, used for the construction of the short-lived low-spin level scheme using a Ritz combinatorial technique.

E_γ [keV]	Rel. Intensity	Transition	E_γ [keV]	Rel. Intensity	Transition
79.96(12)	0.06	17/2 to 15/2	342.0(3)	0.05	13/2 to 15/2
87.8(2)	0.07	13/2 to 15/2	342.3(2)	0.09	13/2 to 11/2
111.8(3)	0.17	13/2 to 15/2	345.8(2)	0.46	9/2 to 11/2
126.9(2)	0.33	15/2 to 15/2	350.6(3)	0.03	11/2 to 13/2
129.9(2)	0.11	15/2 to 15/2	352.0(2)	0.80	7/2 to 9/2
147.5(3)	0.11	9/2 to 9/2	368.9(2)	0.06	15/2 to 15/2
158.3(3)	0.04	11/2 to 11/2	369.8(2)	0.14	11/2 to 7/2
175.8(2)	0.09	15/2 to 13/2	380.4(3)	0.13	13/2 to 13/2
177.2(3)	0.04	19/2 to 17/2	382.5(2)	0.11	9/2 to 9/2
177.8(2)	0.10	9/2 to 7/2?	385.5(2)	0.06	11/2 to 11/2
177.8(3)	0.10	17/2 to 15/2?	390.7(2)	0.09	15/2 to 15/2
178.5(3)	0.04	13/2 to 15/2	394.5(2)	0.07	11/2 to 11/2
181.2(3)	0.09	11/2 to 9/2	394.8(3)	0.03	17/2 to 17/2
189.0(3)	0.04	11/2 to 13/2	395.0(3)	0.03	13/2 to 13/2
189.5(3)	0.09	15/2 to 13/2	402.5(2)	0.20	19/2 to 15/2
196.2(2)	0.09	11/2 to 9/2	415.8(3)	0.03	11/2 to 9/2
196.2(2)	0.09	13/2 to 11/2	421.7(4)	0.03	15/2 to 13/2
199.7(2)	0.20	9/2 to 11/2	424.3(2)	0.07	13/2 to 11/2
204.0(3)	1.00	7/2 to 9/2	431.1(2)	0.52	11/2 to 9/2
222.2(2)	0.09	11/2 to 7/2	439.0(2)	0.23	13/2 to 11/2
229.5(2)	0.10	13/2 to 9/2	443.8(2)	0.15	15/2 to 13/2
230.5(2)	0.10	15/2 to 15/2	448.8(2)	0.06	17/2 to 15/2
232.1(2)	0.13	13/2 to 13/2	456.2(3)	0.04	19/2 to 17/2
233.7(2)	0.23	11/2 to 11/2	460.5(2)	0.07	15/2 to 17/2
234.9(2)	0.34	9/2 to 9/2	478.3(3)	0.08	13/2 to 15/2
241.1(2)	0.21	17/2 to 13/2	493.3(3)	0.04	11/2 to 13/2
247.7(2)	0.23	13/2 to 15/2	515.0(3)	0.03	17/2 to 17/2
267.9(2)	0.02	11/2 to 9/2	517.2(3)	0.03	15/2 to 15/2
269.7(2)	0.09	11/2 to 13/2	531.5(2)	0.07	13/2 to 13/2
276.2(2)	0.09	13/2 to 11/2	537.5(2)	0.04	11/2 to 11/2
283.8(3)	0.04	15/2 to 13/2	568.5(2)	0.04	17/2 to 15/2
314.5(4)	0.09	15/2 to 17/2	570.9(2)	0.12	15/2 to 13/2
327.5(3)	0.03	13/2 to 15/2	573.9(2)	0.26	11/2 to 9/2
335.2(2)	0.17	11/2 to 13/2	575.4(2)	0.11	13/2 to 11/2
337.5(5)	0.03	15/2 to 17/2	597.5(3)	0.02	19/2 to 17/2
338.2(2)	0.20	17/5 to 15/2			

Table A.3: γ -ray transitions, and their relative intensities, used for the construction of the long-lived high-spin level scheme using a Ritz combinatorial technique.

Appendix B

Solar Cells

Fission isomer studies with low reaction cross sections require efficient fission fragment detection systems. The main requirements are: A good time resolution, as when using a pulsed beam (in our case $\Delta t \simeq 400$ ns) in coincidence with fission fragments one has to distinguish between the prompt and the delayed fission component, where for ^{237}Pu we find two shape isomers with $t_{1/2} = 115$ ns and $t_{1/2} = 1120$ ns, respectively. The energy resolution should allow for the separation of fission fragments from background contributions such as e.g. scattered beam particles.

Commercially available silicon solar cells offer an attractive and cost effective solution to this demand. In order to successfully apply solar cells in fission isomer studies, besides the ability to resolve the fission fragment mass distribution the time resolution has to be optimised in order to allow for an unambiguous identification of delayed fission events. For the intended use in the study of the 115 ns and 1120 ns isomers of ^{237}Pu a time resolution of approximately 20 ns is required.

So it was our first approach, before finally building the PPAC array that was actually used in the experiment as described in the previous chapters, to design and build a 4π fission fragment detector set-up based on solar cells. In a first experiment on ^{237}Pu at the Cologne Tandem accelerator this detector system was used and successfully operated, however, for the final experiment a different solution based on PPAC gas detectors was implemented in spite of the larger effort required for the operation of these detectors. The reason for this change of the detector concept was not connected to the performance of the solar cell detectors, but rather due to the thickness of the rolled Uranium target, which could not be produced thinner than 3.7 mg/cm^2 (due to oxygen contaminants in the metallic isotopic material) thus being a factor 2.3 thicker compared to experiments performed earlier [PAN98]. The increased target thickness leads to a large energy loss of the fission fragments in the target and hence only to relatively small signal amplitudes that can be detected with the solar cells. Unfortunately the signal amplitudes turned out to be that low, that only a fraction of about 0.1 % of all signals could have been discriminated from the electronic noise level, thus drastically reducing the detection efficiency.

As the solar cell detector system still represents an attractive option for fission fragment detection, provided a sufficient signal amplitude is given, the following chapter documents the

design properties and technical characteristics of the 4π detector array designed, built and commissioned in the framework of this dissertation.

B.1 Design and technical realisation of the solar cell detector array

When photons with an energy exceeding the band gap energy are incident on a p-n junction, electron-hole pairs are produced. The electrons produced within the depletion layer and many of those produced within about a diffusion length on the n side can be swept into the p region. The junction therefore behaves as a current source, with the current proportional to the intensity of the incident radiation [HOO00]. Solar cells exploit this effect to generate a current from incident light. In our experiments we used fission fragments incident on the solar cells to generate a charge which can be detected and is proportional to the fission fragment energy. Fig. B.1 shows a typical ASE TE16SF solar cell with and without its carrier board, which serves as mounting support and electrical connectors.

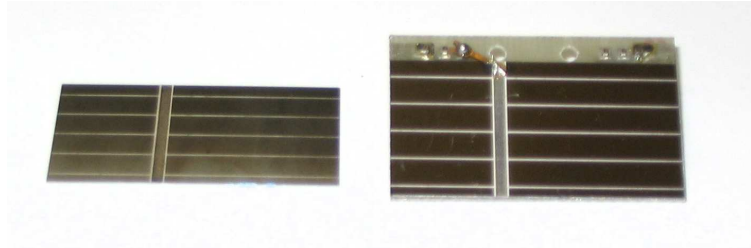


Figure B.1: Typical ASE TE16SF solar cell with (right) and without its carrier board (left).

As discussed in chapter 3, shape isomeric studies are performed with a very small population cross section of the shape isomers, therefore requiring an efficient fission fragment detection system. In our case it was decided to build and test detectors with an active area of $20 \times 40 \text{ mm}^2$. These are glued to a carrier board of size $25 \times 40 \text{ mm}^2$, acting as a carrier plate for the fragile solar cells as well as for carriers of the electrical connectors. First the solar cells are glued onto the conductive surface of the 1 mm thick epoxy carrier plate using a conductive silver glue, then the charge collecting grid of the cell is connected to one of two 2-pin connectors soldered onto the plate via a small copper pin. The commercial monocrystalline solar cells were initially covered with an anti-reflective layer of TiO_2 . In order to reduce the energy loss of the fission fragments this dead layer was etched off in a 10% HF solution for 10 s. Fig. B.2 shows a solar cell of Type ASE TE16SF prior to etching in a 10% HF solution and a solar cell after etching for 10 s.

The design of the preamplifier for the solar cells was developed in Saclay (see Fig. B.3) [BUE03] and improved in Munich. Fig. B.4 shows the output signal of the preamplifier (negative yellow trace) as measured with an oscilloscope. Also shown is the shaped preamplifier signal after it has been put through an amplifier ($1.5 \mu\text{s}$ shaping time and an amplification factor of 20). The typical signal to noise ratio is 5:1 with a typical signal size of 300 mV to 2 V.

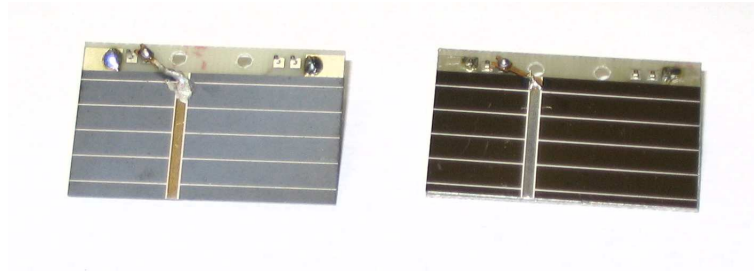


Figure B.2: shows a solar cell of Type ASE TE16SF (right) prior to etching in a 10% HF solution and a solar cell after etching for 10s (left).

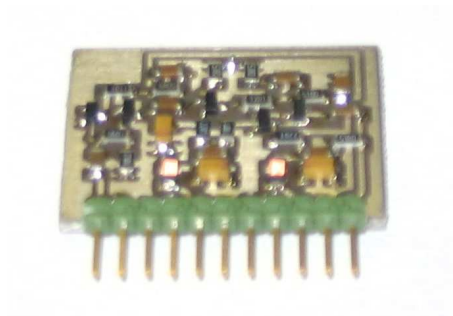


Figure B.3: A preamplifier built in Munich based on a design from Saclay.

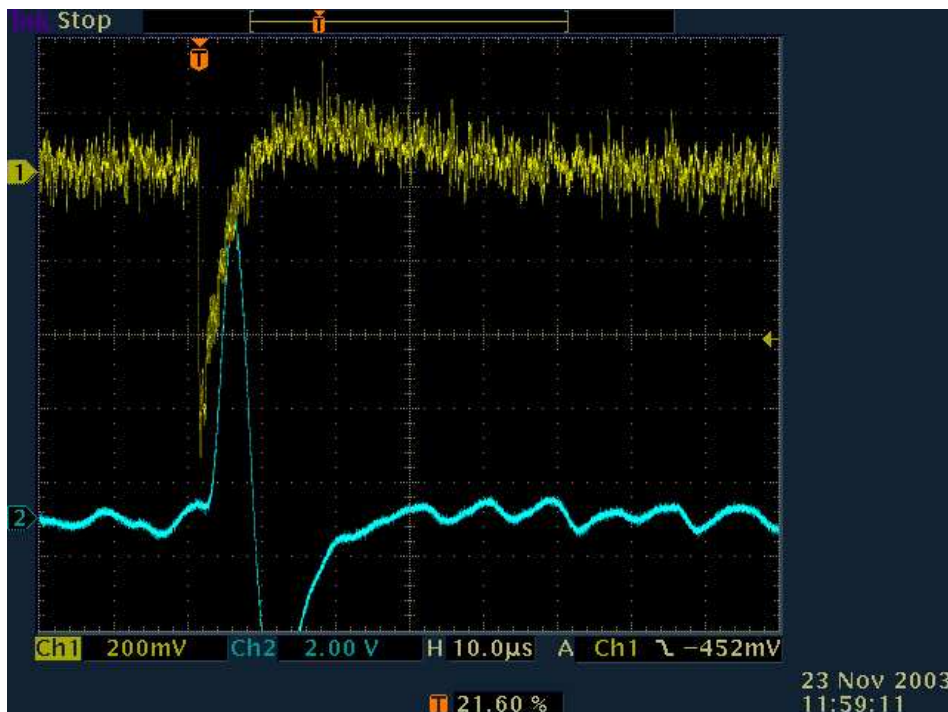


Figure B.4: Preamplifier (yellow trace) and shaper (blue) signals, from an ASE TE16SF solar cell, as seen from an oscilloscope screen. A signal to noise ratio of 5:1 can be achieved.

B.2 Offline Measurements

Off- and online experiments were performed to characterise the performance of two different types of monocrystalline solar cells (manufacturer: ASE, TZZE4020 and TE16SF, $2 \times 4 \text{ cm}^2$). To establish whether the use of silicon solar cells is feasible as a particle detector for fission fragments, a series of test measurements was performed, using a ^{252}Cf fission source (activity $\sim 5 \text{ kBq}$). In order to allow for a quantitative comparison of fission mass distributions measured with different types of solar cells, the mass distribution was parameterised according to Schmitt-Pleasanton [THE97] as shown in Fig. B.5. The most important parameters are given by the peak heights of the low-energy (high mass) peak N_H and the high-energy (low mass) peak, N_L together with the depth of the valley inbetween the two peaks, N_V . From a comparison of the ratios between N_L/N_V , N_H/N_V and N_L/N_H the performance quality of different silicon solar cells can be assessed.

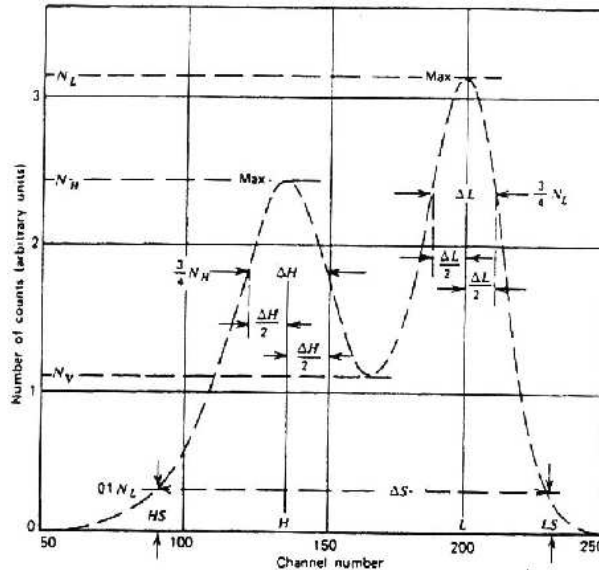


Figure B.5: Schmitt-Pleasanton reference spectrum of the fission fragment mass distribution of ^{252}Cf [THE97]. Indicated are the parameters used to characterise the performance of silicon solar cells. The important parameters are: N_L , N_H and N_V , where N_L denotes the height of the low-energy (high mass) peak, N_H the high-energy (low mass) peak, and N_V the valley height.

The first tests performed were to characterise the energy resolution and the lifetimes (i.e. radiation hardness) of the solar cells. Figure B.6 shows a typical energy spectrum for a solar cell of type TE16SF, the blue curve shows the mass distribution after one day of irradiation with $\sim 2 \text{ kHz}$ of fission fragments, the red curve shows the same information after 7 days of irradiation with 2 kHz of fission fragments. As one can clearly see a separation between high and low energy fission fragments, the energy resolution was sufficient for our intended use as fission fragment detectors. Furthermore as no significant change in the N_L/N_V , N_H/N_V and N_L/N_H ratios occurred over a period of 7 days of constant irradiation with 2 kHz of fission fragments, the radiation hardness of the solar cells proved to be sufficient for our fission fragment experiments, with comparable fission event rates.

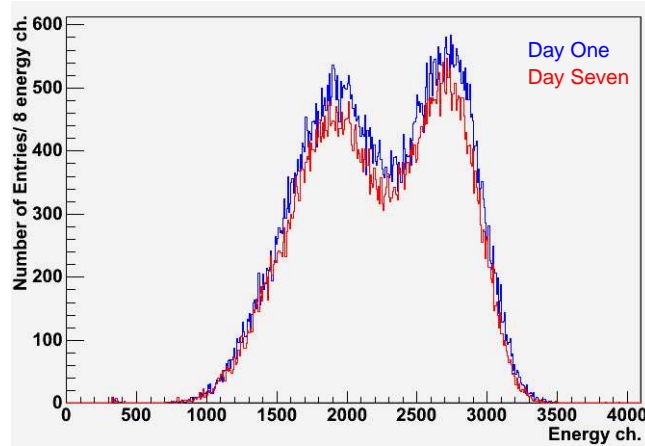


Figure B.6: Typical energy spectrum of spontaneous fission from a ^{252}Cf source (equivalent to the fission fragment mass distribution) measured with a solar cell of type TE16SF. The blue curve shows the mass distribution after one day of irradiation with ~ 2 kHz fission fragments, the red curve displays the situation after one week of continuous operation, revealing no obvious degradation of the solar cell performance by radiation damage. Both spectra contain data from 10 minutes of irradiation of the solar cell.

As the solar cells are initially coated with a TiO_2 layer, the angular dependency of the mass resolution angular dependency of two types of solar cells was measured, for both etched and non-etched cells. The solar cells were placed at ~ 10 cm distance to a ^{252}Cf source and the angle of the source was varied from $\sim 20^\circ$ to $\sim 90^\circ$ around the solar cells. The results of these measurements are shown in Fig. B.7 [SCH04].

The comparison of the peak to valley ratios for the heavy- and light-fragment mass peaks (N_H/N_V and N_L/N_V) of the ^{252}Cf fission fragment distribution consistently shows larger values for the etched cells. Furthermore, no pronounced angular dependency was observed. This indicates a rather thin anti-reflective layer. However, whilst no significant angular dependency was found for the intensity ratio N_L/N_H for the TZZE4020 cells, in the case of the TE16SF cells an angular suppression of the high energetic (light fragment) mass peak intensity at small angles was observed (Fig. B.12c). This may indicate an influence of the TiO_2 layer even after the solar cells were etched.

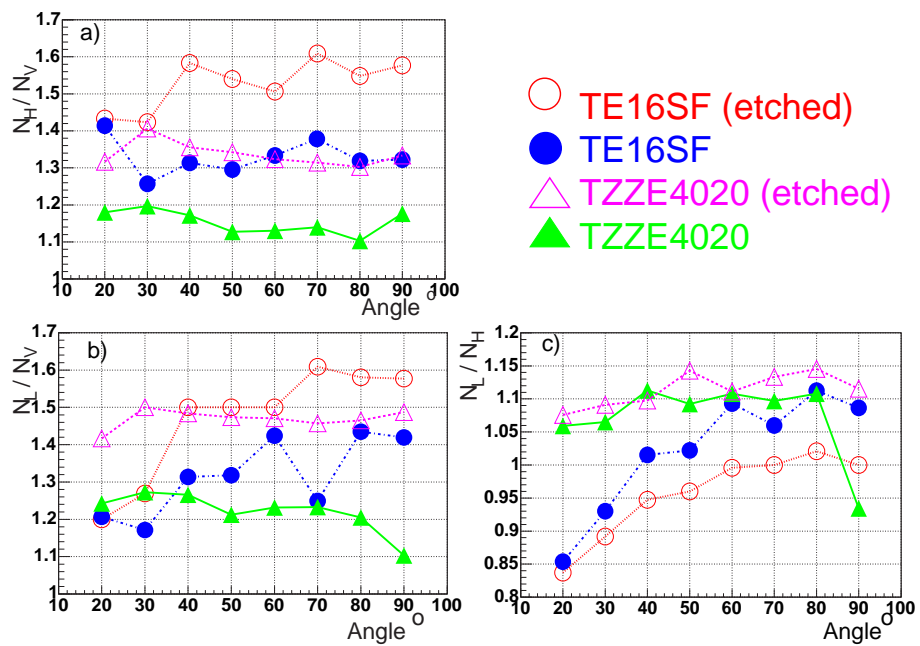


Figure B.7: Angular-dependent response of two types of solar cells (each etched and non-etched) to a ^{252}Cf fission source. N_H (N_L) denotes the intensity of the heavy (light) fragment peak. N_V is the intensity in the valley of the mass distribution.

B.3 Online Measurements Munich

In order to determine the time resolution of the two types of solar cells, a series of test experiments were performed at the Munich Tandem accelerator. A pulsed α beam ($\Delta t \simeq 200$ ns, $E_\alpha \simeq 24$ MeV) was focused onto a thin ^{235}U target (U_2O_3 with $\sim 80 \mu\text{g}/\text{cm}^2$ on a C backing), inducing fission. The time resolution was determined for the fission fragments. The solar cells were placed at angles between 30° and 60° with respect to the beam (~ 4 cm distance from the target). The beam current was ~ 1 nA, inducing a count rate of about 50 Hz in a single solar cell. The schematics of the electronics used in these experiments is shown in Fig. B.8. In these measurements the TDC was set to a "common start" mode, where the trigger was given by a coincidence (AND) from the logical OR of the solar cells with the beam pulse. The time of flight of fission fragments was measured in coincidence with the fragment energy relative to the pulsed beam.

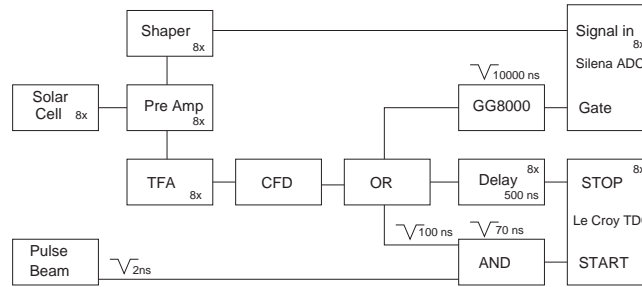


Figure B.8: Scheme of the read-out electronics used in the test measurements to determine the time resolution of silicon solar cells. The TDCs were set to a "common start" mode, where the trigger was given by a coincidence between the logical "OR" of the solar cells and the beam pulse.

Fig. B.9 shows the prompt fission spectrum following the $^{235}\text{U}(\alpha, f)$ reaction. A clear separation of scattered α -beam particles and fission fragments is visible. Furthermore the energy resolution obtained in the offline measurements using a ^{252}Cf source was reproduced.

Figure B.10 shows the energy versus time spectrum for the $^{235}\text{U}(\alpha, 2n)$ reaction. A clear separation between the light-mass high energy fragments and the high-mass low-energy fragments can be concluded. By gating on the light-mass fragment (red circle) and analysing the corresponding fragment time of flight the time resolution of the solar cells was found to be 18 ns, which is sufficient for shape isomer studies in $^{237\text{f}}\text{Pu}$ (see Fig. B.14 b).

After having obtained these promising results with the rather simple and easy-to-handle solar cells, a dedicated detector system was designed and built for use together with the high-resolution MINIBALL γ -ray spectrometer,

Figure B.11 shows a schematic view of a compact 4π solar cell array set up [MOR03] used in the first MINIBALL test experiment. In this setup 16 ASE solar cells of type TE16SF etched for 10 s in 10 % HF solution were used [TE16SF] in order to detect the fission fragments following the $^{235}\text{U}(\alpha, 2n)$ reaction. The solar cells were arranged in a 4π geometry around the target with a solid angle coverage of 73 %. Two hexagonal rings with 6 detectors each were placed to the

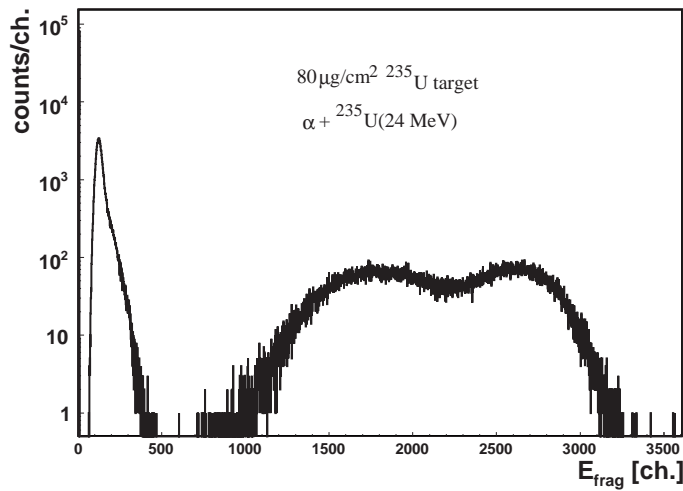


Figure B.9: Prompt fission fragment energy spectrum following the $^{235}\text{U}(\alpha, f)$ reaction, using a 24 MeV α beam focused onto a $80 \mu\text{g}/\text{cm}^2$ ^{235}U target. A clear separation between the double humped fission fragment energy spectrum and scattered low-energy beam particles is visible. The time resolution of the solar cells was found to be 18 ns, which is sufficient for shape isomer studies in ^{237}Pu (see Fig. B.14 b.).

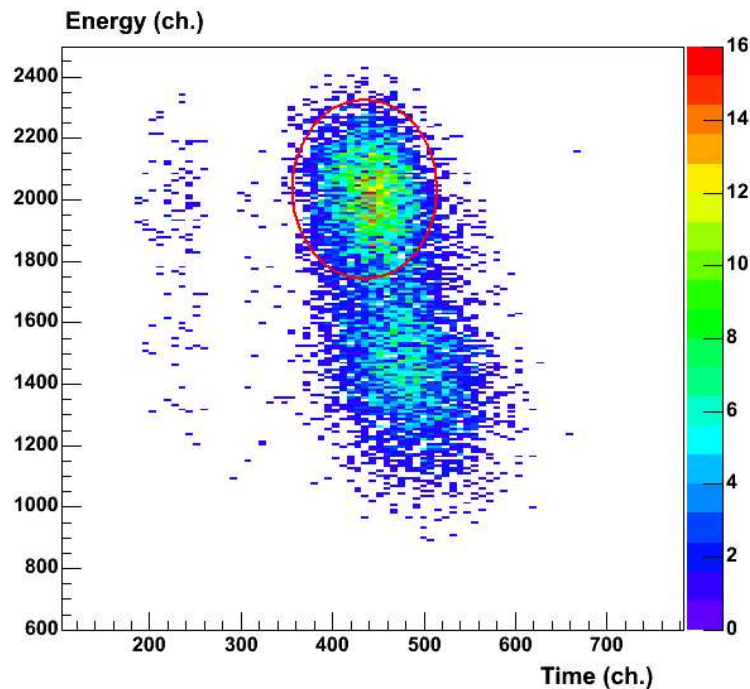


Figure B.10: Energy versus time spectrum for the $^{235}\text{U}(\alpha, 2n)$ reaction, registered with a silicon solar cell at $E_\alpha = 24$ MeV. A clear separation between the light-mass high energy fragment (red circle) and the high-mass low-energy fragment is visible.

left and right - hand side of the target, which could be inserted via a slit inbetween the two rings. The end caps of this barrel-like structure were covered by 2 solar cells at each side, leaving a narrow slit opening (~ 4 mm) for the entrance and exit of the α beam.

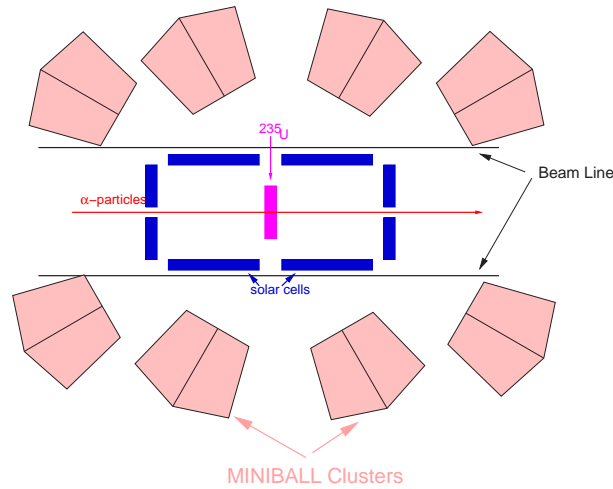


Figure B.11: Schematic view of the 4π solar cell array set up (blue modules) surrounded by the MINIBALL γ -ray detectors. This experimental set-up was used for the first test experiment on ^{237}Pu at the Cologne Tandem accelerator.

For the γ -spectroscopy experiment at Cologne a thick metallic ^{235}U -target (~ 3.7 mg/cm²) was used, which was inserted into the central slit of the detector array (see Figure B.11 for a schematic overview), defining the origin of the reaction.

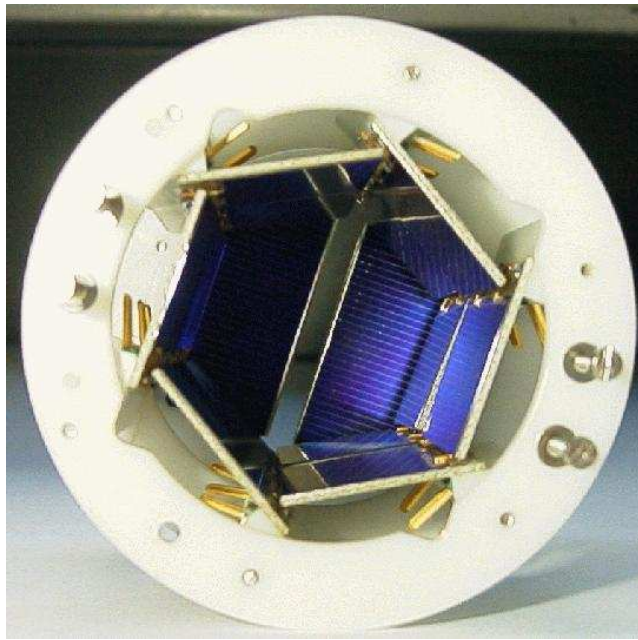


Figure B.12: View on the interior active area of the 4π solar cell detector array, which has been used in a first test experiment as the trigger detector for the γ -spectroscopy studies on shape isomers in ^{237}Pu together with the MINIBALL γ -ray detector array. Two additional solar cell modules forming the frontside end cap of the detector barrel have been removed to take this photograph.

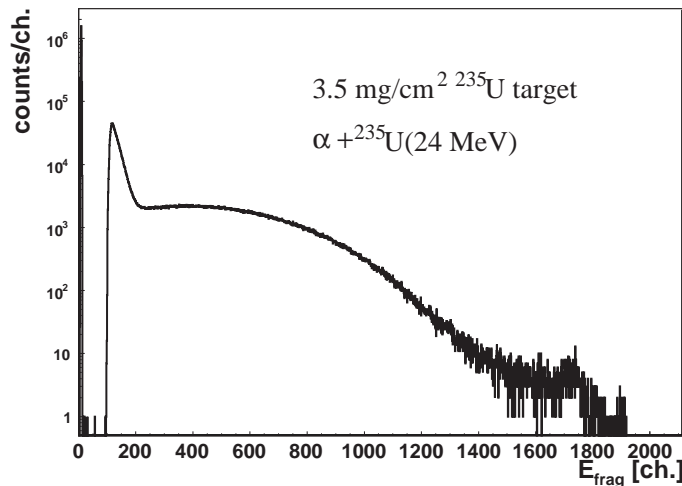


Figure B.13: Prompt fission fragment energy spectrum following the $^{235}\text{U}(\alpha,2n)$ reaction using a 24 MeV α beam focused onto a 3.5 mg/cm^2 ^{235}U target. No clear separation between fission fragments and scattered beam particles is possible (see Fig. B.9 for comparison), the energy resolution is therefore not sufficient to separate between prompt and delayed fission particles. Furthermore the time resolution of the fission fragments in this reaction is larger than 70 ns (see Fig B.14 b.) which again is not suitable for an efficient gating on isomeric fission fragments.

B.4 Online Measurements Cologne

The detector system shown in Figure B.12 was implemented into the MINIBALL array at the IKP in Cologne. While for the online test measurements in Munich a thin UO_2 target ($80 \mu\text{g/cm}^2$) had been used, in Cologne a thick metallic ^{235}U target was placed at the centre of the detector system. Fig. B.13 shows the energy spectrum of signals detected by a TE16SF solar cell following the $^{235}\text{U}(\alpha,2n)$ reaction ($E_\alpha = 24 \text{ MeV}$). The strong background contribution at low energies results from scattered α -projectiles, while at higher energies the double-humped structure originating from the two fission fragments is clearly visible.

Selecting only the low-mass high-energy fission fragments results in the time spectrum of Fig. B.14 a). The time distribution with a width of $\sim 70 \text{ ns}$ (FWHM) reflects the spread of fission fragment flight times due to the thick target. Applying the same cut on low-mass high-energy fission fragments as shown in Fig. B.10 for a thin target results in the time spectrum of Fig. B.14 b) exhibiting a time resolution of $\Delta t \sim 18 \text{ ns}$.

The production of these rolled metallic ^{235}U targets represents a crucial technical challenge for this type of experiments, as the material is highly oxidising, therefore requiring an oxygen-free atmosphere from the production in the hot lab in Munich until the installation in the target chamber in Cologne. For the experiments isotopic target material was available, which turned out to be contaminated with oxidation seeds, thus limiting the achievable target thickness to $3.5\text{-}4 \text{ mg/cm}^2$, which is the borderline of the energy stopping range of fission fragments in the target material, resulting in a wide, low-energy fragment distribution leaving the target. During this test, the performance of the detector set up and the quality of the beam pulse system

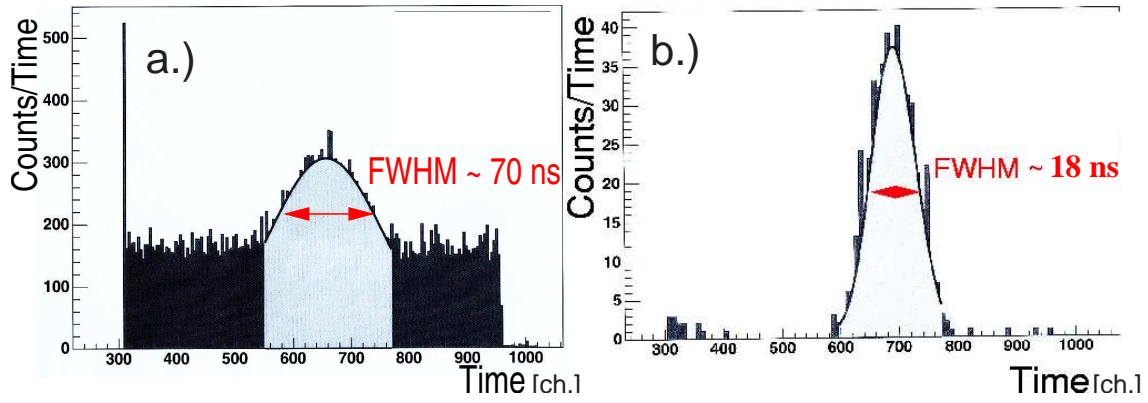


Figure B.14: Part a) shows the time resolution of the solar cells (~ 75 ns) using a 3.5 mg/cm² ^{235}U target. Figure B.14 b) displays the time spectrum of the solar cells using a 80 $\mu\text{g}/\text{cm}^2$ ^{235}U target, exhibiting a time resolution of ~ 18 ns. The difference in time resolution is due to the flight time envelope of fission fragments emitted from the target, where in the 3.5 mg/cm² target the fragments are all slowed-down significantly in contrast to the 80 $\mu\text{g}/\text{cm}^2$ ^{235}U target.

($\Delta t = 400$ ns, pulse width = 2.5 ns) was tested, together with the performance of the solar cell array.

While the detectors in principle proved to be operational, the large target thickness imposed to us by the quality of the available metallic ^{235}U isotope material (in fact no metallic ^{235}U material is presently commercially available world-wide) forced us to abandon the idea of using the silicon solar cell detector array for the γ -spectroscopy studies on ^{237}Pu . Otherwise most of the fission fragment signal amplitude would have been overlapped with the scattered α beam particles and the detector noise, reducing the detection efficiency in an unacceptable way. This finally motivated the change of the detector concept and led to the construction of the PPAC array, which has been discussed in chapter 3.

Bibliography

- [ANA83] M. R. Anastasio, L. S. Celenza, W. S. Pong, and C. M. Shakin, Phys. Rep. 100, (1983) 327
- [BAC79] H. Backe, L. Richter, D. Habs, V. Metag, J. Pedersen, P. Singer and H. J. Specht, Phys. Rev. Lett. **42** (1979).
- [BEN03] M. Bender, P. H. Heenen and P. G. Reinhard, Rev. of Mod. Phys. **75** (2003) 121.
- [BET96] K. Bethge, *Kernphysik - Eine Einführung*, (Springer, Heidelberg 1996).
- [BJO67] S. Bjørnholm, J. Borggreen, L. Westergaard and V. A. Karnaukhov, Nucl. Phys. **A95** (1967) 513.
- [BJO80] S. Bjørnholm and J. E. Lynn, Rev. Mod. Phys. **52** (1980) 725.
- [BLO89] J. Blons, Nucl. Phys. **A502** (1989) 121.
- [BOH69] A. Bohr and B. R. Mottelson, *Nuclear structure*, vol. 1 (Benjamin, New York, 1969).
- [BOM75] A. Bohr and B. R. Mottelson, *Nuclear structure*, vol. 2 (Benjamin, New York, 1975).
- [BOWH39] N. Bohr and J. A. Wheeler, Phys. Rev. **56** (1939) 426.
- [BUE02] T. Bürvenich, D.G. Madland, J.A. Maruhn, P.-G. Reinhard, Phys. Rev. **C65**, 044308 (2002).
- [BUE03] A. Bürger, H. Hübel, E. Mergel, A. Al-Khatib, P. Bringel, S. Chmel, T. Morgan, N. Nenoff, A. Neußer, G. Schönwaßer und A.K. Singh, DPG Frühjahrstagung Tübingen, HK12.10 (2003).
- [BRI71] H. C. Britt, S. C. Burnett, B. H. Errkila, J. E. Lynn and W. E. Stein, Phys. Rev. **C4**, (1971) 1444.
- [CAEN] Nuclear Aerospace Microelectronics RFID CAEN, URL <http://www.caen.it/>.
- [CAR87] J. Carlson, Phys. Rev. **C 36** (1987) 2026
- [CEL86] L. S. Celenza and C. M. Shakin, *Relativistic Nuclear Physics*, World Scientific, Singapore, (1986).
- [COL61] L. J. Colby jr., M. LaSalle Shoaf, J. W. Cobble, Phys. Rev. **121**, (1961) 1415.
- [CWI94] S. Ówiok, W. Nazarewicz, J. X. Saladin, W. Plociennik and A. Johnson, Phys. Lett. **B322** (1994) 304.
- [DAO07] J. Daoutidis and P. Ring, private communication (2007).

- [EBE01] J. Eberth, G. Pascovici, H. G. Thomas, N. Warr, D. Weisshaar, D. Habs, P. Reiter, P. Thirolf, D. Schwalm, C. Gund, H. Scheit, M. Lauer, P. Van Duppen, S. Franchoo, M. Huyse, R. M. Lieder, W. Gast, J. Gerl, K. P. Lieb and the MINIBALL collaboration, *Progr. Part. Nucl. Phys.* **46** (2001) 389.
- [EGI07] T. von Egidy, private communication (2007).
- [EHR72] G. Ehrling and S. Wahlborn, *Phys. Scripta* **6** (1972) 94.
- [EIS70] J. M. Eisenberg and W. Greiner, *Nuclear Models Collective and Single-Particle Phenomena*, Vol. 1 (North Holland Publishing Co., Amsterdam 1970).
- [FET71] A. L. Fetter and J. D. Walecka, *Quantum theory of Many-Particle Systems*, McGraw-Hill Book Company, New York 1971.
- [FIR96] R. B. Firestone, *Table of Isotopes*, Eighth Edition Volume II (1996).
- [FLE68] G. N. Flerov, J. P. Gangrsky, B. N. Markov, S. M. Polikanov und H. Jungclausen, *Sov. Nucl. Phys.* **6** (1968) 12.
- [FUC06] C. Fuchs, H. H. Wolter, in: F. Gulminelli, et al. (Eds.), *Dynamics and Thermodynamics with Nuclear Degrees of Freedom*, *Eur. Phys. J. A* **30** (2006) 5
- [GUS67] C. Gustafson, I. L. Lamm, B. Nilsson and S. G. Nilsson, *Arkiv Fysik* **36** (1967).
- [GAS01] D. Gaßmann, P. G. Thirolf, E. Mergel, D. Habs, M. Chromik, J. Domscheit, A. Görgen, K. Hauschild, H. Hübel, M. Hunyadi, A. Krasznahorkay, A. Lopez-Martens S. Neumann, A. Neußer, D. Pansegrau, P. Reiter, H. Scheit, G. Schönwaßer, D. Schwalm, *Phys. Lett. B* **497** (2001) 181.
- [GAS02] D. Gaßmann, Dissertation, LMU München (2002).
- [GRE96] W. Greiner and J.A. Maruhn, *Nuclear Models*, Springer, (1996), p. 239.
- [GUEN79] W. Günther, K. Huber, U. Kneissl, H. Krieger and H.J. Maier, *Phys. Rev. C* **19** (1979) 433.
- [GUN00] C. Gund, Dissertation, Universität Heidelberg (2000).
- [HAA87] B. ter Haar and R. Malfliet, *Phys. Rev. Lett.* **59**, (1987) 1652
- [HAB77] D. Habs, Habilitation, Universität Heidelberg (1977).
- [HAB99] A. Krasznahorkay, D. Habs, M. Hunyadi, D. Gaßmann, M. Csatlós, Y. Eisermann, T. Faestermann, G. Graw, J. Gulyás, R. Hertzenberger, H.J. Maier, Z. Máté, A. Metz, J. Ott, P. Thirolf, *Phys. Lett. B* **461** (1999) 15.
- [HAM75] I. Hamamoto and W. Ogle, *Nucl. Phys. A* **240** (1975) 13.
- [HAST39] O. Hahn and R. Strassmann, *Naturwissenschaften* **27** (1939) 11.
- [HAX49] O. Haxel, J. H. D. Jensen and H. E. Suess, *Phys. Rev.* **75** (1949) 1766.
- [HEN68] D. L. Hendrie, N. K. Glendenning, B. G. Harvey, O. N. Jarvis, H. H. Duhm, J. Saudinos and J. Mahoney, *Phys. Lett.* **26B** (1968) 127.
- [HOF01] F. Hofmann, C. M. Keil and H. Lenske, *Phys. Rev. C* **64** (2001) 034314.
- [HOL01] N. Holzapfel and P. Thirolf, *MLL Annual Report* (2001) 87.

- [HOO00] J. R. Hook and H. E. Hall, *Solid State Physics*, Second Edition, Wiley Chichester (2000).
- [HOR87] C. J. Horowitz and B. D. Serot, *Nucl. Phys.* **A464**, (1987) 613.
- [HOW80] W. M. Howard and P. Möller, *At. Data Nucl. Data Tab.* **25** (1980) 219 and references therein.
- [HUN99] M. Hunyadi, PhD Thesis, Lajos Kossuth University Debrecen, (1999) unpublished.
- [HUN01] M. Hunyadi, D. Gassmann, A. Krasznahorkay, D. Habs, P.G. Thirolf, M. Csatlós, Y. Eisermann, T. Faestermann, G. Graw, J. Gulyás, R. Hertenberger, H.J. Maier, Z. Máté, A. Metz and M.J. Chromik, *Phys. Lett. B* 505 (2001) 27 .
- [IKP] Institut für Kernphysik (IKP), Universität zu Köln, <http://www.ikp.uni-koeln.de/>.
- [KAL74] R. Kalish, B. Herskind, J. Pedersen, D. Shackleton and L. Strabo, *Phys. Rev. Lett.* **32** (1974) 1009.
- [KRA98] A. Krasznahorkay, M. Hunyadi, M. N. Harakeh, M. Csatlós, T. Faestermann, A. Gollwitzer, G. Graw, J. Gulyás, D. Habs, R. Hertenberger, H. J. Maier, Z. Máté, D. Rudolph, P. Thirolf, J. Timar, B. D. Valnion, *Phys. Rev. Lett.* **80** (1998) 2073.
- [KUC91] H. Kucharek and P. Ring, *Z. Phys.* **A339** (1991) 23.
- [LAN62] A. M. Lane, *Nucl. Phys.* **35**, 676 (1962).
- [LAN93] G. H. Lang, C. W. Johnson, S. E. Koonin and W. E. Ormand, *Phys. Rev. C* **48** (1993) 1518.
- [LAN95] K. Langanke, D. J. Dean, P. B. Radha, Y. Alhassid, and S. E. Koonin, *Phys. Rev. C* **52** (1995) 718.
- [LOJ98] Z. Lojewski and J. Dudek, *Acta Physica Polonica B* **29** (1998)
- [MAC89] R. Machleidt, *Adv. Nucl. Phys.* **19** (1989) 189.
- [MAN75] H. J. Mang, *Phys. Rep.* **18** (1975) 325.
- [MAR] MAR_aB_QU: <http://www.bl.physik.uni-muenchen.de/marabou/html/>.
- [MAY49] M. Goeppert Mayer, *Phys. Rev.* **75** (1949) 1969.
- [MEI38] L. Meitner and O. Frisch, *Nature* **143** (1938)
- [MET74] V. Metag, *Habilitationsschrift*, Universität Heidelberg, (1974).
- [MET80] V. Metag, D. Habs and H. J. Specht, *Spectroscopic Properties of Fission Isomers*, *Phys. Rep.* **65** (1980) 1.
- [MOEL73] P. Möller and J.R. Nix, 3rd IAEA Symp. *Phys. Chem. of Fission*, Rochester, USA, 1973, Vol. I, p.103.
- [MOR03] T. Morgan, C. Alvarez, B. Bruyneel, A. Bürger, D. Habs, H. Hübel, R. Lutter, H.J. Maier, E. Mergel, P. Reiter, O. Schaile, W. Schwerdtfeger, N. Warr and the MINIBALL Collaboration, *MLL Annual Report* (2003) 26.
- [MOS71] U. Mosel and H.W. Schmitt, *Nucl. Phys.* **A165** (1971) 13.
- [NAV96] P. Navrtil and B. R. Barrett, *Phys. Rev. C* **54**, (1996)

- [NAZ85] A.W. Nazarewicz, J. Dudek, Z. Szymanski, G. Leander, Nucl. Phys. A**435** (1985) 397.
- [NIL55] S. G. Nilsson, Dan. Mat. Fys. Medd. **29** (1955) No. 16.
- [NIL69] S. G. Nilsson, C. F. Tsang, A. Sobiczewski, Z. Szymanski, S. Wycech, G. Gustafson, I. Lamm, P. Möller and B. Nilsson, Nucl. Phys. A**131** (1969) 1.
- [NNDC] National Nuclear Data Center (NNDC), URL: <http://www.nndc.bnl.gov/nudat2/>
- [NOL88] P. J. Nolan and P. J. Twin, *Ann. Rev. Nucl. Part. Sci.* **38** (1988) 533 .
- [OBE07] A. Oberstedt, S. Oberstedt, M. Gawrys and N. Kornilov, Phys. Rev. Lett. **99**, 042502 (2007).
- [PAA07] N. Paar, D. Vretenar, E. Khan and G. Colo, Rept. Prog. Phys. **70** (2007) 691-794.
- [PAN98] D. Pansegrau, Dissertation, Universität Heidelberg (1998).
- [PAN00] D. Pansegrau, P. Reiter, D. Schwalm, H. Bauer, J. Eberth, D. Gaßmann, D. Habs, T. Härtlein, F. Köck and H.G. Thomas, Phys. Lett. B**484** (2000) 1.
- [PAU73] H.C. Pauli, Phys. Rep. **7C** (1973) 35.
- [PEL82] D. Pelte and D. Schwalm, *In-Beam Gamma-Ray Spectroscopy with Heavy Ions*, Heavy Ion Collisions Vol. 3, ed. by R. Bock, North-Holland Amsterdam, New York (1982).
- [PODR62] S. M. Polikanov, V. A. Druin, V. A. Karnaukhov, V. L. Mikheev, A. Pleve, N. K. Skobolev, V. G. Subbotin, G. M. Ter-Akop'yan and V. A. Fomichev, Soviet Physics JETP **15** (1962) 1016.
- [POV01] B. Povh, K. Rith, C. Scholz and F. Zetsche, *Teilchen und Kerne*, Springer Verlag, 5th edition, Heidelberg (2001).
- [RAF82] M. H. Rafailovich, E. Dafni, G. Schatz, S.Y. Zhu, K. Dybal, S. Vajda, C. Alonso-Arias and G.D. Sprouse, Phys. Rev. Lett. **48** (1982) 982.
- [RAF83] M. H. Rafailovich, E. Dafni, G. Schatz, S.Y. Zhu, K. Dybal, S. Vajda, C. Alonso-Arias, S. Rolston and G.D. Sprouse, Hyperf. Interact. **15/16** (1983) 43.
- [REI89] P. G. Reinhard, Rep. Prog. Phys. **52** (1989).
- [REI93] P. Reiter, Dissertation, Universität Heidelberg, (1993).
- [REI95] P. Reiter, D. Pansegrau, Ch. Ender, D. Habs, D. Schwalm, P. Thirolf, Proc. Conf. on Low Energy Nuclear Dynamics, eds. Yu. Oganessian et al., World Scientific (1995) 200.
- [RIN80] P. Ring and P. Schuck, *The Nuclear Many-body Problem*, Springer Verlag, Heidelberg (1980).
- [RIN96] P. Ring, Prog. Part. Nucl. Phys. **37** (1996) 193.
- [ROOT] ROOT - An Object Oriented Data Analysis Framework, URL <http://root.cern.ch/>.
- [RUS71] P. A. Russo, R. Vandenbosch, M. Mehta, J. R. Tesmer and K. L. Wolf, Phys. Rev. C**3** (1971) 1595.
- [SCH04] C. Schürmann, Facharbeit (2004), unpublished <http://www.ha.physik.uni-muenchen.de/forschung/gruppen/kernspektroskopie/publications/index.html/>.
- [SEG64] E. Segré, *Nuclei and Particles*, Benjamin, New York, 1964, 64

- [SER86] B. D. Serot, J. D. Walecka, *Adv. Nucl. Phys.* **16**, 1 (1986).
- [SER97] B. D. Serot, J. D. Walecka, *Int. J. Mod. Phys. E***6**, 515 (1997).
- [SER01] M. Serra, PhD Thesis, Technische Universität München (2001).
- [SPE72] H. J. Specht, J. Weber, E. Konecny and D. Heunemann, *Phys. Lett.* **B41** (1972) 43.
- [SPE74] H. J. Specht, E. Konecny, J. Weber and C. Kozhuharov, in: *Symposium on the Physics and Chemistry of Fission, 3rd*, Rochester, New York, 1973 (International Atomic Energy Agency, Vienna, Austria, 1974), SM-174/19.
- [STE75] R. M. Steffen, K. Alder, *Angular Distribution and Correlation of Gamma Rays*, in: *the Electromagnetic Interaction in Nuclear Spectroscopy*, ed. W. D. Hamilton, North-Holland Amsterdam (1975).
- [STR67] V. M. Strutinsky, *Nucl. Phys.* **A95** (1967) 420.
- [STR68] V. M. Strutinsky, *Nucl. Phys.* **A122** (1968) 1.
- [STR05] T. Striepling, Diploma Thesis, Institut für Kernphysik Universität zu Köln, 2005.
- [TE16SF] ASE GmbH, Schott Solar, URL <http://www.schott.com/photovoltaic/german/products/>.
- [THE97] Ch. Theisen, C. Gautherin, M. Houry, W. Korten, Y. Le Coz, R. Lucas, *The SAPHIR Detector*, DAPNIA/SPhN/97-20 (1997).
- [THI02] P. G. Thirolf and D. Habs, *Prog. Part. Nucl. Phys.* **49** (2002) 325.
- [THI03] P. G. Thirolf, *Habilitationsschrift*, Ludwig-Maximilians-Universität München (2003).
- [TYP99] S. Typel and H. H. Wolter, *Nucl. Phys.* **A656** (1999) 331.
- [TYP08] S. Typel, private communication 2008.
- [VAN731] R. Vandenbosch and J. Huizenga, *Nuclear Fission*, Academic Press, New York (1973).
- [VAN73] R. Vandenbosch, P.A. Russo, G. Sletten and M. Mehta, *Phys. Rev.* **C8** (1973) 1080.
- [VRE05] D. Vretenar, A. V. Afanasjev, G. A. Lalazissis, P. Ring, *Phys. Rep.* **409**, 101 (2005).
- [WAL74] J. Walecka, *Ann. Phys. (N.Y.)* **83** (1974) 491.
- [WAL95] J. D. Walecka, *Theoretical Nuclear and Subnuclear Physics*, Oxford University Press, Oxford (1995)
- [WAR01] D. Ward and P. Fallon, *Adv. Nucl. Phys.* **26** (2001) 167 .
- [WIL91] W. S. C. Williams, *Nuclear and Particle Physics*, Oxford University Press, Oxford (1991)
- [WEI03] D. Weisshaar, *Dissertation*, Universität Köln (2003).
- [WOL07] H. H. Wolter, *Prog. Part. Nucl. Phys.* **59** (2007)
- [WOL08] H. H. Wolter, private communication (2008).
- [XIA] X-Ray Instrumentation Associates (XIA), URL <http://www.xia.com/>.

Conference Presentations

Poster Presentations

-
- March 2003** **DPG Frühjahrstagung HK**
Tübingen, Germany
A SOLAR CELL BASED LARGE AREA FISSION DETECTOR ARRAY FOR SHAPE ISOMER STUDIES
- March 2004** **DPG Frühjahrstagung HK**
Köln, Germany
TOWARDS γ -SPECTROSCOPY OF THE ODD-N FISSION ISOMERS IN ^{237f}Pu USING MINIBALL
- March 2005** **DPG Frühjahrstagung HK**
Berlin, Germany
TOWARDS γ -SPECTROSCOPY OF THE ODD-N FISSION ISOMERS IN ^{237f}Pu
- Mai 2005** **Physics with MAFF**
Kloster Banz, Germany
TOWARDS γ -SPECTROSCOPY OF THE ODD-N FISSION ISOMERS IN ^{237f}Pu
- September 2005** **Euro School on Exotic Beams**
Mainz, Germany
TOWARDS γ -SPECTROSCOPY OF THE ODD-N FISSION ISOMERS IN ^{237f}Pu
- September 2006** **Work shop on the Atomic Properties of the Heaviest Elements**
Fraueninsel Chiemsee, Germany
 γ -SPECTROSCOPY OF SUPERDEFORMED ^{237f}Pu
- June 2007** **International Nuclear Physics Conference**
Tokyo, Japan
TOWARDS THE FIRST IDENTIFICATION OF NILSSON ORBITALS IN SUPERDEFORMED ACTINIDES
- December 2007** **The cluster of Excellence for Fundamental Physics, Science Week**
Munich, Germany
IDENTIFICATION OF SINGLE-PARTICLE STATES IN SUPERDEFORMED ^{237}Pu
- March 2008** **DPG Frühjahrstagung HK**
Darmstadt, Germany
IDENTIFICATION OF SINGLE-PARTICLE STATES IN SUPERDEFORMED ^{237}Pu

Oral Presentations

February 2004

MINIBALL Workshop

Leuven, Belgium

γ -SPECTROSCOPY IN THE SUPERDEFORMED MINIMUM OF ^{237}Pu

September 2005

Euro School on Exotic Beams

Mainz, Germany

TOWARDS γ -SPECTROSCOPY OF THE ODD-N FISSION ISOMERS IN ^{237}fPu

March 2006

DPG Frühjahrstagung HK

München, Germany

γ -SPECTROSCOPY OF SUPERDEFORMED ^{237}fPu

February 2007

ISOLDE Workshop

Geneva, Switzerland

γ -SPECTROSCOPY OF SUPERDEFORMED ^{237}Pu

March 2007

DPG Frühjahrstagung HK

Giessen, Germany

γ -SPECTROSCOPY OF SUPERDEFORMED ^{237}Pu

Mai 2008

The cluster of Excellence for Fundamental Physics, Research Area G day

Munich, Germany

NEW INSIGHTS INTO THE FISSION BARRIER LANDSCAPE OF ACTINIDE NUCLEI

Curriculum Vitae

Thomas James Morgan

born on **June 10th 1980** in **Munich**, Germany

Academic Education

November 2002 – Mai 2008	PHD student in Physics at the LMU Munich, Germany in the group of Prof. Habs subject HIGH RESOLUTION γ -SPECTROSCOPY OF ^{237}Pu
June 2002	Master of Physics at the University of Bath, UK grade UPPER SECOND 2.I
June 2001 - September 2002	Research Placement at the MPI für Physik Munich, Germany in the group of Prof. Schmitz subject DESIGN AND CONSTRUCTION OF THE STAR FTPC DRIFT VELOCITY MONITOR
September 1998	Begin of Studies in Physics at the University of Bath, UK
July 1998	European Baccalaureate at the European School Munich, Germany grade 7.3
1991–1998	Secondary School European School Munich, Germany Main Courses MATHEMATICS, PHYSICS, CHEMISTRY
1986–1991	Elementary School European School Munich, Germany

Practical Education

January 2005 – January 2007

Student Representative

Maier-Leibnitz-Laboratory, Munich Research Council

June 2000 – September 2001

Student Trainee

MPI for Physik Munich, Germany in the group of Prof. Schmitz
subject DESIGN AND CONSTRUCTION OF THE STAR FTPC DRIFT VELOCITY MONITOR

April 2000

Apprentice

Günther Braun Baufirma
Builders right hand

June 1999 – September 1999

Apprentice

Günther Braun Baufirma
Builders right hand

April 1999

Translator

Manitz Finsterwald und Partner
translating patent applications from German to English

August 1998 – September 1998

Apprentice

Günther Braun Baufirma
Builders right hand

June 1996

School Placement

at the Krankenhaus Neuperlach, Munich, Germany

Teaching Experience

- 2007** **Instructor**
Grundpraktikum in Experimentalphysik EPh
PRACTICAL PHYSICS TRAINING FOR PHARMACY STUDENTS
- 2006** **Instructor**
Grundpraktikum in Experimentalphysik EPh
PRACTICAL PHYSICS TRAINING FOR PHARMACY STUDENTS
- 2006** **Instructor**
Grundpraktikum in Experimentalphysik C
ADVANCED PRACTICAL PHYSICS TRAINING FOR PHYSICS STUDENTS
- 2005** **Instructor**
Grundpraktikum in Experimentalphysik EPh
PRACTICAL PHYSICS TRAINING FOR PHARMACY STUDENTS
- 2005** **Instructor**
Grundpraktikum in Experimentalphysik C
ADVANCED PRACTICAL PHYSICS TRAINING FOR PHYSICS STUDENTS
- 2006** **Course Assistant**
Physik P1
INTRODUCTORY COURSE ON PHYSICS FOR PHYSICS STUDENTS
- 2005** **Course Assistant**
Physik P1
INTRODUCTORY COURSE ON PHYSICS FOR PHYSICS STUDENTS
- 2004** **Instructor**
Grundpraktikum in Experimentalphysik EPh
PRACTICAL PHYSICS TRAINING FOR PHARMACY STUDENTS
- 2004** **Course Assistant**
Physik P5b
INTRODUCTORY COURSE ON PARTICLE PHYSICS FOR PHYSICS STUDENTS
- 2004** **Course Assistant**
Physik P5a
INTRODUCTORY COURSE ON NUCLEAR PHYSICS FOR PHYSICS STUDENTS
- 2003** **Course Assistant**
Physik P5a
INTRODUCTORY COURSE ON NUCLEAR PHYSICS FOR PHYSICS STUDENTS

Acknowledgements

The creation of this thesis would not have been possible without the help of my coworkers, colleagues and friends. First of all I would like to thank Prof. Dr. D. Habs for the opportunity of working in his nuclear structure group. His encouragement, desire and knowledge of physics led to the completion of this thesis.

Special thanks goes to Dr. Peter Thirolf without whose dedication and support this thesis would not be the same. The countless hours spent at any time of the day with Peter in the lab or in the office will be remembered. I have always been able to trust Peter's judgements.

The data obtained in the measurements of this thesis had to be interpreted, with the aid of the Ritz combinatorial program given to me by Prof. Till von Egidy I was able to produce my final level scheme. This level scheme was then the basis for the theoretical interpretation of my results which were discussed at length with Prof. Peter Ring and John Daoutidis, thank you. I would like to thank Prof. Dr. H. Wolter for proof reading my thesis, and his input to the theory chapters of this thesis.

During the course of this thesis I have shared my office with a few coworkers and partners in crime, I would like to thank Wolfgang, Lori, Kathrin, Carmen who all helped soften the atmosphere in the office. My personal assistant (slave) Christian will be remembered dearly.

The legendary pizza sessions with Jürgen before and "after" teaching will be greatly remembered. The countless coffees I drank with Stefan are probably responsible for my high blood pressure. The "Bussmännchen" has become a true friend be it the love for sailing (I have the slight feeling that you preferred swimming), schnaps, music or the daily walk to the drinks machine in which some or all of the daily frustration was washed away. Andrea was always a help when needed and a pain in the neck when not. Matthias are you coming to "soccer" this week?.

The one thing I will not miss is the canteen in Garching, the only thing that made it beareable was the daily discussions at lunch with Oli, Henning, Veli, Martin, Andreas, Mustapha, Sophie, Uli, Thomas, Raphael, Walter, Flo and Michael and anyone I may have forgotten.

It is always difficult deciding on whom to thank first, thus just starting off, I would like to thank Dr. Otto Schaile, Rudi Lutter and Klaus Steinberger for their support whenever a computing problem arose. I would like to thank Michael Schumann, Hartmut Steffens, Elisabeth Krönauer, Nicoletta Groff in the engineering office for all the mechanical drawings I bothered them with. Rolf Oehm and his crew in the mechanical workshop were an outstanding asset and a great aid by building all the little components required for the different experiments. Similarly I would like to say thank you to Dr. Sven Hegewisch and his team in the electronics lab. All

experiments performed in different set ups and places had one common denominator, the use of excellent targets produced by Dr. Jerzy Szerypo, Dr. Hans-Jörg Maier, Ulrich Friebel, Dagmar Frischke and Rainer Grossmann. Meike Dlaboha and Alexandra Hermann will always be remembered for the parties they organised. A special thanks goes to Rainhardt Satzkowski.

I would like to express my gratitude to the operations group of the tandem accelerator for providing a good working environment and "Teamegeist". Representing the crew at the MLL lab I would like to thank Walter Carli who has become a good friend both in the lab and on the ski slope. More often than not Mario joined us on these ski trips and had a steady supply of tissues. I would also like to express my gratitude to Dr. Ralf Hertenberger who always provided help when needed.

The beamtimes in Cologne could not have been performed without the help of local support. I would therefore like to thank Prof. P. Reiter for his continued support and commitment to this project. Tanja Kotthaus and Dr. Bart Bruyneel, were always of assistance and help, it was a true pleasure to work with them. I would also like to thank Dr. Andrey Blazhev, Norbert Braun, Dr. Alfred Dewald, Dr. Jürgen Eberth, Florian Finke, Dr. Christoph Fransen, Christoph Görden, Herbert Hess, Astrid Holler, Dr. Astrid Imig, Prof. Jan Jolie, Marijke Kalkühler, Daniel Martin, Dennis Mücher, Dr. Gheorghe Pascovici (and his team in the electronic workshop), Jean-Marc Régis, Michael Seidlitz, Lothar Steinert (and his team of tandem operators), Dr. Thorsten Steinhardt, Dr. Irina Stefanescu, Dr. Olaf Thelen, Stefan Thiel (representative of the mechanical workshop), Dr. Nigel Warr, Dr. Dirk Weisshaar and Andreas Wiens. Again should I have forgotten somebody I am sorry.

Last but not least, I would like to thank my friends and family for their love, support, comfort and friendship.